Durham E-Theses

Morphology, structure and electronic properties of CdTe surfaces studied by scanning tunneling microscopy

EGAN, CHRISTOPHER,KIERAN

How to cite:

EGAN, CHRISTOPHER,KIERAN (2011) *Morphology, structure and electronic properties of CdTe surfaces studied by scanning tunneling microscopy*, Durham theses, Durham University. Available at Durham E-Theses Online: http://etheses.dur.ac.uk/835/

Use policy

The full-text may be used and/or reproduced, and given to third parties in any format or medium, without prior permission or charge, for personal research or study, educational, or not-for-profit purposes provided that:

- a full bibliographic reference is made to the original source
- a link is made to the metadata record in Durham E-Theses
- the full-text is not changed in any way

The full-text must not be sold in any format or medium without the formal permission of the copyright holders.

Please consult the full Durham E-Theses policy for further details.

Academic Support Office, Durham University, University Office, Old Elvet, Durham DH1 3HP
e-mail: e-theses.admin@dur.ac.uk Tel: +44 0191 334 6107
http://etheses.dur.ac.uk

Morphology, Structure and Electronic Properties of CdTe Surfaces Studied by Scanning Tunneling Microscopy

by

Christopher K. Egan

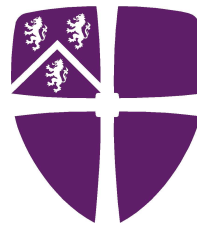

Submitted in conformity with the requirements
for the degree of Ph. D.
Department of Physics
Durham University

Copyright © 2011 by Christopher K. Egan

Contents

1 Introduction **1**

1.1 Outline . . . 1

1.2 Material Properties of CdTe . . . 6

1.3 Scanning Tunneling Microscopy . . . 7

1.4 Atomic Force Microscopy . . . 17

1.5 Atomic Structure of Clean Surfaces . . . 18

1.6 Summary . . . 23

2 Experimental Details **25**

2.1 The Scanning Tunneling Microscope . . . 25

2.2 Tip Preparation . . . 31

2.3 The Atomic Force Microscope . . . 33

2.4 Ion Sputtering System . . . 35

2.5 Crystal Growth . . . 37

2.6 Summary . . . 40

3 The (100) Surface **41**

3.1 Introduction . . . 41

3.2 Preparation of Well Defined Surfaces . . . 42

3.2.1 Introduction . . . 42

3.2.2 Sample Preparation . . . 46

3.2.3 Results and Discussion . . . 48

3.2.4 Summary . . . 53

3.3 Surface Reconstructions Imaged by STM 55
3.3.1 Sample Preparation 55
3.3.2 Results and Discussion 56
3.4 Conclusions 61

4 The (110) Surface 63

4.1 Introduction 63
4.2 Sample Preparation 65
4.3 Results 67
4.3.1 Surface Reconstructions 67
4.3.2 Tunneling Spectroscopy 70
4.3.3 Computation of Tunneling Spectra 76
4.4 Discussion 91
4.5 Conclusions 94

5 The (111) Surface 95

5.1 Introduction 95
5.2 Sample Preparation 96
5.3 Results 98
5.3.1 CdTe(111)A Surface 98
5.3.2 CdTe(111)B Surface 102
5.4 Discussion 112
5.5 Conclusions 116

6 Chemically Treated Surfaces 118

6.1 Introduction 118
6.2 Sample Preparation and Experimental Technique 119
6.3 Results 121
6.3.1 Surface Morphology 121
6.3.2 Tunneling Spectroscopy 124
6.4 Discussion 131

6.4.1 Etched surfaces 131
6.4.2 Passivated surfaces 134
6.5 Conclusions 135

7 Summary **137**

References **144**

Declaration

The material contained within this thesis has not previously been submitted for a degree at Durham University or any other university. The research reported within this thesis has been conducted by the author unless indicated otherwise.

Copyright Notice

The copyright of this thesis rests with the author. No quotation from it should be published without their prior written consent and information derived from it should be acknowledged.

List of Publications

1. *Morphology and reconstructions of polar CdTe(111)A,B surfaces by scanning tunneling microscopy*
   C. K. Egan, Q. Z. Jiang and A. W. Brinkman
   Journal Vacuum Science and Technology A **29** (2011) 011021

2. *Scanning tunneling microscopy and spectroscopy of the semi-insulating CdZnTe(110) surface*
   C. K. Egan, A. Choubey and A. W. Brinkman
   Surface Science **604** (2010) 1825

3. *Morphology and electronic states of chemically treated CdZnTe surfaces*
   C. K. Egan, A. Choubey and A. W. Brinkman
   Journal of Applied Physics **108** (2010) 024310

4. *A scanning probe microscopy study of* $Cd_{1-x}Zn_xTe$
   C. K. Egan, P. Dabrowski, Z. Klusek and A. W. Brinkman
   Journal of Electronic Materials **38** (2009) 1528

Abstract

Morphology, Structure and Electronic Properties of CdTe Surfaces Studied by Scanning Tunneling Microscopy

Christopher K. Egan

A scanning tunneling microscope has been used to study the surface properties of CdTe crystals. Coupled with scanning tunneling spectroscopy (STS) and atomic force microscopy, the surface morphology, structure and electronic properties of CdTe and CdZnTe surfaces have been studied. We have systematically investigated the three low index surface planes of the cubic crystal, that is the $\{100\}$, $\{110\}$ and $\{111\}$ surface planes. In addition, wet chemically treated surfaces were also examined. Clean surfaces were prepared in ultra-high vacuum conditions using argon ion sputtering and annealing. For each surface we imaged and recorded the surface reconstructions and morphologies. For the (100) surface, a mixed $c(2 \times 2) + (2 \times 1)$ surface phase was found, where steps on the surface were found to preferentially align along <100> directions. For the (110) surface, tunneling spectroscopy was used to investigate the surface electronic structure of the (1×1) reconstruction. Using theoretical calculations of the tunneling current, we were able to match theory to experiment and discern the various vacuum tunneling processes for both n-type and semi-insulating material. For the (111) surface, a (2×2) reconstruction consisting of a cadmium vacancy structure was found. For the $(\bar{1}\bar{1}\bar{1})$ surface, a very disordered c(8×4) reconstruction was observed, consisting of a complicated tellurium terminated chain structure. For both faces, a large amount of faceting was observed to occur with the facets formed by $\{311\}$ planes. Finally, wet chemically treated surfaces, important for the construction of many semiconductor devices, were investigated. Here the change in surface morphology for a variety of different common surface preparation methods was observed and, using STS, various surface electronic states were identified.

Acknowledgements

Firstly, I would like to thank my supervisor Prof. Andy Brinkman who has provided me with valuable guidance and encouragement. I would also like to thank him for giving me opportunity to work within this field, it's been extremely interesting and thoroughly enjoyable. I would also like to thank my co-supervisor Prof. Brian Tanner for stepping in at times of need and giving me some excellent advice.

I would like to extend my thanks to Prof. P. K. Datta from Northumbria University for kindly gifting us the STM used in this work. Thanks are also due to Prof. Z. Klusek and in particular Mr P. Dabrowski from the University of Lodz for teaching me the basics of STM and a little Polish! I would also like to thank my colleagues within the research group, Dr A. Choubey and Dr Q. Z. Jiang. Thank you for all the crystals that you've grown, I certainly couldn't have done this work without them! It's been a pleasure working with you both, and I wish you all the best for the future! Finally, I would like to thank Prof. R. M. Feenstra from Carnegie Mellon University, USA, for allowing me to use the SEMITIP program as well as for very useful discussions.

I also thank Mr R. D. Johnson for helping me with the Laue XRD and for some stimulating discussions. Thanks to Mr L. Bowen for performing the SEM work; Dr J. T. Mullins for various discussions and support; and Mr D. Pattinson, Mr D. McCallum and Mr N. Thompson for their technical assistance.

I wish to express my thanks to the HEXITEC project (EPSRC grant: EP/D048737/1) for financial support and the various members within HEXITEC for some interesting discussions and fun nights out!

Finally, I would like to thank my family for being so supportive over the past three years.

Dedicated to my family.

Chapter 1

Introduction

1.1 Outline

All solid materials have surfaces and interfaces. A solid interface defines the small region between two different solid materials, whereas a surface defines the region between the solid and the ambient conditions, i.e. the atmosphere or a vacuum. The properties of surfaces and interfaces can differ considerably from that of the bulk of the solid material [1]. As an example, a thin metal film that is deposited onto a semiconductor has a metal-semiconductor interface that separates the semiconductor from the metal. At the interface, diffusion of atomic species into either of the two materials can influence the properties of the interface region. Further, structural defects that existed at the surface of the semiconductor prior to metal deposition can trap electrical charge altering the charge transport characteristics of the metal-semiconductor system [2]. Surfaces are usually defined to include only the first few atomic layers. In practice however, the effects of a surface can have very far reaching effects. For example, a space charge region induced from electrical charge localised at the surface of a semiconductor, can reach depths of several microns.

Understanding the physical processes that occur at surfaces has become what is known today as *Surface Science* [3]. The study of surfaces is not necessarily limited to the study of solid-vacuum or solid-vapour interfaces.

As an example, consider the thin metal film once again. If we control the deposition of the metal film such that we are able to deposit one atomic layer at a time, then we can study the nucleation of the layers onto the surface as well as physical properties of the surface itself. In doing this, we learn information about the interactions of the film with the semiconductor substrate as well as what effect the growth conditions have upon the film. Now, if we deposit more and more layers, the semiconductor-metal interface turns from a surface into a buried interface and thus becomes difficult to probe. So by precisely controlling the deposition of the metal onto the semiconductor, we have gained information about the characteristics of the buried solid-solid interface. Controlling the deposition of the metal film and studying it on the atomic level inherently requires ultra-high vacuum (UHV), since it is the best environment where such surfaces can be prepared and maintained [1]. An exception to this is the electrochemical environment whereby surface studies are performed in liquids for the study of surface electrochemical reactions [4]. The main results of modern surface science therefore refer to the solid-vacuum, solid-vapour and solid-liquid interfaces.

The metal-semiconductor interface that we have been discussing above is very important in modern electronics. Every semiconductor device (light emitting diode, solid state laser, transistor, photovoltaic cell, etc...) has at least two metal-semiconductor interfaces, derived from metal contacts deposited onto the semiconducting surface so as to apply bias voltages to the device. The properties of these interfaces can have strong influences upon the properties of the device in question. Precise knowledge of the structure and chemical composition of the surface prior to metal deposition is key for controlling the properties of the metal contact [2]. Going further, surface science has played a very strong role in the development of the majority of modern semiconductor devices. The preparation of complex multilayer device structures (multilayer quantum wells, 2-dimensional electron gases, etc...) by molecular beam epitaxy (MBE) and metal organic vapour phase epitaxy (MOVPE) - are largely

derived from surface science techniques [5, 6]. In more recent times, the development of nanostructures (quantum dots, wires and wells) has been entirely reliant on surface science methods since they are inherently very small and typically manufactured on the surface of a substrate [7]. On a more fundamental level, surfaces have very interesting physical properties that can differ quite considerably from those of the bulk, and thus yields a wide variety of intriguing physics. The study of surfaces therefore furthers our knowledge of solid materials [3].

Over the past forty years, many experimental techniques have been developed to study the physical processes at surfaces. These can be roughly grouped into four categories: diffraction, electron spectroscopy, ion probing and microscopy [3]. Diffraction methods include electron and X-ray diffraction and yield the surface crystallography. These techniques are usually employed at grazing incidence so as to probe the 2D crystallography of the surface, such as in reflection high energy electron diffraction (RHEED) and grazing incidence X-ray diffraction (GIXRD) [8, 9]. However, by using very low energy electrons, the surface structure can be measured at higher incident angles, such as in low energy electron diffraction (LEED) [10]. Electron spectroscopy methods (including auger electron spectroscopy and photoelectron spectroscopy) can give the electronic structure and chemical composition of a surface. In this situation, the energy of the electrons emitted from the surface are analysed [1]. Ion probing techniques include ion scattering, eleastic recoil detection analysis and secondary ion mass spectroscopy. These methods use primary ion beams to either elastically scatter off the surface or sputter off target ions. These techniques typically give information on the elemental composition of a surface [1, 11, 3]. Microscopy techniques are used to produce real space magnified images of a surface. In general, microscopy provides information on the surface morphology (i.e the size and shape of the features that comprise the surface); the surface crystallography (i.e. the atomic structure and periodicity of the surface); and the surface composition (i.e. the elements and compounds

that the surface is composed of) [3]. Each surface analysis technique has its own specific advantages and disadvantages, and for a complete understanding of the physical processes that occur at surfaces, all of the above mentioned methods must be employed. Of the four categories of surface analysis methods, microscopy provides the highest resolution. All the other three groups are area averaged methods and thus generally provide an overview of the surface physics. Microscopy on the other hand, can give very high spatial resolution, even down to resolving individual atoms. Furthermore, the microscope can be coupled with other analysis methods, thus providing a very local probe of electronic or chemical properties. For example, modern scanning electron microscopes are often equipped with X-ray or electron spectrometers to analyse emitted auger electrons or X-rays. This can give information on the chemical composition of a surface with a spatial resolution below the micron level [12].

The operational principles vary greatly from one type of microscopy to another. They include: electron beam transmission (transmission electron microscopy)[13] and reflection (reflection electron microscopy, low energy electron microscopy, scanning electron microscopy)[14, 15, 12]; field emission of electrons or ions (field emission microscopy, field ion microscopy)[16]; or scanning the surface with a probing tip (scanning tunneling microscopy, atomic force microscopy)[17]. Of all of these, scanning tunneling microscopy (STM) and atomic force microscopy (AFM) provide the highest spatial resolution. STM can easily achieve atomic resolution, whilst AFM usually has nanometer resolution.[1]. These scanning probe techniques achieve such high resolutions because of local scale interactions of the probe tip with the surface. This very high spatial resolution gives these techniques the edge over other surface analysis methods. Further, these methods can be used as a very local probe using techniques like tunneling spectroscopy (current-voltage relationship) and force spectroscopy (force-distance relationship) giving these methods extra characterisation capabilities [17].

[1]Although the best AFM systems are able to achieve atomic resolution [18]

In this thesis we use scanning probe microscopy to investigate the surface physics of a particular semiconductor, namely cadmium telluride (CdTe). CdTe is a cubic II-VI semiconductor that finds many uses in the fields of photovoltaics and radiation detection. This material is ideally suited to photovoltaic solar cells because it has a band gap that is well tuned to the visible part of the electromagnetic spectrum [19]. It is also well suited as a high energy X-ray and gamma-ray detector because of its large average atomic mass, and high intrinsic resistivity [20]. Furthermore, the physical properties of CdTe can be tuned for different purposes when it is alloyed with other group II metals. For example, when alloyed with a small percentage of zinc (CdZnTe), the intrinsic resistivity of the material is increased allowing for a reduced leakage current and thus improved radiation detector performance [21]. When it is alloyed with mercury (HgCdTe), a useful infrared detector material is produced [22]. In the latter case, CdTe (as well as CdZnTe) is often used as a substrate for epitaxial growth of HgCdTe films. It is also often used as a buffer layer for epitaxial growth of HgCdTe on large area silicon substrates for the production of large area focal plane arrays [23]. Because CdTe has so many practical applications, understanding the surface physics of this material is essential for producing devices with good performance, especially as research and development in this material grows.

This thesis is focused on the use of scanning probe microscopy techniques to investigate the surface properties of CdTe and CdZnTe crystals. We have used a scanning tunneling microscope, along with tunneling spectroscopy and atomic force microscopy to image and characterise the surface morphology, atomic structure and electrical properties of CdTe and CdZnTe surfaces. We systematically investigate the three principle low index surfaces, the {100}, {110} and {111} miller surface planes of a cubic crystal, as well as examining chemically treated surfaces. In the next section we will outline the basic material properties of CdTe and CdZnTe, including the crystal structure and electrical properties which are relevant for STM studies.

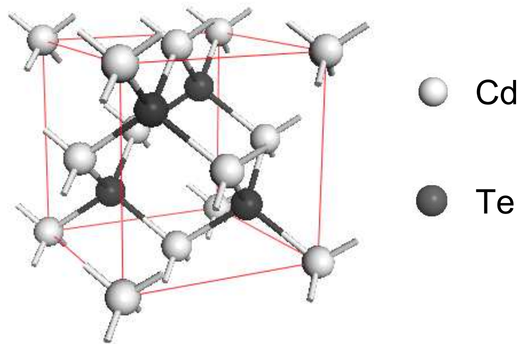

Figure 1.1: Ball and stick model of the zincblende crystal structure. The cubic unit cell is defined by the red boundaries.

1.2 Material Properties of CdTe

CdTe is a mechanically weak and brittle material (Knoop hardness = 45 kg/mm^2; critically resolved shear stress = 5 MPa, at room temperature) [24]. It has the zincblende crystal structure which consists of two interpenetrating face-centered cubic (fcc) sublattices displaced by 1/4 of a body diagonal. One fcc sublattice is entirely composed of group II elements, i.e. the cations (cadmium), and the other sublattice is entirely composed of group VI elements, i.e. the anions (tellurium). The structure is very similar to the diamond structure (found in group IV semiconductors, e.g. silicon) except that alternate atoms are comprised of group II and group VI elements, respectively, as shown in Figure 1.1. The lattice constant for CdTe is 6.481 Å at room temperature. Many other II-VI and III-V semiconductors have the same crystal structure, examples are zinc telluride (ZnTe) and gallium arsenide (GaAs). One particularly interesting property of the zincblende structure is that it lacks inversion symmetry, meaning there are no inversion centres within the crystal. This has important implications for some of the surface structures as will be described later in the thesis.

CdTe is a direct bandgap semiconductor with a band gap of 1.47 eV at room temperature. For intrinsic material (pure and undoped), CdTe has electron and hole mobilities of about 1000 cm^{2}V^{-1}s^{-1} and 100 cm^{2}V^{-1}s^{-1}, respectively

[25]. Undoped material is typically slightly p-type due to an abundance of cadmium vacancies, usually introduced during crystal growth because of the higher cadmium vapour pressure. N-type dopants are usually group III elements (e.g. indium) however n-type conductivity can also be achieved using group VII elements (e.g. chlorine) which displace group VI atoms yielding extra electrons to the lattice. P-type dopants are usually group V elements like phosphorous. For most practical applications however, undoped, high resistivity material is required. The intrinsic resistivity is usually found to be in the 10^9 Ωcm range. This can be increased to the mid 10^{10} Ωcm range by adding up to 10 % of zinc (ZnTe band gap $\sim$ 2.2 eV) to the lattice producing CdZnTe.

1.3 Scanning Tunneling Microscopy

The scanning tunneling microscope was first invented in the early 1980's by Gerd Binnig and Heinrich Rohrer who subsequently won the Nobel Prize for Physics in 1986 for its invention [26, 27, 28, 29]. It is a very powerful imaging system able to resolve individual atoms on the surface of solid materials. To do this, a bias voltage is applied between a very sharp metal tip and a conducting sample. These are then brought to within a separation of about 10 Å, and at these distances, electrons are able to quantum mechanically tunnel across the gap and a small electrical current can flow. If we consider a one-dimensional barrier, the transmission coefficient is dependent upon the barrier height, ϕ_B and barrier thickness d in the following way:

$$T \propto \exp\left[-2d\sqrt{\frac{2m}{\hbar^2}\left(\phi_B - E\right)}\right] \tag{1.1}$$

with m being the electron mass and E its energy [30]. Thus the transmission coefficient is exponentially dependent upon the barrier thickness, or for the STM, the tip-sample separation. This massive variation of the transmis-

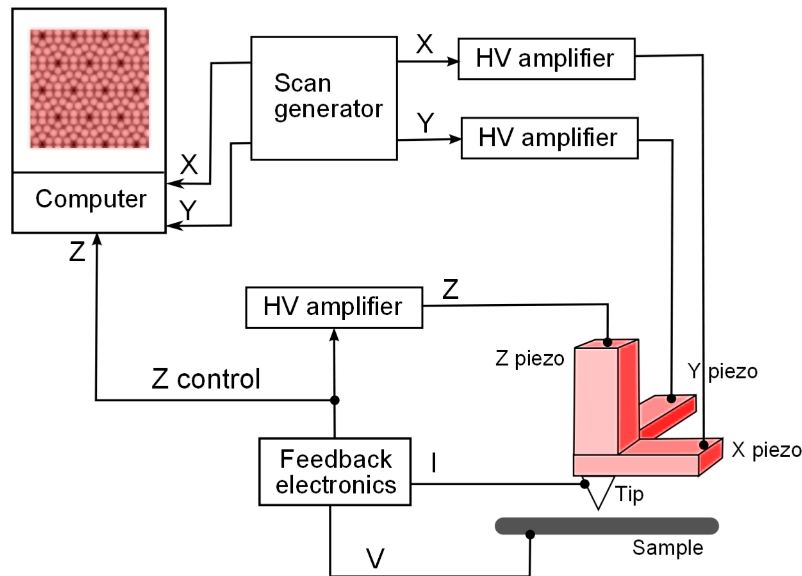

Figure 1.2: Schematic diagram of a typical STM set-up.

sion coefficient with tip-sample separation is what gives the STM its extreme spatial resolution. By scanning the tip across the surface and using the tunnel current to control the tip height, topographic maps of the surface can be obtained. Using very precise instrumentation, individual atoms can be imaged. A schematic diagram of a typical STM set-up is shown in Figure 1.2. The system is usually employed within an UHV chamber, such that the tunneling junction is metal-vacuum-metal or metal-vacuum-semiconductor. The use of a vacuum allows for a more stable tunneling current, as well as preventing contaminants from absorbing onto the surface and disturbing the surface physics to be studied.

In order to image surface features on the atomic scale, very precise positioning of the probe tip is required. Interactomic distances are typically of the order of a few angstroms and thus control of the tip position to better than 1 Å is required. This is achieved using piezoelectric materials to control the *xyz*-position of the tip. A change in length of a piezoelectric material is observed if a voltage is applied to it. By applying voltages in the range of several hundred Volts down to a few mV, scan ranges can vary between several hun-

dred nanometers and the angstrom range, with a resolution better than 1 Å. Most modern STMs use a tube scanner whereby the three piezoelectric drives (xyz shown in Figure 1.2) can be condensed into one 'tube' of piezoelectric material with three different electrodes to control the xyz position of the tip. For the z-axis, the height of the probe tip above the surface is controlled by the tunneling current. As was shown in Equation 1.1, the tunneling probability (and therefore the tunneling current) is exponentially dependent on the tip-sample separation; so if the tunnel current is kept constant to within 2%, then a vertical resolution of less than 0.01 Å can be achieved. This is the so-called *constant current* operation mode. The tunnel current is constantly recorded and fed back to the control electronics so as to maintain it at a constant specified value. As with all feedback systems, an amplification of the feedback signal coupled with a feedback factor is required. This controls how well the tip tracks the features on the surface. This so-called *loop gain* is a crucial control parameter for good surface imaging, although it can limit the scan speed somewhat. Alternatively, a STM can be operated in constant height mode, whereby the tip is scanned across the surface but the z position is kept constant and the current is recorded as a function of the tip position, producing a current image. The feedback system is switched off, which allows for much faster scan speeds; however, it can only be used on relatively flat surfaces and quantitative determination of the topographic height is difficult because a separate determination of the barrier height is required to calibrate z.

Up til now we have only mathematically considered a 1D tunnel barrier and assumed that the magnitude of the tunneling current is proportional to the tunneling probability. Although this description is physically correct, we really should have a more stringent mathematical description of the tunnel junction in order to fully understand the processes involved. This was provided in 1985 by Tersoff & Hamann [31] and we present the main details of this theory below:

Tersoff and Hamann modeled the STM using a sharp probe tip terminated

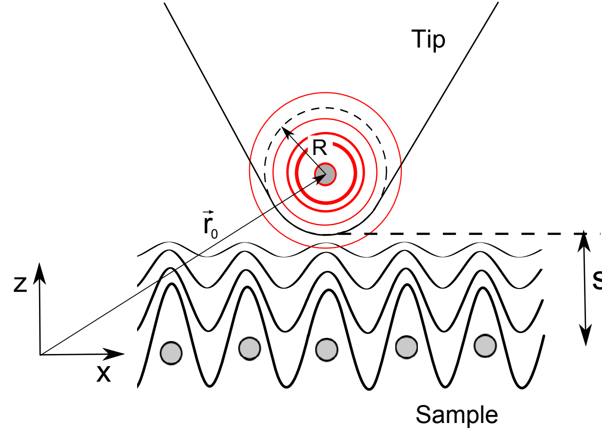

Figure 1.3: Schematic diagram of the tunnel junction within the Tersoff-Hamann theory of the scanning tunneling microscope. The tip (red) is approximated as an s-type wavefunction centered at $\vec{r_0}$. The tip itself has radius R and is separated from the surface by a distance s. The sample and tip wavefunctions (represented by grey and red waves) decay exponentially within the vacuum region.

with a single atom, as shown in Figure 1.3. Based on the Bardeen formalism [32], they wrote the tunnel current as:

$$I = \frac{2\pi e}{\hbar} \sum_{\mu,\nu} |M_{\mu\nu}|^2 \left[f(E_\mu) - f(E_\nu) \right] \delta(E_\mu - E_\nu - eV) \tag{1.2}$$

where $f(E)$ is the Fermi function, V is the applied bias voltage and $M_{\mu\nu}$ is the tunneling matrix element between states ψ_μ of the probe tip and ψ_ν of the sample. The Dirac delta function controls which direction the tunneling electrons flow. The matrix element was first proposed by Bardeen who was trying to understand the tunneling characteristics of two superconductors separated by thin oxide layers [32]. This is written as:

$$M_{\mu\nu} = \frac{\hbar^2}{2m} \int \left(\psi_\mu^* \nabla \psi_\nu - \psi_\nu \nabla \psi_\mu^* \right) d\vec{S} \tag{1.3}$$

where the integration is performed over any surface that lies completely within the tunnel barrier. For the the sample surface, plane wave extended

wavefunctions were used, which have the form:

$$\psi_\mu = \frac{1}{\sqrt{V_s}} \sum_{\vec{G}} a_{\vec{G}} e^{\left[-\left(\kappa^2 + |\vec{\kappa_G}|^2\right)^{1/2} z\right]} \exp\left(i\vec{\kappa_G} \cdot \vec{x}\right) \tag{1.4}$$

where V_s is the sample volume, $\kappa = \sqrt{\frac{2m\phi}{\hbar^2}}$ is the inverse decay length for the wavefunctions in the vacuum, ϕ is the work function, and $\vec{\kappa_G} = \vec{k}_{\|} + \vec{G}$ where $\vec{k}_{\|}$ is the surface Bloch wavevector and $\vec{G}$ is a surface reciprocal lattice vector.

For the tip, Tersoff and Hamann used wavefunctions with an asymptotic spherical form centered at the center of curvature of a tip with radius R and separated from the surface by a distance s. These wavefunctions have the form:

$$\psi_\nu = \frac{1}{\sqrt{V_t}} C_t \kappa R e^{\kappa R} \frac{\exp\left(-\kappa \left|\vec{r} - \vec{r_0}\right|\right)}{\left(\kappa \left|\vec{r} - \vec{r_0}\right|\right)} \tag{1.5}$$

where V_t is the volume of the tip, C_t is a normalisation constant, and $\vec{r_o}$ defines the center of radius. Evaluating the matrix element using these wavefunctions and substituting them into Equation 1.2, we get:

$$I = \frac{32\pi^3}{\hbar} e^2 V \phi^2 \rho_t(E_F) R^2 \kappa^{-4} e^{2\kappa R} \sum_\mu \left|\psi_\mu(\vec{r_0})\right|^2 \delta(E_\mu - E_F) \tag{1.6}$$

where $\rho_t(E_F)$ is the density of electronic states per unit volume of the probe tip at the Fermi level. This equation in itself is quite messy, however one crucial thing drops out; the tunneling current is proportional to the local density of states (LDOS) of the surface:

$$I \propto \sum_\mu \left|\psi_\mu(\vec{r_0})\right|^2 \delta(E_\mu - E_F) \equiv \rho_s(\vec{r_0}, E_F) \tag{1.7}$$

This implies that for an STM operating in constant current mode, the tip traces lines of constant LDOS.

The mathematical description presented above makes a number of approximations. For example, in considering the wavefunctions of the tip, s-type

wavefunctions were only considered. These are only adequate if the real wavefunctions of the metal atoms have a low angular momentum, l. Further, for a sufficiently large tip radius, the use of a single atomic wavefunction is likely to lose its validity. However, the incorporation of higher angular momentum wavefunctions or the use of multiple combined wavefunctions would make the mathematics much more complex and is unlikely to add to the physical understanding of the tunneling junction. In any case, the exact microscopic shape of the tip is unknown, so any theoretical approach will have to make some assumptions about the shape of the tip.

Since the wavefunctions decay exponentially within the vacuum region perpendicular to the surface:

$$\psi_\mu(\vec{r_0}) \propto \exp\left(-\kappa z\right) \tag{1.8}$$

we find that

$$\left|\psi_\mu(\vec{r_0})\right|^2 \propto \exp\left[-2\kappa(s+R)\right] \tag{1.9}$$

where s is the tip-sample separation. Therefore the tunnel current is found to be exponentially dependent upon the tip-sample separation, s, thus returning us to our first hypothesis based on Equation 1.1:

$$I \propto \exp\left(-2\kappa s\right) \tag{1.10}$$

This equation is quite useful; the variation of the tunnel current with tip-sample separation gives us a measurement of the inverse decay length, κ, of the wavefunctions at the surface, and in turn yields the local barrier height.

Now let us look in more detail about what effect the applied voltage has on the tunnel characteristics. The applied voltage is of course necessary for a current to flow, and the polarity of the voltage controls which direction the current flows (mathematically represented by the Dirac delta function in Equation 1.2). Firstly, consider a positive sample bias, i.e. electrons flowing

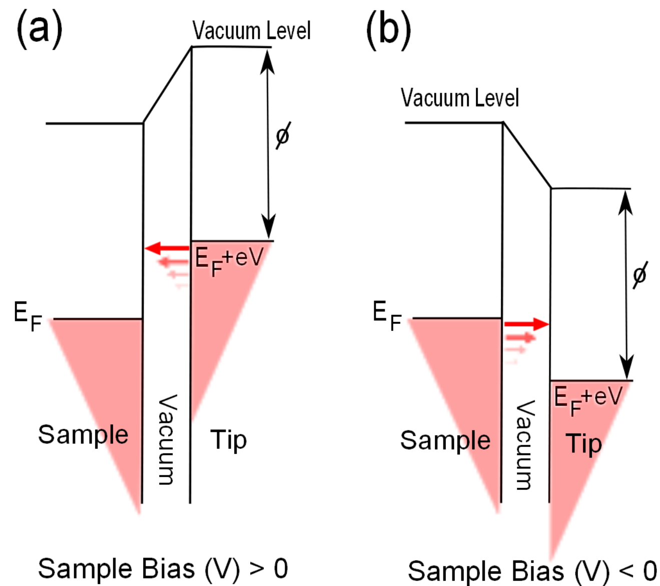

Figure 1.4: Energy diagram for a metal-vacuum-metal tunnel junction. (a) Positive sample bias: electrons tunnel from the filled states of the tip to the empty states of the sample. (b) Negative sample bias: electrons tunnel from the filled states of the sample to empty states of the tip.

from the tip into the sample. This is schematically represented in Figure 1.4. In this situation the tip is probing *empty states* of the sample. For a negative sample bias, electrons tunnel from the sample to the tip, and thus the *filled states* of the sample are probed. Therefore, the tunnel current should show strong differences at positive and negative bias, depending on whether empty or filled states of the sample are probed. This effect is particularly evident on semiconductors which have strongly different bandstructures either side of the bandgap. This so called bias dependent imaging can be taken further by taking current-voltage curves. This then probes the specific changes in the bandstructures for both empty and filled states and gives us a measure of the LDOS of the surface as a function of bias voltage (energy). This mode of operation is called *scanning tunneling spectroscopy* (STS) and is a very useful local probe which can be scanned across the surface to measure the surface LDOS at specific locations [17].

Up til now we have limited our discussion to a metal-vacuum-metal tunnel-

ing junction. Consider now a metal-vacuum-semiconductor tunneling junction which is more applicable for STM studies on CdTe surfaces. The basic principles are the same as for the metal-vacuum-metal junction, however typically, higher bias voltages are required for STM measurements on semiconductors. This is a consequence of the bandstructure of the semiconductor and in particular the fundamental bandgap near the Fermi level. At negative sample bias (probing filled states), we are usually dealing with electrons tunneling from the *valence band* of the semiconductor into the metal tip. For positive sample bias (probing empty states) we are usually dealing with electrons tunneling from the metal tip into the *conduction band* of the semiconductor. However we must also consider the electric potential of the metal tip. The small distance between the tip and sample allows for very high electric fields to be produced. This field is screened by the charge carriers in the metal and semiconductor, respectively. For metals, the screening length is very small (< 1 Å) because of the high number of charge carriers. However for a semiconductor, the number of charge carriers in the bulk is typically 6 - 8 orders of magnitude smaller, and so the electric field of the tip penetrates deep into the semiconductor bulk. Typical screening lengths vary between tens of nanometers for highly doped semiconductors up to several microns for weakly doped, or undoped material. The resultant situation resembles that of a metal-semiconductor Schottky contact, except that some of the applied bias is dropped across the vacuum gap. Just like Schottky contacts, there exists a space charge region underneath the metal tip, causing the bulk bands of the semiconductor to be bent. This effect is known as *tip induced band bending* (TIBB) and is defined as the electrostatic potential at a point directly underneath the tip [33]. Typical band bending profiles that commonly occur for a metal tip in close proximity to an n-type semiconductor are shown in Figure 1.5. Figure 1.5(a) shows the case for a positive sample bias. The electronic bands are bent upwards and the near-surface region is depleted of charge carriers. This is known as *depletion.* Figure 1.5(b) shows the case for negative sample bias. The bands are bent downwards and

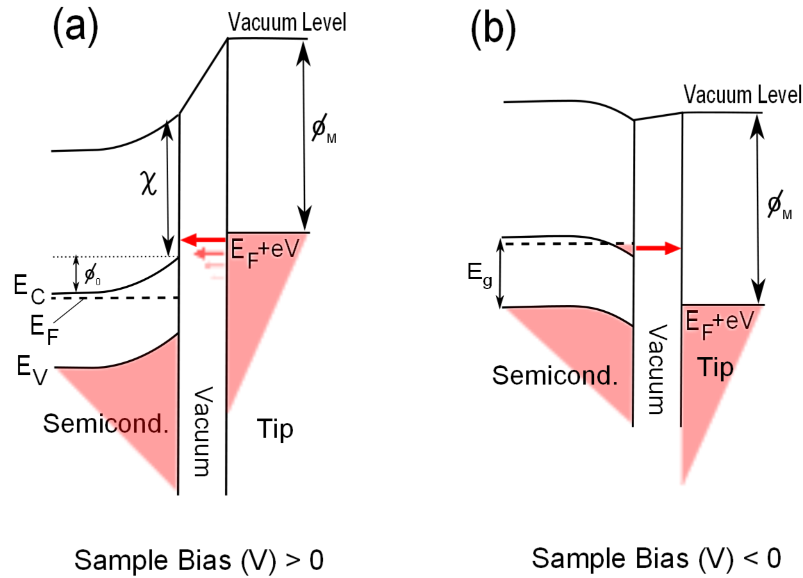

Figure 1.5: Energy diagram for a metal - vacuum - n-type semiconductor tunnel junction. (a) Positive sample bias. The bands are bent upwards, depleting the near-surface region of charge. The TIBB is defined as ϕ_0. (b) Negative sample bias. The bands are bent downwards, and electrons accumulate at the near-surface region. These localised electrons provide the tunnel current.

the Fermi level closely approaches the conduction band resulting in a large number of electrons accumulating at the near-surface region. This is known as *accumulation*. For extremely large negative bias voltages, a so-called inversion layer could form where the Fermi level approaches the valence band, allowing holes to exist at the near-surface region. This situation (not shown in Figure 1.5) is known as *inversion* because the conductivity type of the near surface-region is effectively reversed. Similar scenarios could be envisaged for p-type semiconductors, but with the definitions reversed in-line with the majority carrier reversal (e.g. an accumulation layer is defined as holes accumulating at the surface for p-type material).

TIBB can have a strong effect upon a measured tunneling spectrum (current-voltage relationship $[I(V)]$) and must be taken into account when one is interested in the surface LDOS. The effect of TIBB is to shift any observable surface features of energy E in the tunneling spectrum (such as band onsets or surface states) by the amount of TIBB, which is defined as the potential

energy at the semiconductor surface, ϕ_0:

$$E - E_F = eV - \phi_0 \tag{1.11}$$

In order to account for this one must calculate the variation of the TIBB with bias voltage [$\phi_0(V)$]. This is performed by solving Poisson's equation (in the same way as for metal-semiconductor contacts), but taking into account the voltage drop across the vacuum gap. To do this one must know the electrostatic potential of the tip relative to a point deep inside the semiconductor. This is defined as:

$$\phi_T = eV + \Delta\phi \tag{1.12}$$

where the contact potential, $\Delta\phi$, is the difference in work function between tip and sample:

$$\Delta\phi = \phi_m - \chi - (E_C - E_F) \tag{1.13}$$

where ϕ_m is the metal work function, χ is the semiconductor electron affinity, E_C is the conduction band minimum and E_F is the sample Fermi level within the bulk [34]. Furthermore, one must also consider the 3D shape of the probe tip, since a sharp tip will drop more of the applied bias across the vacuum gap; as compared to a blunt tip with a large radius of curvature which will drop more of the electric field within the semiconductor bulk [35]. Such calculations are usually performed numerically using finite element methods to model the 3D tip shape. Later in this thesis we will calculate the TIBB [$\phi_0(V)$] and use it to calculate tunneling spectra using the equations presented above. These will be used to compare to tunneling spectra obtained from STM experiments on CdTe surfaces. Further details about the calculation formalism, including how the 3D shape of the tip is accounted for, will be given then.

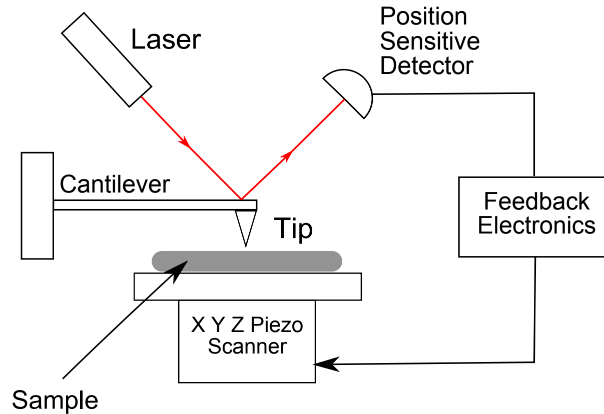

Figure 1.6: Schematic diagram of a typical AFM set-up

1.4 Atomic Force Microscopy

Throughout this thesis, an atomic force microscope (AFM) has been used to supplement STM studies. The basic principles of AFM are very similar to that of STM in that a sharp probe is precisely scanned across a surface whilst the probe height is recorded and used to image the surface. Typically the probe tip is mounted on the end of cantilever which is deflected through interatomic force interactions with the surface. The tip-sample forces originate from a variety of sources including: Van der Waal's interactions, electrostatic forces and capillary effects. The cantilever deflection is measured by a deflection sensor which come in a variety of different forms. The first AFM's used an STM with its tip positioned onto the back of a conducting cantilever to measure the deflection [36]. The majority of modern AFM's use a laser beam that is reflected off the back of the cantilever onto a position sensitive detector [Figure 1.6]. AFM can be operated in three different modes: contact mode, non-contact mode, or tapping mode. In contact mode the tip is in soft physical contact with the surface and is subjected to repulsive forces [Figure 1.7]. The tip-sample distance is only a couple of angstroms and to avoid surface damage the cantilever must be very soft. This operation mode is thus very prone to damaging the surface, especially for soft materials. In non-contact mode, the tip-sample separation is quite large (100 Å - 1000 Å) and the probe is

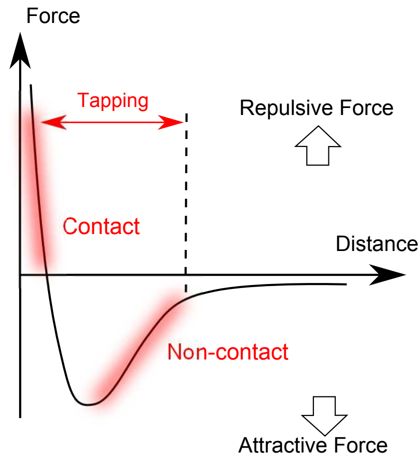

Figure 1.7: Qualitative representation of the Van der Waal's forces acting between two closely spaced atoms. The regions of each AFM operation mode are indicated.

subjected to weak attractive forces [Figure 1.7]. The cantilever is oscillated at its resonant frequency and scanned across the surface. Forces acting on the tip cause a change in frequency of the oscillating cantilever. If the frequency of the oscillating tip is kept constant, then this can be used as a feedback signal and thus image the surface. This mode of operation is in fact sensitive to the force-gradient rather than the force itself and thus traces lines of constant gradient. The advantage of this method is that the probe does not touch the surface and so no damage is incurred; unfortunately scan rates are much reduced. In tapping mode, the cantilever is oscillated at a larger amplitude such the it almost touches the surface at the bottom of its swing. Therefore the the AFM is now alternated between contact and non-contact modes. This offers some advantages over non-contact mode AFM for surfaces that may have liquids absorbed onto the surface [17]. The experimental details of the AFM used in this work will be provided in Chapter 2.

1.5 Atomic Structure of Clean Surfaces

In this section we overview the basic principles of surface science and surface crystallography. The theory presented here largely follows that of Luth[1]

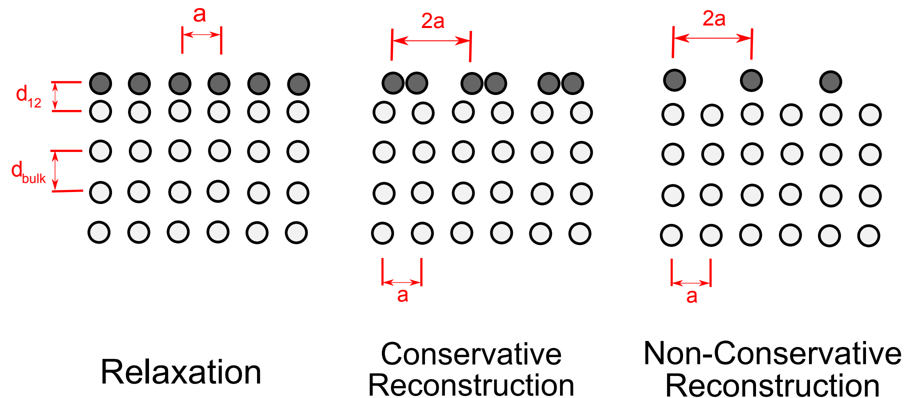

Figure 1.8: Schematic illustration of relaxed and reconstructed surfaces. (left) Relaxation of the topmost layer normal to the surface. The surface 2D periodicity is maintained. (centre) Conservative reconstruction of the topmost layer into a surface net with a period twice that of the bulk. The number density of surface atoms is preserved. (right) Non-conservative reconstruction where the number density of surface atoms is not preserved.

and Oura *et al.*[3] and for further details the reader is advised to consult those sources. On a surface, due to the absence of neighbouring atoms on one side, the interatomic forces in the uppermost atomic layers are considerably changed. Because of this the atomic positions of the surface atoms are expected to be altered, resulting in a different surface crystallography. Thus the surface is *not* simply a truncation of the bulk crystal. The nature of the surface alteration is obviously material dependent. For example, in a metal, the interatomic bonding is governed by a strongly delocalised electron gas; whereas in a semiconductor, the bonding is highly directional. Therefore any bond breaking on a semiconductor is expected to have a strong effect on the resultant surface atomic arrangement.

There are two general types of atomic rearrangements at a surface. These are *relaxation* and *reconstruction* and are schematically shown in Figure 1.8. For a relaxed surface, the topmost layer has the same atomic arrangement as in the bulk, but the interlayer spacing is modified. For a reconstructed surface, the surface atomic arrangement is different from that in the bulk. This rearrangement can either be done conservatively, whereby the number of atoms on the surface is the same as for the bulk-truncated surface; or non-conservatively,

whereby the number of atoms on the surface is different from that of the bulk-truncated surface. Typically, reconstructed surfaces are also accompanied with some kind of relaxation due to the re-distribution of charge associated with forming new bonds. Relaxation and reconstruction is not necessarily confined to the topmost layer. For some materials a surface reconstruction may consist of a complicated two or three layer construction, however the basic principles still apply. While reconstructions are limited to only a handful of metal surfaces, they are very common on semiconductor surfaces. The high directionality of the bonds in semiconductors means that the bulk truncated surface has a high density of dangling (or partially filled) bonds. In order to minimize the surface free energy, the surface atoms rearrange themselves in order to fill these partially filled dangling bonds. This happens either by forming new bonds with one another (common in the group IV elemental semiconductors); or by charge transfer between dangling bonds making some completely filled but leaving others completely empty (common in compound semiconductors). On the other hand, the atomic displacements induce a lattice strain within the topmost layers which increases the surface free energy. The interplay between these two effects governs the particular reconstructions of a surface.

Having outlined the basic physical concepts behind surface restructuring we now need a way to mathematically define the surface crystallography. Although a surface (or interface) is inherently a three-dimensional (3D) entity having a certain thickness, the symmetry of the surface is only two-dimensional (2D), i.e. it is periodic in two directions only. For a 2D surface there are only five differing Bravais lattices (as opposed to 14 in 3D), these are: oblique, rectangular, centered rectangular, square and hexagonal; and are shown in Figure 1.9. In order to relate the surface reconstruction to the crystallography of the bulk, we use the Wood notation:

$$X(hkl) - \left(\frac{a}{|a|} \times \frac{b}{|b|}\right) R\theta$$

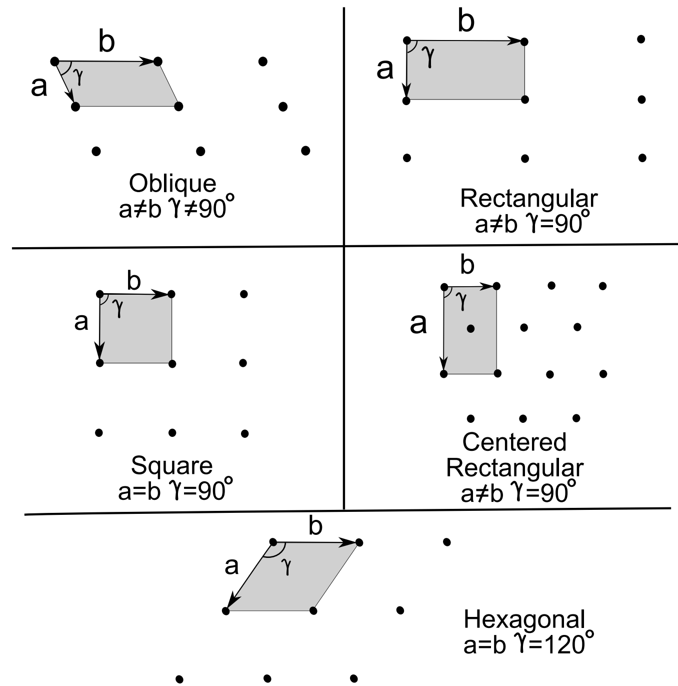

Figure 1.9: Five 2D Bravais lattices. Translation vectors are shown with unit cells shown as shaded regions.

Where X is the chemical formula for the material in question (e.g. Si or GaAs); (hkl) represents the substrate surface plane; a and b are the surface vectors for a particular Bravais lattice; and R represents a rotation of the superstructure by θ degrees with respect to the substrate axes (i.e. the principle axes for a particular 2D Bravais lattice). Some examples of a superstructure (reconstruction) on different bravais lattices, along with their associated Wood notations, are shown in Figure 1.10. Note that so far the discussion has been solely about *lattices* rather than structures. Remember that a crystal structure is made from the addition of a *basis* to every lattice point.

The basis for a 2D lattice will of course be material and surface dependent. For example, the GaAs(100)2×4 surface has a variety of different structures which all have the same periodicity. This surface forms arsenic dimers which are arranged in three different structures (the α, β and $\beta 2$ phases) all of which have the same 2×4 periodicity [37, 38]. These structures (the basis) are all slightly differently arranged: the α phase consists of two arsenic surface

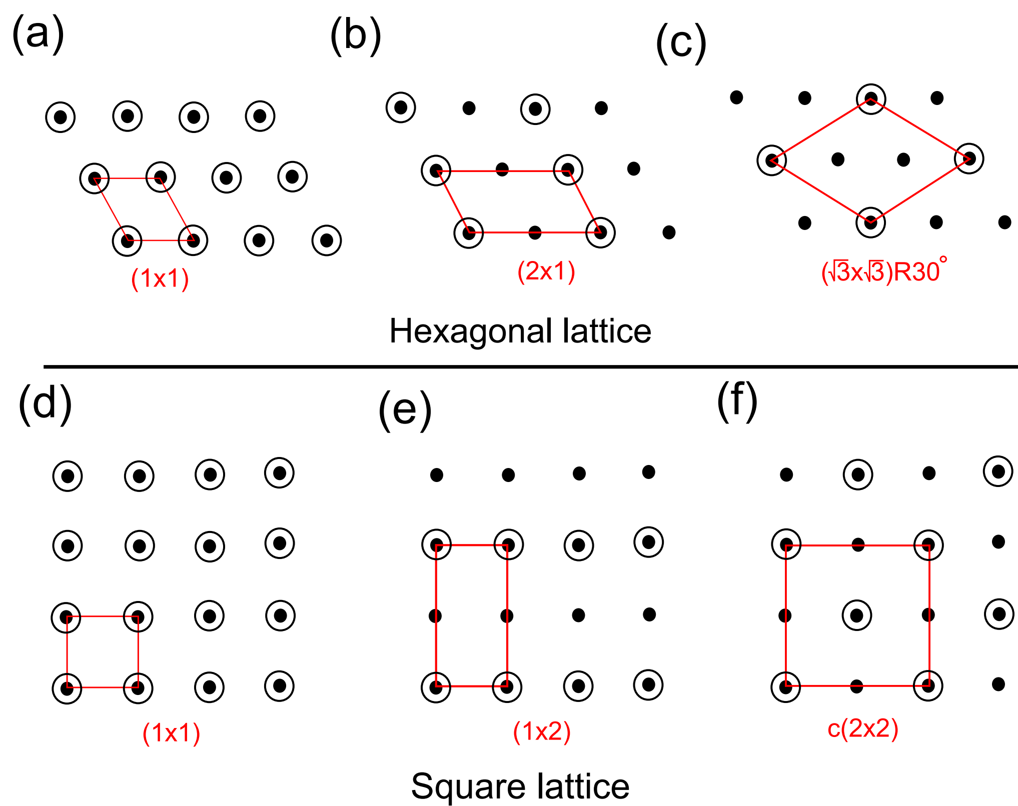

Figure 1.10: Wood notation for various superstructures (open circles) on a 2D lattice. (a)-(c) superstructures on hexagonal lattice. (d)-(e) Superstructures on square lattice.

dimers, the β phase consists of three arsenic surface dimers and the $\beta 2$ phase consists of two arsenic surface dimers and one arsenic dimer in the third layer. All three structures show significant relaxation in the surface bonding. This example demonstrates how different surface structures can exhibit the same superlattice [(2×4)] but completely different atomic structures (basis).

1.6 Summary

In summary, this thesis is focused on the use of a scanning tunneling microscope to investigate the properties of CdTe surfaces. We have used this, along with tunneling spectroscopy and atomic force microscope to image and characterise the surface morphology, atomic structure and electrical properties of CdTe surfaces. In this chapter we have outlined some of the main physical properties of CdTe and it's various practical applications. We have described the operational principles and theory of the scanning tunneling microscope (STM) and discussed how it can be used to investigate the surface morphology, structure and electronic properties of the surfaces of solid materials. We have also described the physical principles of the atomic force microscope and discussed how this technique can be used to complement STM studies. We have outlined the theoretical aspects of surface atomic structures and described the principles of relaxation, reconstruction and surface crystallography. We will use this knowledge and apply it to studying the surfaces of CdTe.

This thesis is organised as follows: In the next chapter (Chapter 2) we describe the experimental techniques used in this work. We outline both the STM and AFM used, as well as the methods of probe tip preparation. We also outline the equipment and methods used to prepare clean surfaces in vacuum. Finally we describe the crystal growth methods used to grow the single crystals of CdTe and CdZnTe to be studied. In the following three chapters we systematically investigate the atomic structure and electronic properties of the three lowest index surface planes. These are the {100}, {110} and {111}

miller planes of a cubic crystal. For the (100) surface (Chapter 3) we start by investigating what is required to obtain a clean surface in vacuum. This is performed by bombarding the surface with argon ions. The effect on the surface morphology for different ion energies and fluxes is investigated. We then follow on and study the surface reconstructions formed after annealing sputtered surfaces in vacuum. For the (110) surface (Chapter 4) we introduce the concepts of tunneling spectroscopy and apply these to investigate the electronic structure of this surface. To do this, we calculate the tunneling spectra obtained from CdTe and CdZnTe surfaces and use these to match to experiment. This is then correlated with the observed surface reconstructions. For the (111) surface (Chapter 5), we investigate the surface reconstructions and surface morphology for clean surfaces prepared in UHV. We then move on to discuss certain surface defects that can be seen in STM images. In the penultimate chapter (Chapter 6), we use our knowledge and experience from studying clean surfaces and build upon it by investigating the surface morphology and electronic properties of chemically treated CdTe and CdZnTe surfaces. This includes investigations using AFM and tunneling spectroscopy. In the final chapter (Chapter 7) we summarise the thesis and draw conclusions.

Chapter 2

Experimental Details

2.1 The Scanning Tunneling Microscope

The scanning tunneling microscope used throughout this work is an Omicron micro H STM. It operates in constant current mode and uses a single tube scanner with a maximum scan range of 15 $\mu m \times 15$ μm with a z-travel of about 2 μm. The STM has a two stage current-voltage converter and amplification. The first is in vacuum and sits very close to the instrument to reduce electronic noise. The second lies outside vacuum which also serves as a power supply for the in-vacuum electronics. In this set up, the tip is always kept at ground potential, whilst the bias voltage is applied to the sample. The STM stage is well designed for easy sample and tip transfer. Coarse sample and tip positioning is achieved using piezoelectric stacks with a slip/stick motion, driven by a sawtooth voltage input. For fine tip positioning (i.e. to bring the tip into tunneling contact) a combination of coarse approach and tube scanner z-movement in a cyclic process is employed which terminates when a tunnel current is measured. The STM stage has in-situ sample heating facilities using an indirect resistive heating method on the backside of the sample plate. The system has a temperature range between room temperature and 350°C which is measured by a NiCr/Ni thermocouple mounted to the topside of the sample stage. The temperature difference between sample and thermocouple is less

than 10 °C. Vibration isolation is achieved by a soft viton rubber stack on which the whole STM stage is mounted. A simplified schematic diagram of the STM stage is shown in Figure 2.1.

The whole system is housed within a bakeable ultrahigh vacuum (UHV) chamber with a base pressure of $< 6 \times 10^{-11}$ mbar. Such low pressures are achieved immediately after bakeout, however the typical working pressure of the system is the range $(1-2) \times 10^{-10}$ mbar. This is because of the introduction of contaminants after sample/tip loading and surface sputtering etc... The UHV chamber is pumped by a 150 l/s ion pump backed with a titanium sublimation pump. The chamber pressure is measured by a hot filament ionisation gauge. Samples are loaded into vacuum by a load-lock which is pumped by a turbomolecular pump. This also acts as a backing pump for the whole system. Sample transfer in vacuum is achieved using a pincer-grip wobble stick. The chamber is also equipped with a cold-cathode ion sputtering source and rotational manipulator with sample heating facilities. The details of these two systems will be discussed in Section 2.4. The whole chamber sits on pneumatic damping legs to reduce mechanical vibrations.

Calibration of the tube scanner was performed by imaging the (0001) basal plane surface of highly ordered pyrolytic graphite (HOPG). HOPG lends itself to be very useful as a STM calibration material because of its well known structure and stable surface. Clean surfaces can be prepared in air by cleavage using sticky tape to remove the top surface layers. The resultant surface can be imaged at atomic resolution in air as well as in vacuum. Figure 2.2 shows STM images of the HOPG surface made using a platinum/iridium tip in UHV. Figure 2.2(a) shows the raw data image with no filtering applied to it. The surface has a six-fold symmetry with each protrusion surrounded by six nearest neighbours. Figure 2.2(b) shows the fast Fourier transform (FFT) image of (a). By measuring the positions of the spots in this image we get the reciprocal of the atomic spacing. This also acts as the calibration for the tube scanner. The calibrated scanner measures the atomic spacing to be 2.46 Å. Figure 2.2(c)

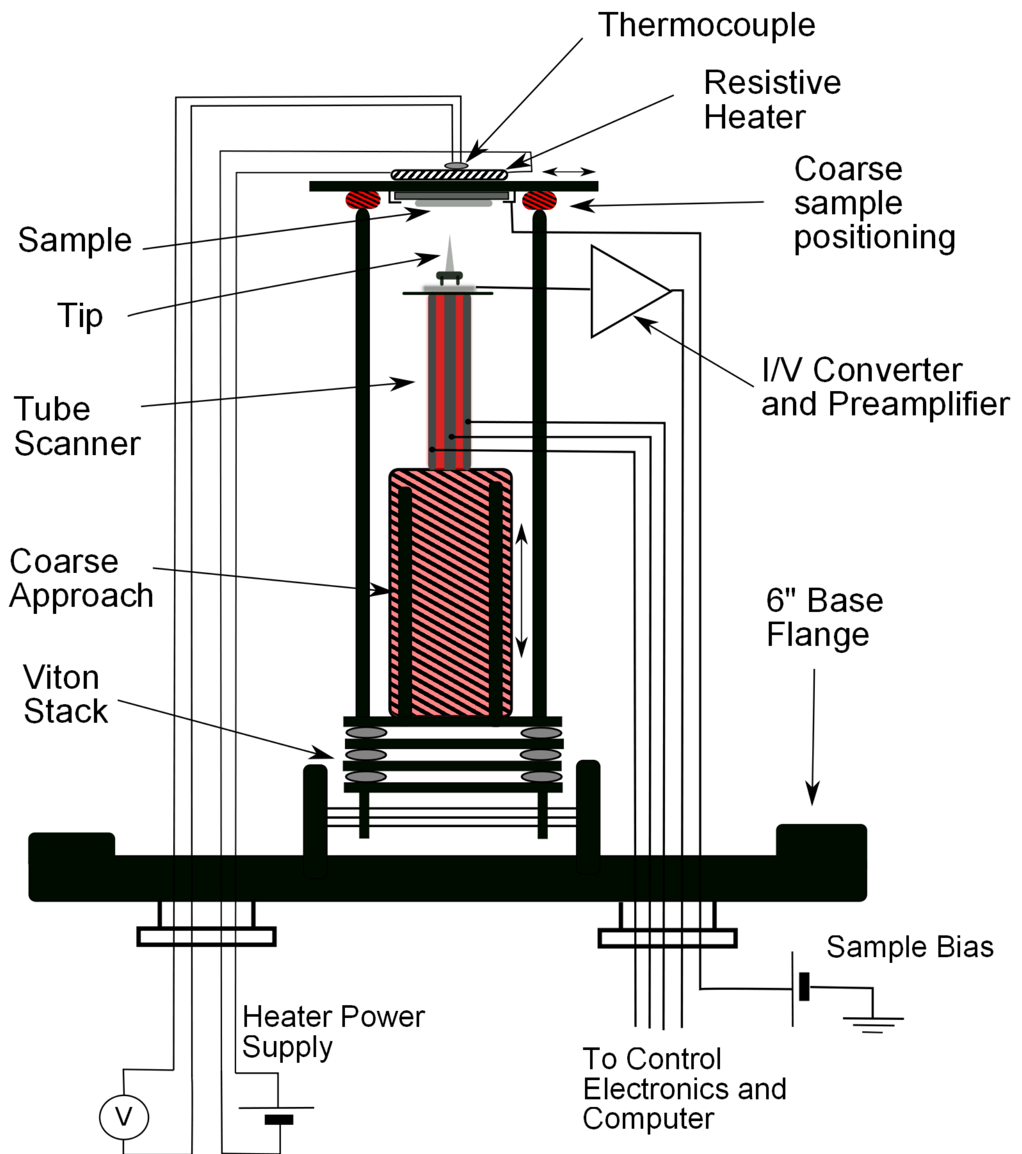

Figure 2.1: Simplified schematic diagram of the Micro H STM.

shows a FFT filtered (and expanded) image of (a). The atomic positions are now very clear but the surface does not show the hexagonal structure as one would expect for graphite. Indeed, a hexagonal structure has been superimposed on the image in Figure 2.2(c) and we can see that every other carbon atom is imaged. This phenomenon is due to the stacking arrangement of the graphite layers resulting in the so-called A-sites and B-sites. A-site atoms lie directly above atoms from the layer below, whereas B-site atoms lie directly above a void. The result is increased charge density residing on A-sites rather than B-sites, and thus making them more prone to imaging [39]. This highlights the sensitivity of the STM to surface *charge density* rather than the atoms themselves.

Calibration of the z-axis is performed by imaging steps on the HOPG(0001) surface. The cleavage process is usually not perfect, and large scale terraces can form. The distance between adjacent graphite planes is 3.35 Å and steps are usually $n \times 3.35$ Å high, i.e. multi-height steps can form. Figure 2.3(a) shows a large area STM image of the cleaved HOPG(0001) surface. Here we see a number of terraces separated by steps. The terraces typically extend over a very large area of approximately greater than 800 nm. A line profile taken across the surface (Figure 2.3(b)) shows the step height to be 3.35 Å, and this is used to calibrate the scanner.

Tunneling spectroscopy measurements were performed using an interrupted feedback loop system. This involves switching off the feedback loop and scanning the bias voltage through a preset range of values. A number of delay times (typically in the microsecond range) are used to allow stabilisation of the current and prevent capacitance effects. Typically, STS measurements were obtained between bias voltages of -3 V and +3 V in steps of 0.006 V. A better method to obtain high quality STS spectra would be to use an oscillating voltage signal superimposed on top of the preset bias voltage. The tunneling current is then recorded using a lock-in amplifier yielding the derivative of current with respect to voltage (dI/dV) at various bias voltages. The

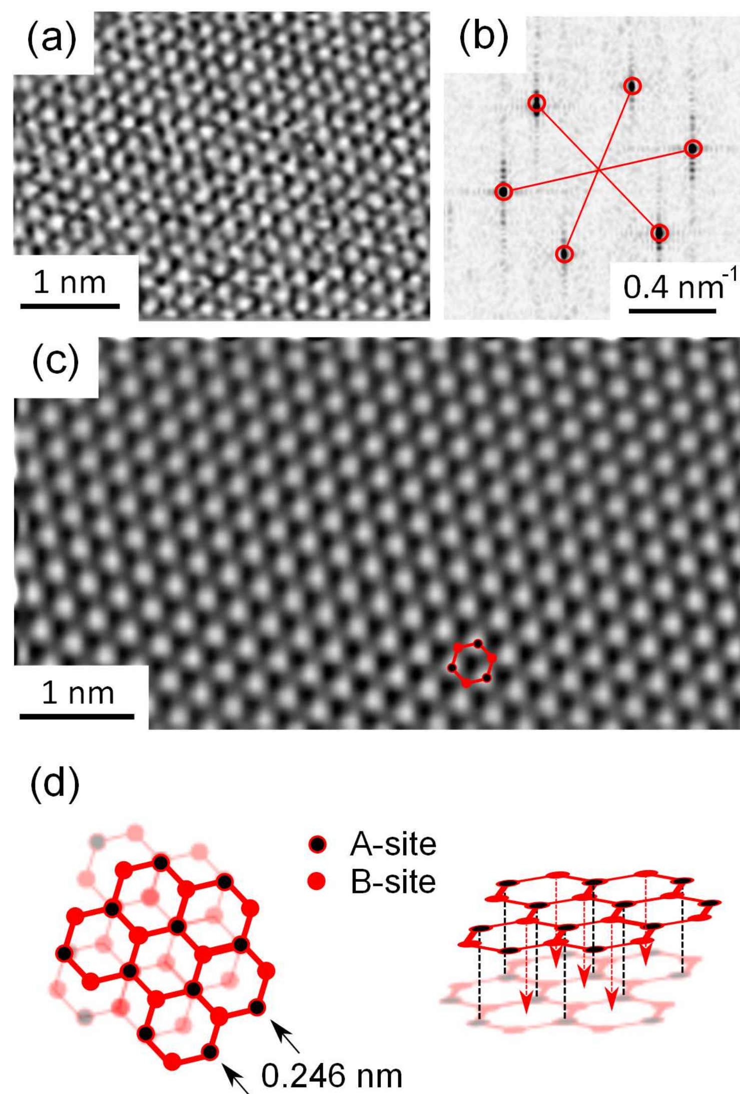

Figure 2.2: (a) Raw data STM image of the HOPG(0001) surface. (b) Fast Fourier transform of (a). (c) FFT filtered image of the HOPG(0001) surface. The graphite structure has been overlaid. (d) Schematic of the graphite crystal structure. A-site atoms correspond to those that sit directly above another carbon atom from the layer below. B-site atoms sit directly above a void.

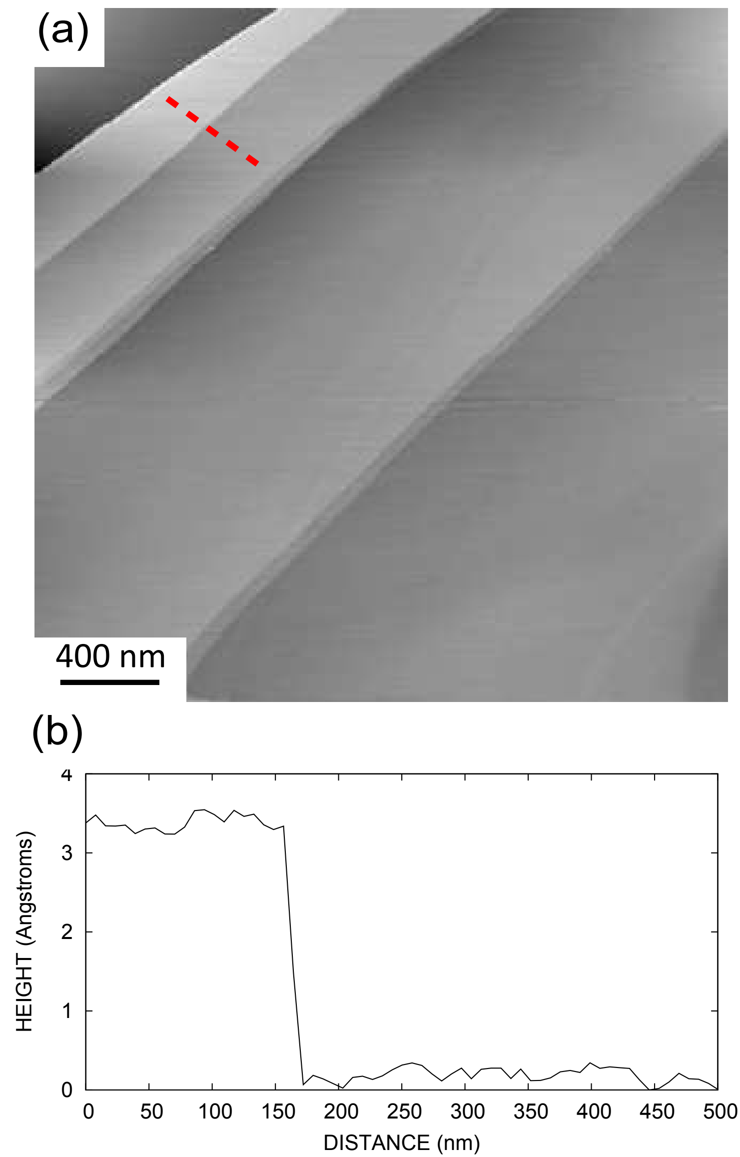

Figure 2.3: (a) Large area STM image of the cleaved HOPG(0001) surface. The cleavage is not perfect and large flat terraces are formed, separated by steps. (b) Line profile along the dashed line in (a). The step height is 3.35 Å.

main advantage of this method is that it gives higher signal to noise ratios, unfortunately capacitance effects have to be actively compensated, which means more complex electronic equipment is required [40]. Due to limitations within our equipment we could not implement the latter (lock-in) method, so we used the former technique which produced perfectly adequate results. All STS measurements were performed at constant height and in the dark.

2.2 Tip Preparation

The preparation of sharp, clean tips as required for STM studies is the most important factor for good imaging performance. Unfortunately, it is also the most difficult part in STM experimentation. The main difficulties lie in irreproducibility of the imaging capabilities of tips produced in the same manner. Often one tip prepared by a particular method will produce good quality images, whereas a second tip produced using the same method may have poor imaging capabilities. In this thesis we have used two different types of tips produced by different methods: Platinum-Iridium tips made by cutting wire and tungsten tips produced by electrochemical etching. Both have their relative advantages and disadvantages and we will discuss them in turn.

Cutting alloyed platinum-iridium (90:10) wire at oblique angles can often produce tips with excellent imaging capabilities [17]. Practically, a more of a ripping/cutting method using relatively blunt wire cutters, such that small asperities can form at the very apex of the tip, generally works well. On the macroscopic scale, tips produced in this manner look very dogged, however the asperities that protrude from the end of the tip can have very small radii and give good imaging performance. As was discussed in Section 1.3, the tunnel current is exponentially dependent on the tip-sample separation; so if one of the asperities protrudes further than all the others by only 1 nm, then this will contribute to 99.9% of the overall tunnel current, thus making all the others obsolete. Having said that, this preparation method is prone

to making so-called 'double tips' which can produce double-convolved images. This effect can generally be removed by soft crashing the tip into the surface typically removing one of the asperities. The advantage of producing tips in this manner is that it is quick and easy. Furthermore, used tips can be recycled by simply cutting off the end of the wire once again. In addition, platinum is a very unreactive metal so no oxide layer forms, meaning the metallicity of the tip is high allowing for good imaging performance. The disadvantage is that the preparation method is quite irreproducible; it is wise to prepare a number of tips and load them into vacuum simultaneously, just in case one or more of the tips is poor.

Electrochemical etching of tungsten wire can give more control over the tip preparation process [41, 42]. Practically, tips are formed by immersing a piece of polycrystalline tungsten wire to a depth of 1 cm into a 1 molar solution of sodium hydroxide. An electrical current is passed through the system using a stainless steel counter electrode. At the air-liquid interface, the wire is preferentially etched (forming tungstate WO_4^{2-} ions) and eventually it is completely etched through such that the bottom piece falls off, leaving the top piece with a sharp point. It is essential to immediately stop the current at the drop off point; otherwise the apex of the tip is blunted because it is still in contact with the surface of the liquid and would be etched away. To do this an electronic circuit is employed to monitor the current such that when a certain threshold is reached, the circuit is broken. The cut-off time is important to produce the sharpest tips and the circuit employed in this case has a cut-off time less than 50 micro seconds. A circuit diagram of the cut-off circuit can be found in reference [41]. Typical SEM images of tips produced in this manner are shown in Figure 2.4.

Unfortunately, etching in oxidising solutions allows tungsten to readily form an oxide layer, which is very debilitating to tip performance. In-vacuum annealing, either by direct resistive heating or electron bombardment, is often performed to remove this oxide layer [42, 43]. Unfortunately due to limitations

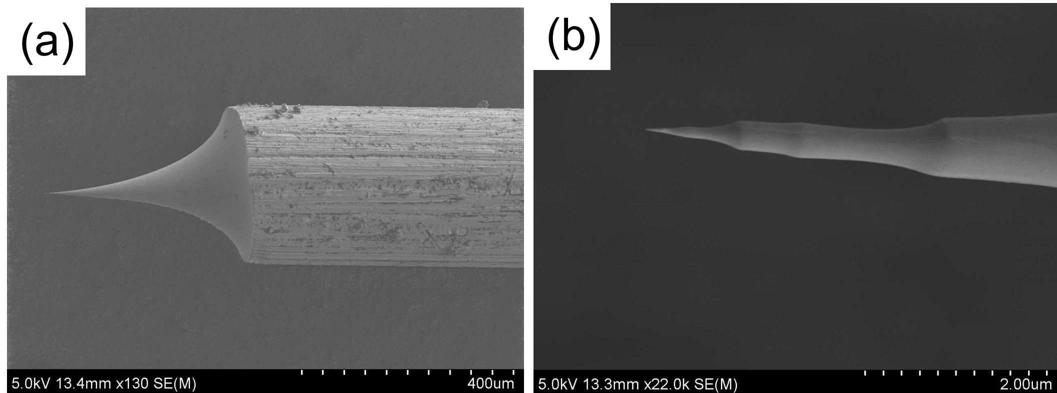

Figure 2.4: SEM images of typical electrochemically etched tungsten tips. (a) Large area (b) small area showing the apex of the tip.

within our equipment, it was not possible to implement these methods. Instead, we have employed a different in-situ preparation technique that involves making a controlled contact onto a clean metal surface. The contact allows clean metal atoms to be picked up onto the end of the tip forming a sharp, reliable tip [44]. In order to do this, a thin gold film was thermally evaporated (ex-situ) onto a sample plate. This surface was then argon ion sputtered to remove surface contaminants. The tip was repeatedly scanned across the clean surface and at random locations indented into the surface by 1-2 nm. This is repeated several times until a very stable tunnel current is measured.

2.3 The Atomic Force Microscope

We use a non-contact AFM that is designed in such a way that the same tube scanner can be used for both AFM and STM studies. Measurements are performed using Omicron Needle Sensor tips. This type of AFM is a non-contact method which uses the change in phase of an oscillating tip as a feedback signal [45, 46]. Silicon AFM tips are glued to a quartz crystal (see Figure 2.5) which has a sinusoidal voltage applied to it. The tip oscillates at high frequency and the interaction with the surface causes a phase shift in the oscillations which is measured using a lock-in amplifier. This phase

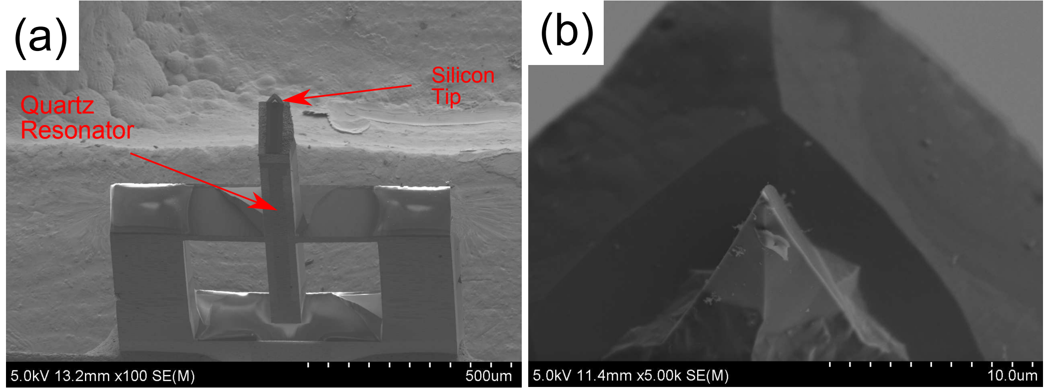

Figure 2.5: SEM images of Omicron Needle Sensor AFM tips. (a) Overview showing the quartz resonator and glued AFM silicon tip. (b) Detail of the tip apex.

shift can be used as a feedback signal. We use a fixed phase shift of -7° at a resonance frequency of ∼1 MHz. This method negates the requirement for a deflection laser allowing for an easier and simpler experimental set-up. All AFM measurements were performed in UHV conditions.

At various stages throughout this thesis, statistical analysis of the surface roughness has been calculated from AFM topographic images. AFM images were used for this analysis because (as was identified in Section 2.1) the STM is sensitive to the surface charge density rather than the atoms themselves, and thus would give erroneous results. We have used the root mean square (RMS) roughness which is calculated according to:

$$R_q = \sqrt{\frac{1}{MN}\sum_{j=1}^{N}\sum_{i=1}^{M} z^2\left(x_i, y_j\right)} \tag{2.1}$$

Where $z\left(x_i, y_j\right)$ is the topographic height at point $\left(x_i, y_j\right)$. The RMS roughness has been used to compare various surface preparation methods. In order to precisely represent the surface roughness, AFM topographic images are measured over an area that is much greater than the size of the surface features. Careful consideration to ensure images have been planed and flattened such that false height data is not included.

2.4 Ion Sputtering System

Argon ion sputtering has been used to prepare clean surfaces in vacuum. The system consists of an ion source on a 2.75" Conflat flange mounted to the main vacuum system. Argon ions impinge on the end of rotatable manipulator where the sample is mounted. The experimental set-up is schematically shown in Figure 2.6. Argon atoms are ionised by collisions with electrons from a burning discharge between cathode and anode (U $\approx$ 500 V). A magnetic field extends the electron's path length, thus increasing the number of collisions. The ions are accelerated by a voltage of a few kilovolts towards the sample surface. The beam is focused by a set of biased lens electrodes. The target sample is kept at ground potential to prevent charge build up. The beam energy is given by the acceleration voltage applied to the cathode (usually specified in kilo electron volts, but experimentally given by the bias applied to the cathode, in kilo volts); whilst the beam current is given by the number of ions leaving the source per unit time (specified by measuring the current at the sample mount). The sputtering is performed at a chamber pressure of $\sim 1 \times 10^{-5}$ mbar where the argon gas is admitted via a leak valve into the front of the sputtering source. During the process the whole chamber is pumped by the turbomolecular pump and after sputtering, the leak valve is closed and the argon is pumped away. UHV conditions (low 10^{-9} mbar range) can be achieved within 30 minutes after sputtering.

As will be discussed in the next chapter, annealing of the samples is a necessary step after argon ion sputtering to restore the surface crystallography, as well as remove absorbed contaminants. This annealing step is performed in-situ on the manipulator arm. The backside of the sample plate is resistively heated by a pyrolytic boron nitride heater mounted within the sample stage on the manipulator arm. The temperature is measured by a nickel-chromel thermocouple mounted on the same sample stage. The heater has a temperature range from room temperature up to 1100 °C. However for CdTe, temperatures

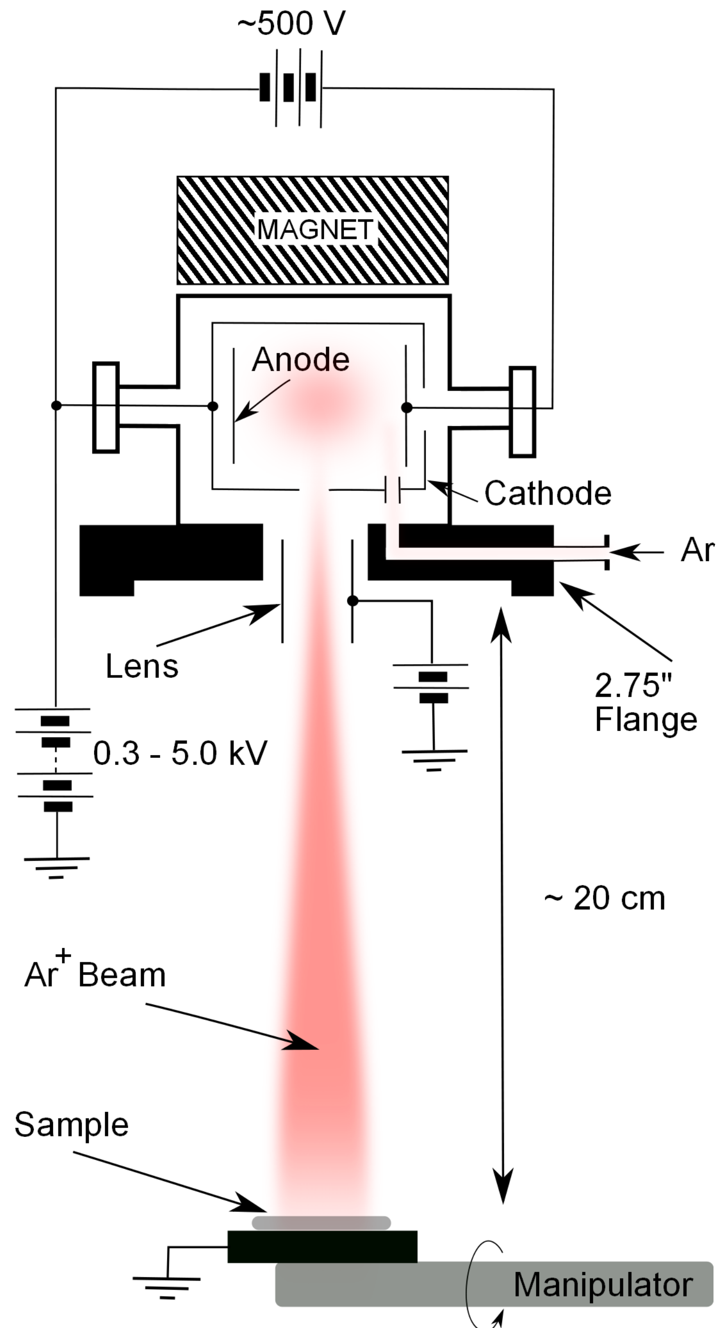

Figure 2.6: Cold-cathode argon ion sputtering gun and manipulator. A discharge is burning between cathode and anode (U ≈ 500 V) where the argon ions are produced by electron impact. A magnet increases the electron's path length and a biased lens is used for beam focusing. The ion beam impinge's onto a grounded rotatable manipulator arm where the sample sits.

below 400 °C are generally sufficient. All annealing steps are performed in UHV conditions.

2.5 Crystal Growth

All of the CdTe and CdZnTe crystals studied in this work were grown in our laboratory. Growth was performed from the vapour phase using either closed space sublimation (CSS)[47], hot wall epitaxy (HWE)[48] or the multi tube physical vapour transport (MTPVT) method[49]. All three methods use a semi-open system whereby the growth interface is continuously pumped allowing the removal of contaminants and un-stoichiometric material. They are all seeded growth methods, typically using foreign seed wafers, like GaAs or Ge, and the growing crystal is kept away from the ampoule walls, allowing stress free growth. All crystals were undoped with a high level of purity. The basic details of the crystal growth set-up and growth processes are described below.

The CSS set-up is the most simple, whereby a CdTe source is evaporated and condensed onto a substrate that is in clear line of sight. This deposition method is more commonly used in the production of CdTe based solar cells. However in this situation, single crystal substrates are used, such that the growth is epitaxial, and the source-substrate distance has been lowered to about 1 mm, which improves crystal quality. Unfortunately, the thickness of the films is limited to a maximum of about 300 μm. The main advantage of this method is that it is very quick and easy; a typical growth run can take less than 24 hours. HWE is performed in a similar manner, but this time the source-substrate distance is very large, typically about 20 cm. The main advantage of this method is that the source and substrate temperatures can now be controlled more precisely, unfortunately there are difficulties in getting sufficient vapour pressure build-up at the seed crystal for nucleation. As a consequence, higher substrate temperatures are required, and a typical

growth run may take a couple of days, however thicker crystals can be grown. The MTPVT method is the ultimate advancement of the vapour phase growth technique. In this situation, the source and substrates are completely separated in different 'tubes' allowing very precise control over the growth and source temperatures. The 'tubes' are connected by a crossmember that contains a small capillary. This capillary effectively separates the vapour pressures between the two tubes. Because the vapour flow rate is proportional to the capillary radius to the power four, all other variables are suppressed allowing for controlled growth [50]. Using this method very thick, bulk crystals can be grown. A typical growth run produces boules of 50 mm diameter and 10 mm in thickness. To grow such thick crystals, a typical growth run may take longer than 1 week. In addition, a third tube can be installed allowing for the introduction of extrinsic dopants. For example, a third tube containing a source of zinc telluride (ZnTe) can be used to grow CdZnTe crystals. Indeed, all of the CdZnTe crystals studied in this work were grown by the MTPVT method.

Schematic diagrams of the three individual crystal growth set-ups are shown in Figure 2.7. Characterisation of the grown crystals was performed using X-ray diffraction, infrared microscopy and transmission, photoluminescence and current-voltage characterisation. These were mostly performed by my colleagues, and, where applicable, these results have been published [47, 48, 49]. Generally, all three growth methods produced high quality single crystals that were more than adequate for STM studies. Sample preparation after growth usually involves cutting, mechanical polishing, etching in bromine methanol solutions and finally the deposition of ohmic metal contacts. The details of these preparation methods are given, where relevant, in the following chapters.

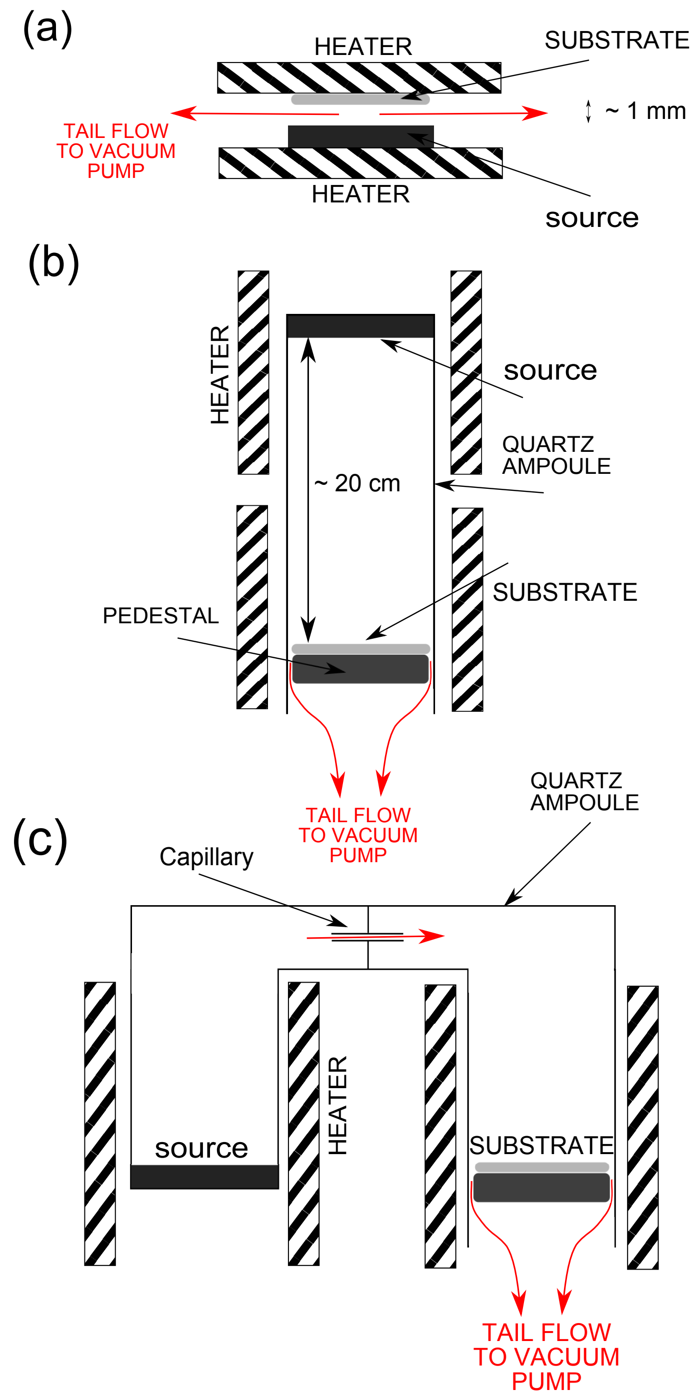

Figure 2.7: Schematic diagrams of the growth equipment used to grow the crystals used in this thesis. (a) CSS (b) HWE (c) MTPVT.

2.6 Summary

This chapter has described the experimental techniques and equipment used in this thesis. The scanning tunneling microscope and the UHV chamber in which it is housed has been described in detail. Calibration of the STM scanner was performed by imaging the atomic structure of the HOPG(0001) surface. During this process the sensitivity of the STM to surface charge density, rather than the individual atomic positions was identified. The z-axis calibration of the scanner was performed by imaging atomic height steps produced after cleavage of the HOPG(0001) surface. Tip preparation has been identified as a very important step for good experimental results. We have described the methods used to produce sharp tips as required for STM imaging and discussed their relative advantages and disadvantages. The atomic force microscope used in this work has been described along with typical analysis methods. The argon ion sputtering system that has been used to prepare clean surfaces in vacuum has been described. Finally the crystal growth techniques used to grow the single crystals has been outlined.

In the following chapters we systematically investigate the atomic arrangement of the low index surface planes of CdTe. We start in the next chapter by looking at the CdTe(100) surface. This surface is the most studied of all the principle crystallographic faces of CdTe, and thus is a good experimental starting point. Prior to this, we will look at what is required to prepare a clean surface in vacuum, i.e. using the argon sputtering system described above. Then we will investigate the atomic structure of the surface after this treatment.

Chapter 3

The (100) Surface

3.1 Introduction

This chapter concerns the study of {100} orientated surfaces of CdTe crystals. Like the GaAs(100) surface, the CdTe(100) surface is often used as a substrate for epitaxial growth in MBE systems. Indeed, MBE growth of HgCdTe films (for IR detector applications) is usually performed on CdTe(100) or the more lattice matched CdZnTe(100) substrates [51, 52]. Because of the lack of inversion symmetry in the zincblende structure, the {100} surface planes are polar. In practice this means that the {100} surface planes can either be completely covered in a monolayer (ML) of cadmium or a ML of tellurium atoms, as shown in Figure 3.1. For either termination, atoms sit on bridging sites bonded to two atoms from the layer below, as such, each surface atom has two dangling bonds. The (1×1) surface unit cell has dimensions of 4.580 Å along both the $[1\bar{1}0]$ and [110] directions, i.e. it forms a 2D square lattice.

Because of its strong practical applications, the CdTe(100) surface is by far the most studied of any of the low index surfaces, especially using techniques like LEED, RHEED, STM and AES. Using such techniques, a mixed cadmium-rich $c(2 \times 2)+(2 \times 1)$ reconstruction with a cadmium coverage of 0.5 monolayers (ML) has been found to be stable over a wide temperature range [53]. Under special preparation conditions (high tellurium flux, low annealing

temperatures) a tellurium-rich (2×1) reconstruction has been observed with a tellurium coverage of 1.5 ML [54]. These structures have also been predicted by first principles total energy calculations. Based on these calculations, the surface energy of the cadmium-rich $c(2\times2)$ and (2×1) reconstructions were found to be very similar, thus explaining the mixed surface phase. The tellurium-rich (2×1) reconstruction was only found to be stable for low tellurium chemical potentials [55]. Based on STM measurements, this mixed surface phase was found to consist of small domains of the $c(2 \times 2)$ and (2×1) phases separated by domain boundaries that run parallel to <110> directions [56].

In this chapter we investigate the surface morphology and surface reconstructions of CdTe(100) surfaces. The aim was to build upon the work from previous research and add to the understanding of the surface physics. The chapter is roughly split into two sections: The first part concerns the preparation of clean, well-defined surfaces using argon ion sputtering and annealing. Here we investigate the variation of the surface morphology with different ion energies and fluxes. In the second part, we look at the surface reconstructions of the (100) surface, i.e. the surface crystallography formed after annealing sputtered surfaces. We then expand upon this, by discussing vicinal CdTe(100) surfaces.

3.2 Preparation of Well Defined Surfaces

Before we can investigate the specific surface reconstructions of a surface, we need to prepare a clean, well defined surface in vacuum, such that it can be imaged on the atomic scale using the scanning tunneling microscope. This is the topic of discussion for the next section.

3.2.1 Introduction

Clean surfaces, as required for STM imaging, can be prepared in a number of ways: evaporation or molecular beam epitaxy (MBE) of thin films in UHV;

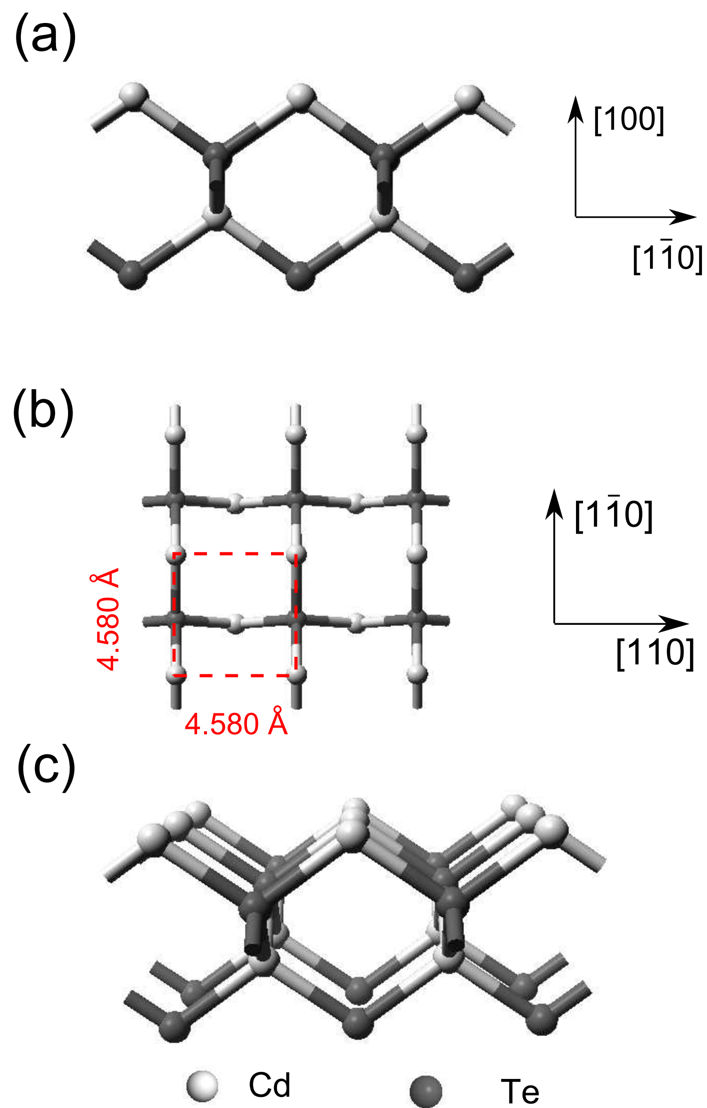

Figure 3.1: Atomic structure of the bulk terminated (100) surface of CdTe. (a) Side view looking along the [110] direction. (b) Top view with the (1×1) surface unit cell shown by the dashed square. (c) Perspective view looking along the [110] direction.

sample cleavage in UHV; or ion bombardment and annealing [1, 3]. The first method requires expensive equipment and a devoted system for the growth of good quality films in a vacuum environment. The second method is usually limited to particular materials and surface orientations. For example, the cleavage plane for silicon is the (111) plane whilst for CdTe it is the (110) plane [1]. In any case this method is still relatively difficult to employ since it requires mechanical feedthroughs that can be controlled from outside the chamber and may also require an elaborate sample holder set-up. The most versatile method to prepare clean well-defined surfaces is via ion bombardment and annealing. Surface contaminants, oxide layers and usually the topmost surface layers can be sputtered off by bombardment of the surface with noble gas ions like argon or neon. This bombardment is usually followed by annealing which is a necessary step required to remove embedded or absorbed noble gas atoms and to recover the surface crystallography. During this process, the surface cleanliness is usually monitored by AES whilst the surface crystallography is inspected by LEED. Often repeated cycles of ion bombardment (sputtering) and annealing may be required to result in a clean and flat surface as required for STM imaging. Furthermore, surfaces prepared by sputtering may be of interest to those studying metal contact deposition in vacuum.

Unfortunately, due to limitations within the current vacuum system, AES and LEED equipment could not be implemented. However, sputtering and annealing is a well defined and reproducible process, and it's very easy to build upon previous results and findings. As described above, the (100) surface of CdTe is by far the most studied surface especially by STM, and thus provides a good starting point for further study.

Yong et al.[57] recorded Auger electron spectra for CdTe surfaces prepared by argon ion sputtering and annealing and the results are shown in Figure 3.2. The spectrum after chemo-mechanical polishing [Figure 3.2(a)] shows surface contaminants of oxygen, carbon and chlorine. These are likely from residual chemicals absorbed onto the surface after surface preparation and/or from

surface exposure to the atmosphere. After sputtering [Figure 3.2(b)] these contaminants are fully removed. Note however that the carbon peak, although reduced in magnitude, still remains. In actuality, the carbon peak coincides with a sub-peak from the cadmium line. The cadmium sub-peaks exist at energies of 277 eV and 321 eV, respectively. The 277 eV peak nearly exactly corresponds to the carbon line and thus can be concealed. However the 321 eV peak can be clearly seen in the spectra, and this peak has a pronounced increase in intensity after sputtering. Thus the removal of surface defects and contaminants has allowed the cadmium peak to become more visible. This is also shown by the increase in intensity of the principal cadmium MNN line. Finally, note that a very small peak at about 216 eV has appeared. This corresponds to argon, and is presumably resultant from argon ions embedded within the surface after sputtering. After annealing at 330°C [Figure 3.2(c)] no real change in the shape of the spectra is observed, although the very small argon peak appears to have disappeared implying this contaminant has been removed. The annealing step is necessary also to recover the surface crystallography. No LEED patterns are ever observed after simply sputtering a surface. In addition, the surface cleanliness has no real surface plane orientational dependence, as demonstrated Figure 3.2(d). This spectrum was recorded on a sputter-annealed CdTe(110) surface and no major differences are observed.

These conclusions are also broadly the same for sputtered and annealed CdZnTe surfaces, as shown in Figure 3.3. This data was recorded by Neureiter et al.[53] on a $Cd_{0.96}Zn_{0.04}Te$ wafer, i.e. one that is perfectly lattice matched for HgCdTe epitaxy. The data in this case is somewhat better than that presented in Figure 3.2, but the main conclusions still apply. In this case, a lower beam energy and annealing temperature was used to prepare the surface, however (as was well demonstrated by those authors) a clean and well defined surface could still be produced. One interesting conclusion from those authors was that the surface was *not* zinc enriched after sputtering, however after annealing, particularly at temperatures greater than 350°C, a significant zinc

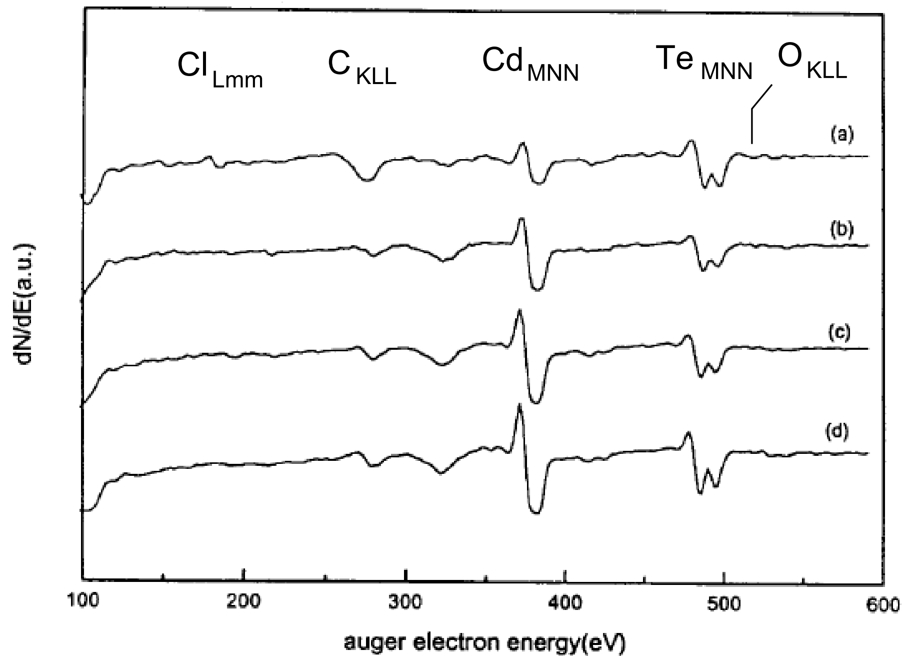

Figure 3.2: Auger electron spectra from a CdTe (100) wafer. (a) Chemo-mechanically polished (b) After argon ion sputtering for 10 min at 1.2 KeV(c) and after subsequent annealing at 330°C for 5 min. (d) The same preparation as for (c) but on the CdTe(110) surface. Reproduced and modified from Yong et al.[57].

enrichment was observed.

Although the cleanliness and crystallography of sputtered and annealed surfaces is well documented, no studies have systematically investigated the surface *morphology* for sputtered surfaces. In particular what is the morphological dependence on the ion beam energy, incident angle or flux? We perform this study here, by varying the angle of incidence, the excitation energy and flux on the sample sample surface.

3.2.2 Sample Preparation

For this study, a number of different samples of varied surface orientations were looked at. The majority of the samples had a (100) surface orientation, however other samples with different surface orientations were also studied for

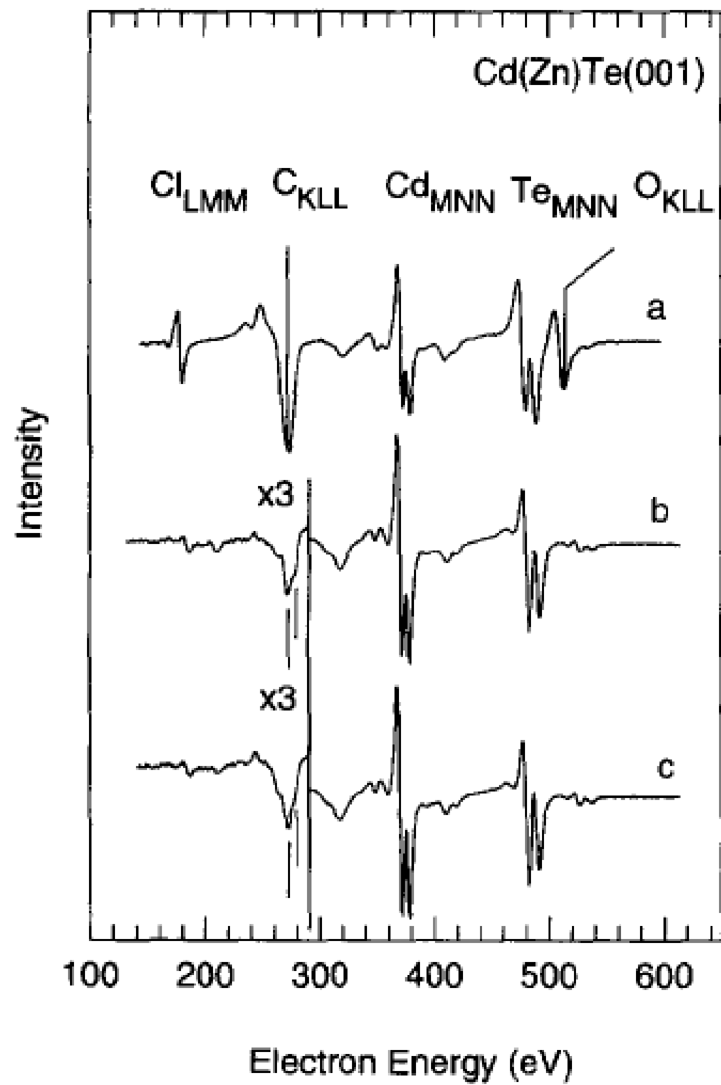

Figure 3.3: Auger electron spectra from a CdZnTe (100) wafer. (a) As-received (b) After argon ion sputtering for 10 min (c) and after subsequent annealing at 300°C for 5 min. Reproduced from Neureiter et al. [53].

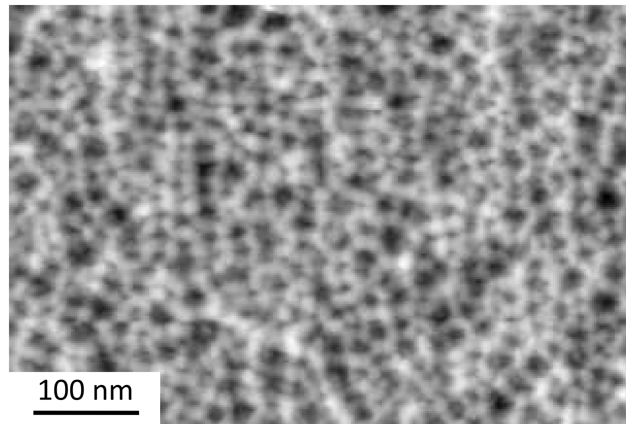

Figure 3.4: AFM image of an argon ion sputtered CdTe(100) surface using a beam energy of 2 keV and flux of 10 μAcm^{-2} at normal incidence. The image is shown on a grayscale range of 14 nm.

comparison. They were all grown either by HWE or CSS, as described in Section 2.5, and all showed good crystal quality with no obvious difference in quality between the two growth methods. All samples were polished using a diamond suspension with a final particle size of 0.1 μm and then etched in a 2 % bromine methanol solution for 2 minutes. This produced very shiny, mirror-like surfaces. Samples were then mounted in a molybdenum sample holder and loaded into UHV via a fast entry load-lock. Argon ion sputtering was performed as described in Section 2.4 and the surface morphology was subsequently studied by AFM in non-contact mode, as described in Section 2.3.

3.2.3 Results and Discussion

Figure 3.4 shows the surface morphology of an argon ion sputtered CdTe(100) surface. The sputtering was performed at normal incidence using a beam energy of 2 keV, a flux of 10 μAcm^{-2} for 30 minutes. The surface shows a globular structure with no orientational dependence. There are no structural features like step edges or terraces, and suggests that the surface is amorphous. Indeed, no electron diffraction patterns are ever found for simply sputtered

surfaces. Sputtering was also performed on different surface orientations (for example the (110) and (111) surfaces) but no obvious differences were found in the surface morphology. This surface was prepared using a beam of normal incidence, however by changing the angle of incidence we can drastically change the surface morphology, as shown in Figure 3.5.

We see that for normal incidence the surface shows a globular structure with no orientational dependence. For grazing incidence the surface shows a strong ripple-like structure with the ripples being parallel to the beam direction. Rotation of the sample with respect to the beam appears to make no change in the ripple formation. The ripples are always found to be parallel to the beam direction. The ripple wavelength increases for a more grazing incident beam reaching a maximum value of about 25 nm. Indeed rippling is observed for even slight mis-orientation from the normal, with an angle of 20° from the normal giving a ripple wavelength of about 16 nm. Figure 3.6(a) shows the RMS roughness as a function of incident angle, we see that the surface roughness is reduced for a grazing incident beam, producing a 50 % smoother surface for a 10° grazing angle. The rippling shows no surface orientational dependence, i.e. we observe the same effect for other surface orientations like the (110) and (111) surfacess.

This rippling effect is a well known phenomenon observed on a variety of different materials and surfaces. The theory and understanding behind the surface rippling effect is now well established (albeit very complicated) and the phenomena can be controlled and exploited to pattern surfaces without using external masks or templates. For example, quantum dots have been observed to self-organise on GaSb surfaces after ion sputtering [58]. For the purposes of this thesis we only provide an outline of the basic processes behind the phenomena, the reader is referred to the review article by W. L. Chan and E. Chason [59] for further information. The morphology of sputtered surfaces is essentially controlled by the dynamic competition between that of roughening (sputtering atoms off the surface) and smoothing (diffusion of

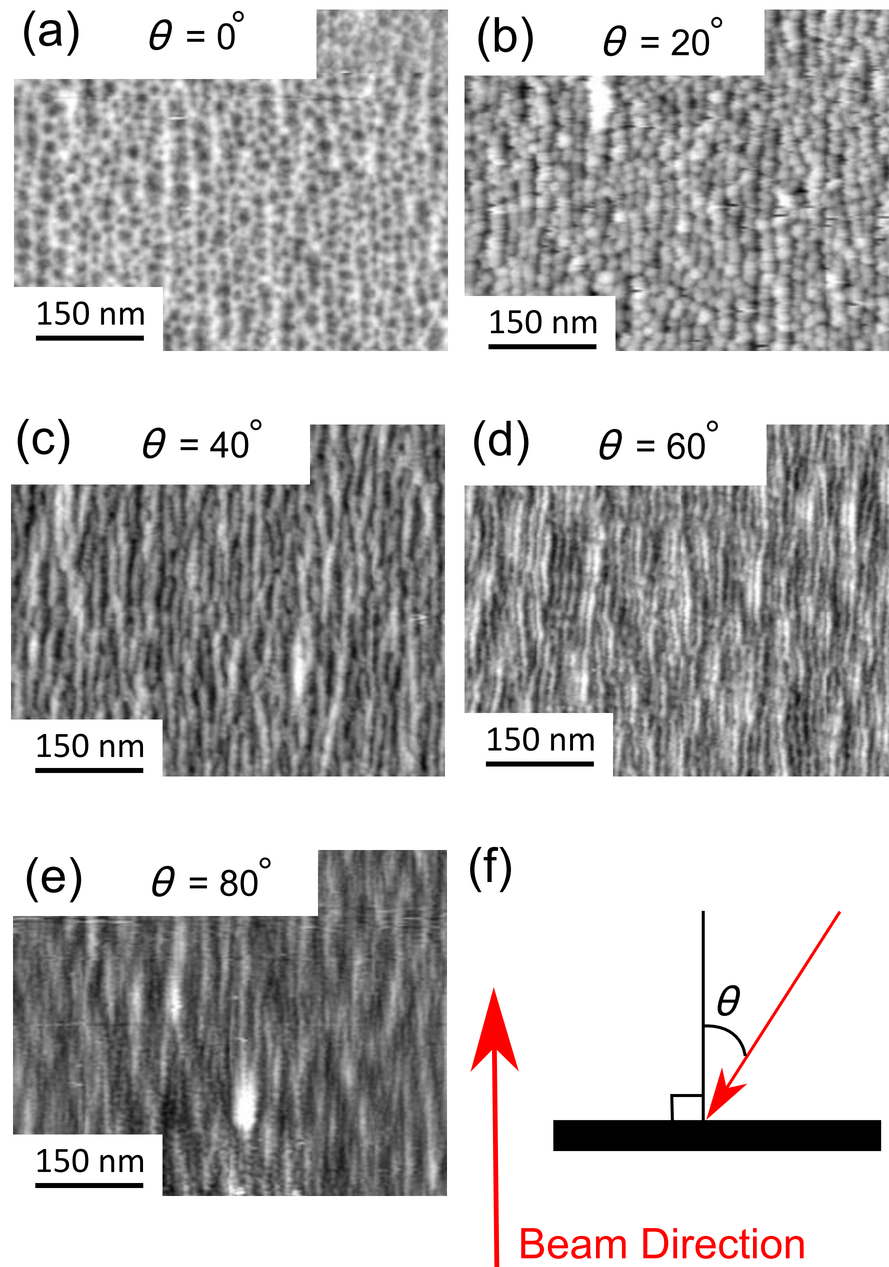

Figure 3.5: Surface morphology of argon ion sputtered CdTe surfaces as a function of incident angle. Angle of incidence given relative to the surface normal as: (a) 0° (b) 20° (c) 40° (d) 60° (e) 80°. The beam direction and schematic diagram for all images is shown in (f).

defects and atomic species) processes. The variation of these two processes with temperature, ion flux, ion energy and incident angle defines the resultant surface morphology. For the present case, where the surface patterning appears to be controlled solely by the ion beam, rather than the surface crystallography, indicates that we are in the so-called Bradley-Harper (BH) instability regime [60]. In the BH regime, the morphology is described by curvature dependent sputtering coupled with surface diffusion that is not barrier limited. Bradley and Harper found that the sputtering yield at a particular point on the surface was proportional to the local surface curvature at that point. So a point with positive curvature (bottom of valleys) has more material removed from it compared to a point with negative curvature (top of hills). This leads to an instability that tends to increase the rate of roughening with increasing surface roughness. This rapid roughening is balanced by surface diffusion which acts to smooth the surface. This results in a surface morphology that has a characteristic wavelength that depends upon the sputtering conditions (e.g. temperature, incident angle etc...). One property of the data presented here is that the ripples form *parallel* to the ion beam at all incident angles. In fact, ripples are known to form either parallel *or* perpendicular to the ion beam depending upon certain ion beam/material parameters. Typically, ripples are observed to form perpendicular to the ion beam below some critical angle of incidence and form parallel to the ion beam above this angle [61]. For CdTe however, we observe no rotation of the ripple direction implying a slightly more complex theory is required to explain the sputtering processes on this surface.

For diffusion processes that are highly barrier limited (i.e. a relatively large energy barrier has to be overcome before diffusion can occur) display drastically different surface morphologies that cannot be explained by the BH theory. For this regime (known as the ES instability regime - named after Ehrlich and Schwoebel who first proposed diffusion barriers[62, 63]) the surface patterning shows a strong crystallographic orientational dependence for pattern formation (rather than the ion beam controlling the surface pattern-

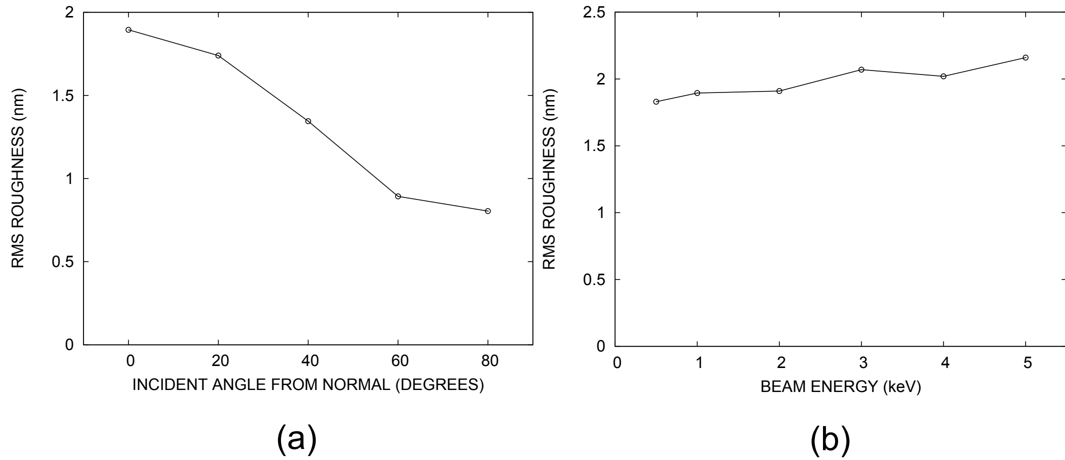

Figure 3.6: (a) RMS roughness of sputtered surfaces as a function of incident angle. The beam energy and flux was kept constant at 1 keV and 8 μAcm^{-2}, respectively. (b) RMS roughness of sputtered surfaces as a function of incident beam energy. This data was recorded for normal incidence beam using a constant flux of 8 μAcm^{-2}.

ing). This type of patterning is very common on metal surfaces and can result in the formation of surface pits and/or ripples that show no dependence with the orientation of the ion beam, but rather some principle crystallographic direction. There are numerous other erosion regimes which are described by complex theoretical models (e.g. to describe the self-organisation of quantum dots on semiconductor surfaces[58]), but the BH and ES regimes are the two most common.

For the present case, we do not attempt to match the observed ripple wavelength or ripple amplitude to that predicted by the BH model, since it is outside the scope of this thesis. Instead we simply acknowledge that ripple formation occurs on sputtered CdTe surfaces and we have a basic theoretical knowledge to explain it.

Figure 3.6(b) shows the effect of the incident beam energy on the surface roughness. We see little effect on the surface morphology as a function of energy. We observe a slight increase in roughness for higher energy beams, however this effect is weak compared to that of the incident angle. From this it appears that using lower beam energies (e.g. less than 1 keV) should

produce a smoother surface. However, some previous results from AES experiments suggest that low beam energies do not have sufficient cleaning power [64]. Considering this, we chose to use an incident beam energy of 1 keV. This energy should have sufficient cleaning power whilst not increasing the roughness too much. Furthermore, these results agree with those found from other authors [64]. The use of a higher beam energy may cause argon ions to be deeply implanted into the surface and thus would require higher annealing temperatures to remove.

The flux of the incident beam appears to show a much stronger effect than the beam energy, as shown in Figure 3.7. This surface was prepared by sputtering with a beam energy of 5 keV and flux of greater than 40 μAcm^{-2}. The surface has a deeply pitted morphology interspaced with relatively flat regions. The pits are very deep, typically greater than 100 nm and appear to be spherically symmetric with diameters of up to 1 μm. We also observe some extended features, although they typically still have similar widths. In between the etch pits, the surface remains relatively flat, on a par with that found for low flux etching. We believe that these features are most likely resultant from preferential etching of surface defects that intersect the surface: either dislocations, inclusions, precipitates, or sub-grain boundaries. This type of etching may prove to be a useful *dry* defect etching mechanism, similar to standard wet chemical defect etching methods. However, at the this time the etching mechanism is still not clear and requires further work. Therefore, in the context of this thesis, the use of high energy, high flux ion etching is really just an interesting aside. For the purposes of the preparation of a flat clean surface as required for STM studies however, we found that using a flux of less than 10 μAcm^{-2} produced good results.

3.2.4 Summary

To summarise, the surface cleanliness of CdTe surfaces has been demonstrated using AES by previous authors. We have built upon their work and have stud-

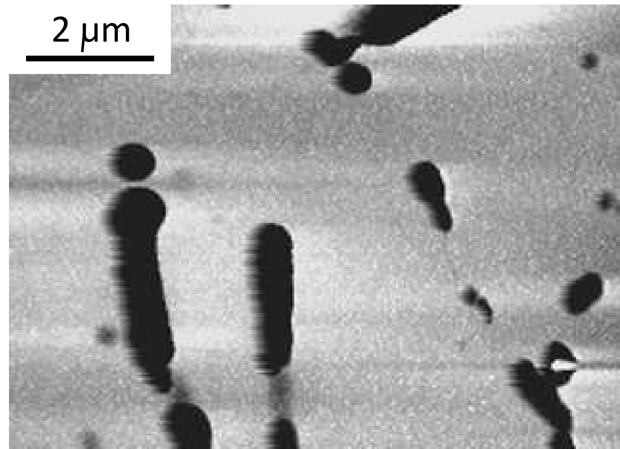

Figure 3.7: Large area AFM image a surface sputtered with a beam energy of 5 keV and flux of 40 μAcm^{-2}. The image is shown on a grayscale range of 130 nm. A background subtraction has been applied to emphasise the etch pits.

ied the effect of the incident angle, beam energy and beam flux of argon ion sputtering on the surface morphology. We observe that for a grazing incident beam a rippling effect occurs with the ripples lying parallel to the incident beam. The surface morphology shows little dependence on the surface orientation or beam energy for low fluxes. This phenomena can be explained by the Bradley-Harper erosion regime for surfaces that are not diffusion barrier limited. For high beam energy and flux we observed a novel defect etching mechanism, whereby deep holes were formed in the surface. For the purposes of atomic resolution imaging for STM studies, we have concluded that sputtering for 30 minutes using a beam energy of 1 keV and flux less than 10 μAcm^{-2} produces a sufficiently smooth, flat and clean surface.

Subsequent annealing of surfaces after ion bombardment is required to recover the surface crystallography and to allow increased surface migration to produce an atomically flat surface as required for atomic resolution imaging. Unlike ion sputtering, annealing is strongly surface dependent, with different surfaces producing different surface reconstructions for different annealing temperatures. This is a result of the atomic arrangement and stoichiometry of

the surface in question.

3.3 Surface Reconstructions Imaged by STM

Having outlined the requirements for the preparation of a clean, well defined surface, now let us build upon this and look at an example: the atomic structure of CdTe(100) surface. As was discussed in Section 3.1, the clean CdTe(100) surface shows a cadmium-rich c(2×2)+(2×1) mixed reconstruction. This has been observed for surfaces prepared by both MBE and sputter-annealing. For both methods annealing temperatures in the range of 250°C to 320°C have been used. In the following work we identify this mixed reconstruction using STM and then build on this work by looking at vicinal (100) surfaces.

3.3.1 Sample Preparation

(100) orientated undoped CdTe thick films were epitaxially grown on either GaAs(100) or Ge(100) substrates. To improve the crystal quality of the films, the substrates were offcut by 6° degrees towards the (111)A plane. The offcut angle is known to inhibit so-called *dual-epitaxy*, whereby grains of (100) and (111) orientated CdTe are formed [65]. These films were typically about 100 μm thick and showed good crystal quality. A typical Laue back reflection image of a thick film is shown in Figure 3.8. The offcut is clearly evident in the diffraction pattern whereby the central spot is off-centre. The offcut is measured to be $(6.5 \pm 0.5)^\circ$ towards the (111)A plane for this sample. Thus the crystal registry of the film is consistent with the substrate. After growth, the films were polished using a diamond suspension with a final particle size of 0.1 μm and then etched in a 2 % bromine methanol solution for 1 minute. This produced a very shiny, mirror-like surface. Samples were then mounted on a molybdenum sample holder and loaded into UHV via a fast entry load lock. The surfaces were then prepared by argon ion sputtering and annealing

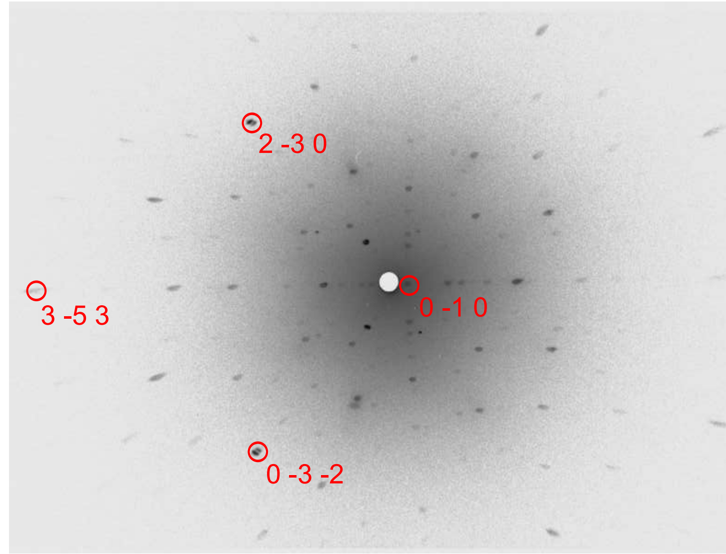

Figure 3.8: Laue back reflection diffraction pattern from a CdTe(100) film grown on an offcut GaAs(100) substrate. Key reflection indexes are identified. The central spot is shifted towards the right and the measured offcut is found to be $(6.5 \pm 0.5)^{\circ}$ towards the (111)A plane.

as described in the previous section.

3.3.2 Results and Discussion

A typical STM image of CdTe(100) surface prepared by argon sputtering and annealing at 275°C is shown in Figure 3.9. We can see that there exists a high number of steps that separate terraces. These are due to the offcut of the substrate, causing the (100) plane to be slightly inclined to the surface. On the terraces we observe a mixed phase of $(2 \times 1) + c(2 \times 2)$ reconstruction. This mixed phase consists of small domains, separated by phase boundaries. The unit cells for the (2×1) and $c(2 \times 2)$ are shown in the Figure. For the (2×1) reconstruction the periodicity along the $[1\bar{1}0]$ direction is measured to be about 9.4 Å i.e. consistent with a 2x periodicity in that direction. The periodicity along the [110] direction is more difficult to measure because the adatoms usually form rows in that direction, however good imaging combined with filtering techniques allows us to measure this. As expected, the surface periodicity is found to be about 4.7 Å, consistent with a 1x periodicity. For

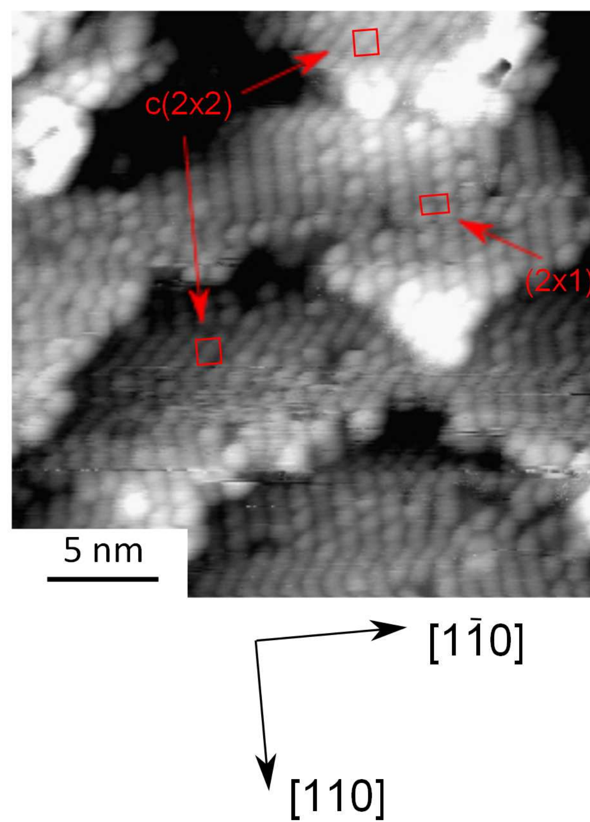

Figure 3.9: STM image of the CdTe(100) surface after sputtering and annealing.

the c(2 $\times$ 2) reconstruction a 2x periodicity was found in both the <110> directions.

These structures can be predicted using the electron counting rule. This rule applies to most binary semiconductor surfaces and successfully predicts the surface reconstructions [66]. The rule is based on counting the number of dangling bonds for both the anions and the cations per unit cell; then matching the number of dangling bonds by removal of a number of surface atoms; and finally redistributing the electronic charge within those dangling bonds to the most electronegative element. In this case, the ideal, bulk terminated CdTe(100) surface can either be terminated by 1 monolayer (ML) of cadmium or 1 ML tellurium, as shown in Figure 3.1. For the cadmium terminated surface there are two dangling bonds located on cadmium atoms and no dangling bonds on tellurium atoms (per unit cell). If one removes a cadmium atom for every (2 $\times$ 1) unit cell (i.e. the removal of one row of cadmium atoms along a [110] direction, leaving the surface with 0.5 ML of cadmium), then there are an equal number of dangling bonds on both the anion and cation per (2 $\times$ 1) unit cell: two dangling bonds located on cadmium atoms and two located on tellurium atoms. Now, electrons from the two cadmium dangling bonds are transfered to the two dangling bonds located on the more electronegative tellurium atoms. This leaves the cadmium dangling bonds completely empty, whilst the tellurium dangling bonds are completely filled. The resultant surface is now found to be very stable. This mechanism successfully predicts the majority of the surface reconstructions found on III-V semiconductors[66] and also appears to be the driving force for all of the surface reconstructions found on CdTe surfaces.

The electron counting rule successfully explains the CdTe(100)-(2 $\times$ 1) reconstruction, but what about the c(2 $\times$ 2) reconstruction? In fact this reconstruction can be made by translation of every alternate two-fold coordinated cadmium atom along the $[1\bar{1}0]$ direction. This surface has the same stoichiometry (0.5 ML cadmium) and thus still maintains the electron counting rule. In-

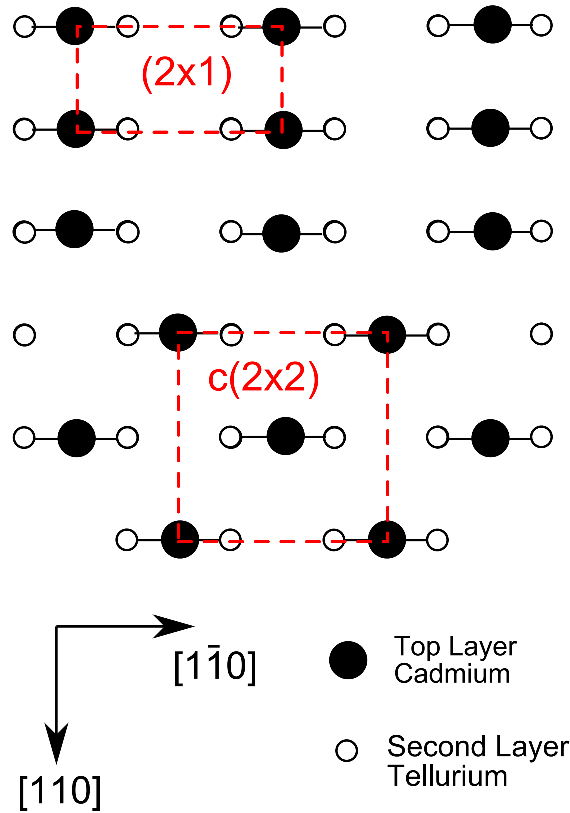

Figure 3.10: Atomic ball and stick model for the CdTe(100) surface reconstructions.

deed, these two structures are very similar and therefore the energy difference between them is predicted to be very small, as shown by first principle total energy calculations which explains the mixed surface reconstructions observed experimentally [55]. Atomic models for the (2×1) and c(2×2) reconstructions are shown in Figure 3.10.

These reconstructions are observed on terraces separated by steps. Line profiles across the steps show them to be 3.2 Å in height. This corresponds to one CdTe bilayer, thus implying the surface is either completely cadmium or tellurium terminated. From previous results the CdTe(100) surface is known to be more stable for the cadmium terminated structures. What is very evident from Figure 3.9 is that the steps are *not* straight. The steps have a zig-zag pattern with triangular shaped apexes. This is more evident if we look over a wider area as shown in Figure 3.11. Here we see that many of the step edges

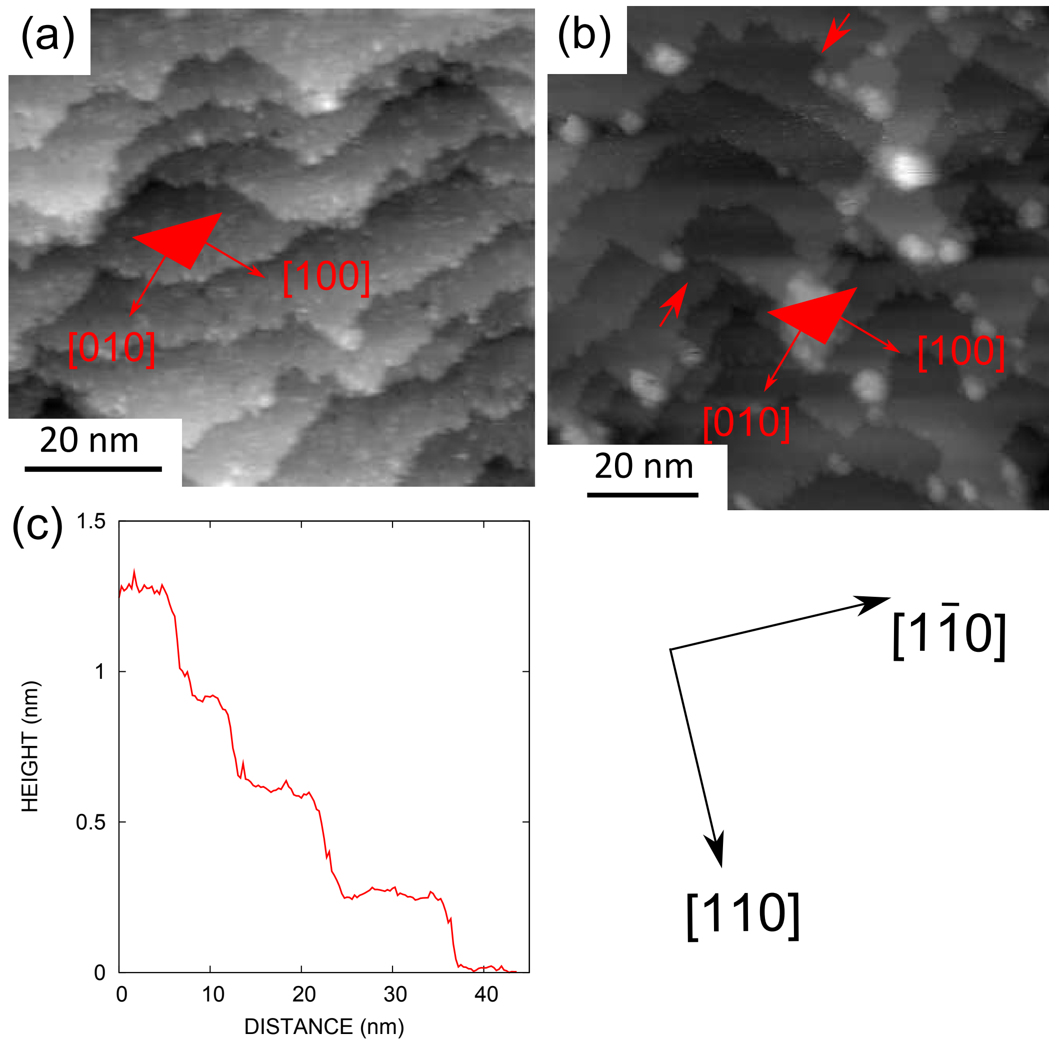

Figure 3.11: Large area STM images of vicinal CdTe(100) surfaces offcut towards the [111] direction. (a) and (b) two images taken at two different positions using two different tips. (c) Line profile taken between the arrows in (b).

are parallel to a <100> direction. Indeed this particular sample was grown on a Ge(100) substrate offcut by 6° towards the (111) plane. In theory this should produce steps with edges parallel to <110> directions. However this is not the case found experimentally and suggests that [110] type steps are unstable, and [100] type edges form preferentially. Indeed this result agrees with that found from Martrou *et al.*[67], who found that step edges are parallel to <100> directions forming parallel terraces for CdTe films epitaxially grown on wafers offcut towards the (110) plane.

3.4 Conclusions

In conclusion, we have outlined the necessary steps to prepare well defined surfaces as required for STM studies by using argon sputtering and annealing. The surface cleanliness of sputtered surfaces has been demonstrated from previous work, whilst the surface morphology of sputtered surfaces has been systematically studied. The optimum sputtering conditions were identified from our own results and from drawing on the work of previous authors. We found that the surface shows a rippled structure for a grazing incidence beam, whilst the surface roughness also reduced. The beam energy showed little effect upon the surface roughness, whilst the beam flux showed a stronger relationship. Based on this work we conclude that a 1 keV argon ion beam, with a flux of about 8 μAcm^{-2} and sputtering for about 30 minutes duration produced surfaces that were adequate for STM studies.

Subsequent annealing of sputtered surfaces restores the surface crystallography, and this has been demonstrated by directly imaging the atomic surface reconstructions of the CdTe(100) surface. This surface shows a mixed phase of $(2 \times 1) + c(2 \times 2)$ reconstructions consisting of two-fold coordinated cadmium atoms sitting upon the bulk terminated structure. We have outlined the electron counting rule which is a simple but powerful tool for predicting the surface reconstructions for binary semiconductors and explains the surface

reconstructions observed here by STM. Furthermore, we have studied vicinal CdTe(100) surfaces. We found that for surfaces offcut towards the (111)A plane the steps formed zig-zagged structures with edges parallel to the <100> directions. This implies that <100> type steps are energetically favourable.

The work in this chapter serves as a building block for the study of the other principal low index surfaces. The CdTe(100) surface is by far the most studied surface of CdTe and because of this it was chosen to be the first studied. In the next chapter we will look at the CdTe(110) surface which forms the cleavage plane.

Chapter 4

The (110) Surface

4.1 Introduction

The (110) surface of zincblende semiconductors forms the cleavage plane since the bond density between those planes is the lowest. It contains the same number of cations as anions and thus is intrinsically neutral. The CdTe(110) surface shows no reconstruction, with the (1×1) unit cell containing one cadmium and one tellurium atom, each of which has one dangling bond. The (1×1) unit cell has dimensions of 6.481 Å (i.e. the CdTe lattice parameter) along the [001] direction, and 4.583 Å along the $[1\bar{1}0]$ direction as shown in Figure 4.1. Although the surface shows no surface *reconstruction* the surface does have some *relaxation* where the surface atoms have some vertical displacement because of charge transfer between the surface atoms. The transfer of charge is from the cadmium sites toward the tellurium sites such that the cadmium dangling bond is left somewhat more empty and the tellurium dangling bond is somewhat more full. Accompanied with this charge transfer is a shift of the tellurium atom vertical upwards and the cadmium atom vertical downwards. This shift (or buckling) causes a tilt because the bond lengths are nearly invariant and this tilt can be measured using LEED. The tilt (or buckling angle, ω) was found to be $\omega = 30.5 \pm 1.5°$, similar to that found on GaAs and other III-V semiconductors. This is surprising since CdTe is considerably more ionic

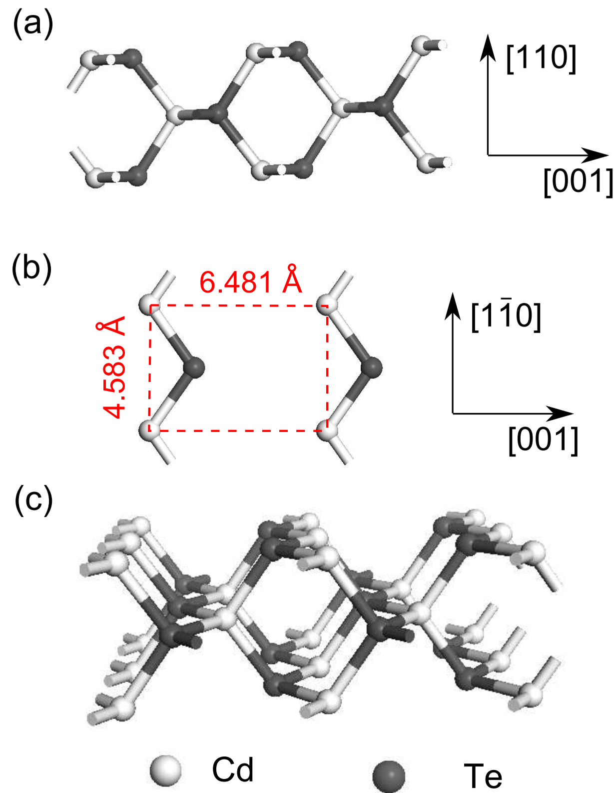

Figure 4.1: Schematic of the CdTe(110) surface. (a) Side view looking along the [1$\bar{1}$0] direction. (b) Top view with the 1×1 unit cell shown by the dashed rectangle. (c) Perspective view looking along the [1$\bar{1}$0] direction.

than those materials [68]. Due to the inherent charge neutrality and therefore lack of surface reconstruction, the (110) surface lends itself to being a *standard* amongst binary semiconductor surfaces. Furthermore, the charge transfer between surface atoms means that any surface states (from dangling bonds on the surface) are pushed outside the band gap region, opening up the way to STM/STS studies of the states in the gap due, e.g., to metal deposition for the study of Fermi-level pinning at metal-semiconductor junctions [69, 70]. Such studies have been very successfully employed on III-V semiconductor (110) surfaces [71].

Going further, tunneling spectroscopy is a very useful tool to study (110) surfaces because of the possibility of performing so-called cross-section STM (XSTM). In XSTM, heterostructures or low dimensional structures can be

probed in cross-section (i.e. perpendicular to the growth plane) by a STM tip scanning across the cleavage plane [72, 73]. This is usually performed by growing heterostructures by e.g. MBE along the [100] direction on a (100) orientated substrate. These are then cleaved (in vacuum) on the (110) plane exposing a clean flat surface with the structures viewed in cross-section. Tunneling spectroscopy is ideal for this since it gives us information about the electronic structure (both bulk and surface) at the very local scale and can even yield specific physical quantities like band offsets or the energy of quantised electronic states. This has been very successfully employed in III-V semiconductors for the study of heterojunctions and quantum dots [74, 75]. As such, STS of the (110) surface of III-V semiconductors has been extensively developed over the last 20 years, and is now a mature science [71, 76]. Unfortunately II-VI semiconductors have not received that kind of attention. Indeed, in this thesis we present the first tunneling spectra obtained on CdTe and CdZnTe surfaces. The aim of this work was to record and analyse tunneling spectra from CdTe and CdZnTe (110) surfaces, upon which future developments in this field can be made (e.g. to study II-VI based heterostructures or quantum dots). To start with, we image and record atomically resolved images of the surface using STM. Then we move on and investigate the electronic structure of the surface using STS. We have performed measurements on both n-type and semi-insulating material, with the latter being particularly relevant since the majority of CdTe and CdZnTe crystals are undoped and have a high resistivity. By using theoretical calculations of the tunneling current and matching the results to experimental data, we are able to fully understand the physical processes involved.

4.2 Sample Preparation

Samples were undoped single crystals of CdTe or CdZnTe which were grown by the MTPVT method as described in Chapter 2. Undoped material was

generally semi-insulating with resistivities greater than 10^8 Ωcm. We have also studied n-type CdTe samples which were produced by post-growth doping of bulk CdTe crystals with chlorine. Chlorine atoms substitute tellurium atoms yielding extra electrons to the lattice [77]. The doping was performed by annealing samples in an atmosphere of chlorine at 450°C. The atmosphere was created from a precursor of zinc chloride [78]. Annealing was typically performed for 48 hours with the heating and cooling rate kept below 2°C/min. The experimental set-up for the post-growth doping process is shown in Figure 4.2. Electrical characterisation of the doped samples was performed using indium metal contacts that were deposited by thermal evaporation [79]. Figure 4.3(a) shows the current-voltage characteristics from a planar n-type doped CdTe device. Here we can see very symmetrical ohmic behaviour from the indium contacts. These electrical characteristics qualitively confirm the doped crystals are n-type since an indium contact on semi-insulating or p-type material would make strong Schottky barrier contacts. Because the diffusion coefficient of chlorine in CdTe is relatively small, it is expected that the dopant only penetrated into the near-surface region. A quick check of this was made by polishing off 30 microns from the surface layer and re-depositing an indium metal contact on to the freshly prepared surface. As expected, the current-voltage curve shows a strong diode or Schottky behaviour, as shown in Figure 4.3(b). This indicates that the dopant did not penetrate further than 30 microns below the surface. This surface doping however, is not critical for STM studies because we are only interested in the near-surface region. An exact measurement of the doping level within the semiconductor was made using the Van der Pauw method using four indium metal contacts at opposite corners of the sample and applying a magnetic field of 0.5 T perpendicular to the (110) plane [80]. Using this we found the doped CdTe crystals had carrier concentrations in the range of $(0.5 - 2.1) \times 10^{16}$ cm^{-3}.

(110) orientated surfaces were prepared by cleaving in air. A diamond scribe was used to scratch a line along a [110] direction across the sample.

Pressure was applied above the scribed line causing the sample to cleave forming a (110) surface. The quality of the cleavage was often mixed with some samples producing mirror like surfaces and others producing highly stepped surfaces. Whenever a poor cleave was achieved the surface was polished and etched to remove any steps on the surface prior to loading into UHV. Samples that cleaved well were immediately loaded into UHV without any further preparation. N-type doped samples were cleaved prior to post-growth doping, however after this process the surface was very lightly polished and etched in bromine methanol to remove the tarnished surface. Following this, ohmic indium metal contacts were deposited by thermal evaporation as described above.

In UHV, clean surfaces were prepared by argon ion sputtering and annealing, as described in Chapter 2. For this surface, we followed the preparation method described by Cohen-Taguri *et al.*[64], which consisted of sputtering at 1 keV for 30 minutes at normal incidence followed by annealing at 180°C for a couple of hours. The lower annealing temperature in this case prevents zinc enrichment at the surface, which would likely alter the surface composition and reconstructions.

4.3 Results

4.3.1 Surface Reconstructions

Figure 4.4 shows a STM image of the CdZnTe(110) surface after sputtering and annealing. This image was recorded using a negative sample bias, and thus represent tunneling from filled states of the sample. The surface appears to be made up of rows separated by terraces. The rows lie along the $[1\bar{1}0]$ directions. Step heights are measured to be about 2.3 Å, corresponding to a single atomic step. The measured periodicity on the surface is found to be the same as for the bulk terminated surface, i.e. the surface has a (1×1) reconstruction. A detailed STM image of the surface showing the (1×1) unit

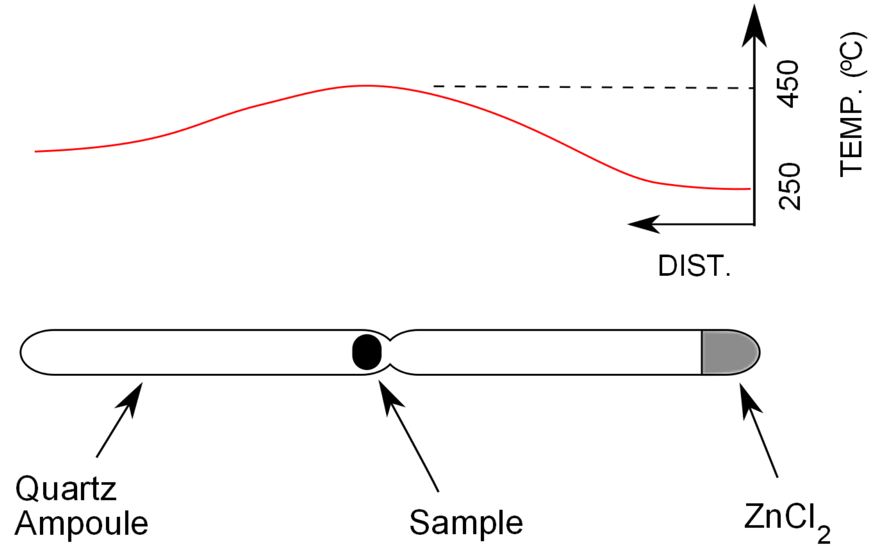

Figure 4.2: Experimental set-up for post-growth doping of CdTe crystals with chlorine. The sample and dopant are enclosed in an evacuated sealed quartz ampoule. The pressure inside the ampoule was 1.4×10^{-4} mbar before sealing. The temperature profile during the annealing process is shown above.

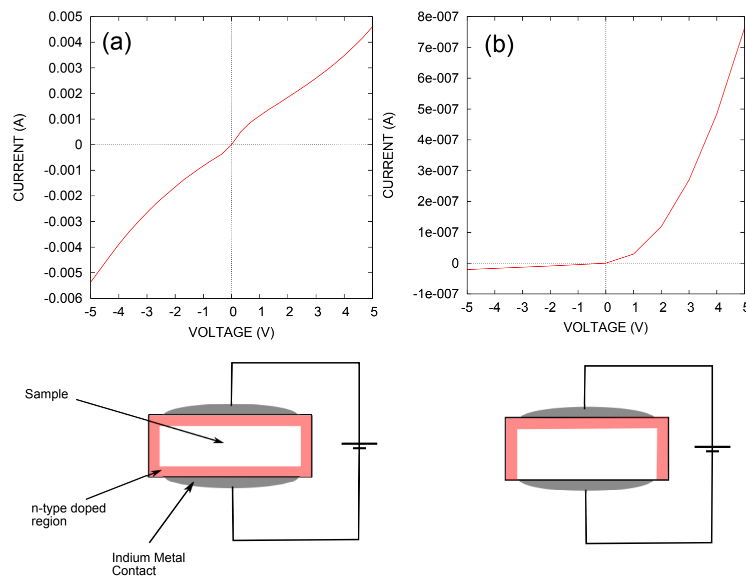

Figure 4.3: Electrical characterisation of n-type CdTe crystals. (a) current voltage characteristics for planar ohmic contacts. (b) current-voltage characteristics with 30 microns removed from one side.

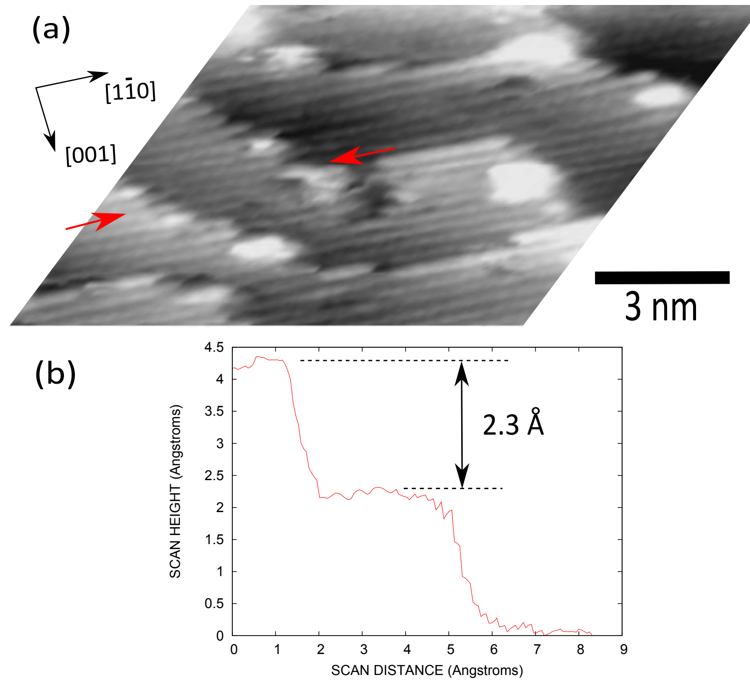

Figure 4.4: (a) STM image of the CdZnTe (110) surface. Sample bias -2 V, tunnel current 0.1 nA. Gray scale range 4.5 Å. (b) Line profile taken between the arrows in (a).

cell is shown in Figure 4.5(a). These results agree with previous work on the (110) surface and also agrees with that of the majority of III-V and II-VI (110) semiconductor surfaces which also show a (1×1) reconstruction [64, 81, 68].

Line profiles taken across the surface show the corrugation amplitude to be about a factor of 2 higher along the [001] direction compared to the [1$\bar{1}$0] direction. This is not surprising since the atomic distance along that direction is much smaller, resulting in a more localised charge density, and as a result the atomically resolved STM image appears as rows. Having said that, STM images of many III-V semiconductor (110) surfaces display a 90° rotation in the apparent row direction at positive bias (i.e. rows align along [100] directions at positive bias). This was attributed to various contributions from intrinsic dangling bond states at the surface at either bias polarity [82]. For this case however, we did *not* observe this effect because STM images could not be obtained at positive bias due to a very low tunneling current. Similar results were recorded from the n-type CdTe(110) surface, except that for this case

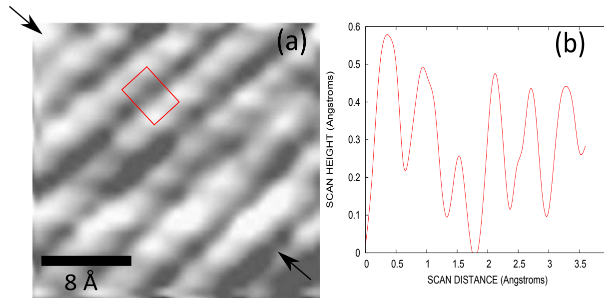

Figure 4.5: (a) Detailed STM image of the CdZnTe(110) surface. A (1×1) surface unit cell is shown by the red rectangle. (b) Line profile taken between the arrows in (a).

the applied bias voltage was of opposite polarity. Again however, we could not obtain a sufficiently stable tunnel current to record good STM images at the opposite bias polarity (although the magnitude of the tunnel current was larger for the n-type case). This apparent *rectification* is explained in the next section by considering the tunneling spectrum obtained from these surfaces.

4.3.2 Tunneling Spectroscopy

In this section we investigate the variation of the tunnel current with applied bias voltage using tunneling spectroscopy. The experimental methods for STS were outlined in Chapter 2.

Figure 4.6 shows a typical tunneling spectrum obtained from the semi-insulating CdZnTe(110) surface. In part (a) the tunneling spectrum is plotted on a linear scale, whereas in part (b) it is plotted on a logarithmic scale. We can see the spectrum is highly rectified in that a large amount of current flows at negative sample bias, but very little flows at positive sample bias. The onset at negative bias is well defined at 0.7 V whereas at positive bias it is not well defined, being at about 1.5 V. No current is observed to flow at very low bias voltages (around zero volts), with the noise level being below 1 pA. The highly rectified spectrum is consistent with that found previously on the SI and weakly doped GaAs(110) surfaces [83, 84].

A tunneling spectrum obtained from an n-type CdTe(110) surface, is shown

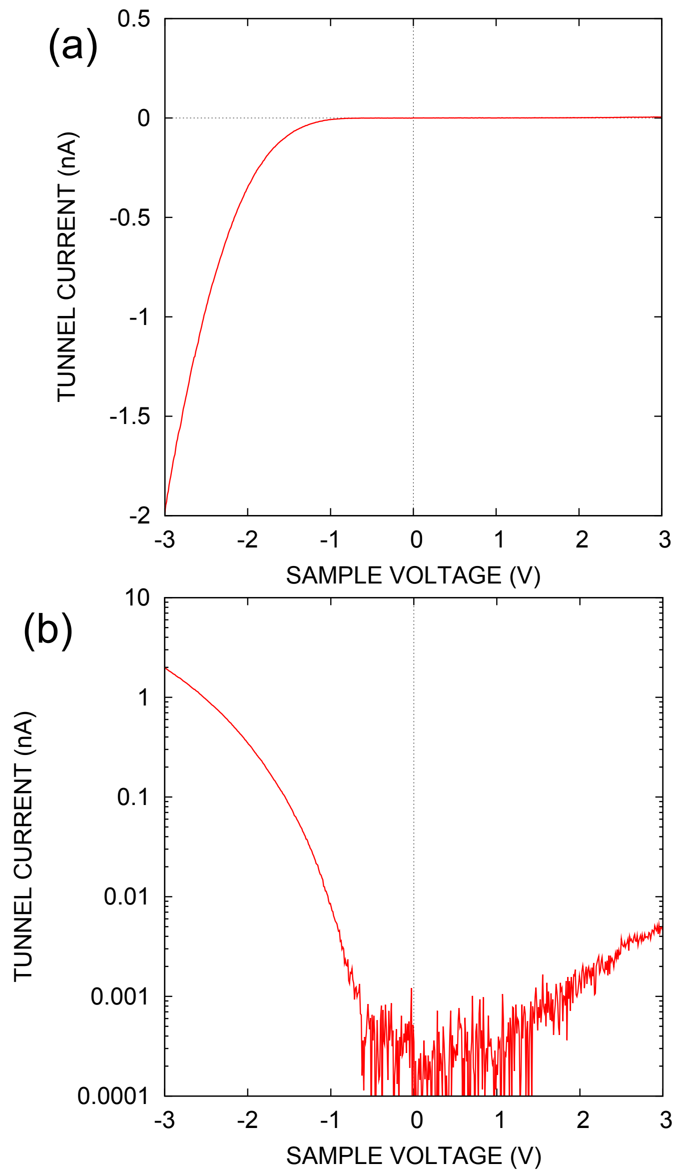

Figure 4.6: Tunneling spectrum obtained from the SI-CdZnTe(110) surface. (a) Linear Scale (b) Logarithmic scale.

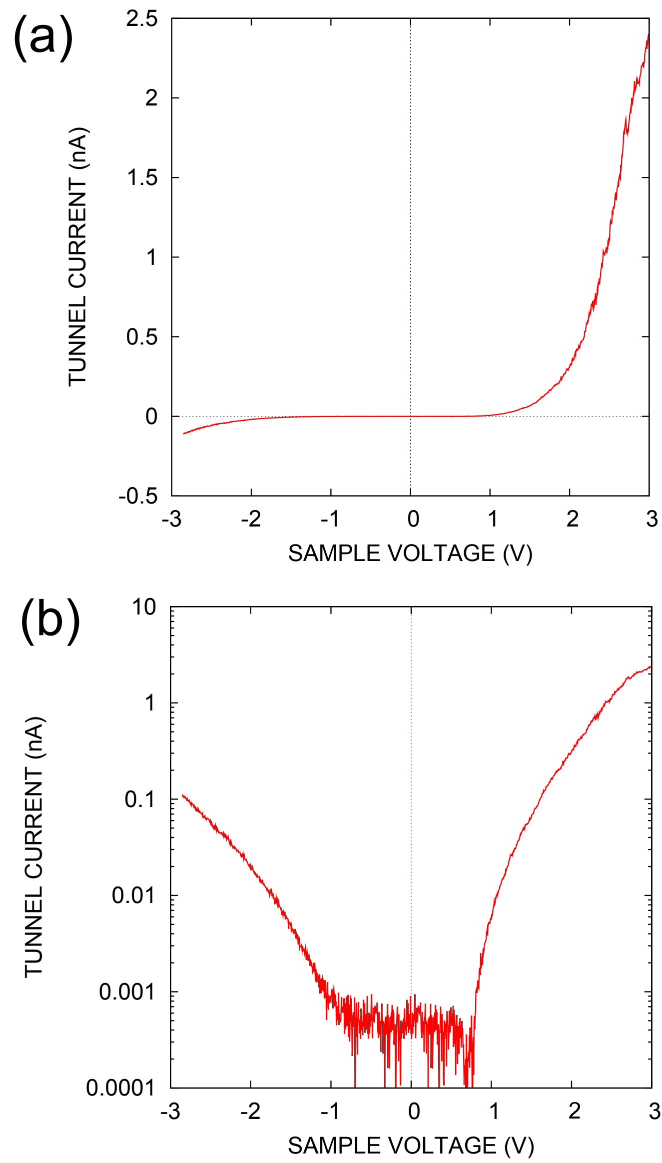

Figure 4.7: Tunneling spectrum obtained on the n-type CdTe(110) surface (a) Linear scale. (b) Logarithmic scale.

in Figure 4.7. Again, the spectrum is plotted in both a linear and logarithmic scale. This spectrum is again quite rectified, but this time more current flows at positive sample bias compared to negative sample bias. The amount of rectification is smaller for the n-type surface, with approximately 10x more current flowing at +3V relative to -3V (this is compared to over 100x for the SI (110) surface). The current onsets are clearly better defined, being -1 V and +0.7 V respectively.

Another more convenient way of viewing tunneling spectra is to calculate the normalised conductance. That is, taking the differential conductance and dividing by the total conductance, $(dI/dV)/(I/V)$. This normalised conductance provides a value that can be presented on a linear, rather than a logarithmic scale and allows us to easily compare spectra taken from different surfaces using different tips. The reason for doing this analysis is that the normalised conductance has been shown to be *independent* of tip-sample separation [71]. Since it is impossible to precisely know the tip-sample separation in a particular measurement, comparing spectra from different experiments becomes difficult. Furthermore, the normalised conductance has also been shown to produce a quantity that is proportional to the surface-state density and has been used in many cases to measure surface electronic structures for both metals and semiconductors. For example, the electronic structure of the pi-bonded Si(111)-(2×1) and Si(111)-(7×7) surface reconstructions have been precisely measured using STS by plotting the normalised conductance [85, 86]. The main limitation in this analysis is that for wide band gap semiconductor surfaces (e.g. GaAs or CdTe), the normalised conductance diverges near to the band edges. This occurs simply because the current approaches zero faster than the differential conductance. To overcome this effect a certain amount of broadening can be applied to the conductance (I/V) by convoluting it with a Gaussian or exponential function. This forms a more smoothly varying function and prevents the divergence problem near to band edges [71, 87]. Another more simply way of doing this is to simply add a small offset to the conduc-

tance preventing the divide by zero problem, $(dI/dV)/[(I/V) + c]$ [88, 89]. We choose the latter method here for simplicity and clarity. In any case, the normalised conductance generally can only be used as a *qualitative* method to analyse experimental data; a more *quantitative* method is to calculate the tunneling current and fit to the experimental data. This analysis will be done later, but first we will examine the normalised conductance spectra obtained on the semi-insulating and n-type (110) surfaces.

Figure 4.8(a) shows the normalised conductance spectra obtained on the semi-insulating (110) surface. The normalisation was performed using an offset constant of 10 pA/V. At negative sample bias, we see a large contribution with a peak at 1.40 V. For the moment let us assign this to the valence band (VB) since it is observed at negative sample bias. The VB onset can be measured by extrapolating a line from the linear portion of the spectrum down to zero (black dashed lines in Figure 4.8), which gives a value of 0.50 V. At positive sample bias, we observe a significantly smaller contribution and this we attribute to the conduction band (CB). This small contribution is in line with the rectification observed in the raw data. Extracting an onset for the CB is more difficult due the noise in the data, however for this spectrum we find a value of 1.0 V. So on the face of it the surface has a band gap of around 1.5 eV, i.e. closely matched to that of CdZnTe. This suggests that TIBB effects are relatively weak which is quite surprising considering the low doping level in this sample. However, taking numerous measurements on a number of different samples we noted that the CB component can vary quite significantly. Indeed for some samples, we observed no tunnel current up to voltages greater than +3 V, giving band gap values much greater than 1.5 eV. As will be discussed later, theoretical calculations of the tunnel current must be employed to gain a better insight into the tunneling processes occurring, since e.g. no physical explanation for the strong rectification observed can be deduced from the normalised tunneling spectra. Now consider the normalised tunneling spectra obtained from n-type CdTe (Figure 4.8(b)). This spectrum was normalised using an offset value of

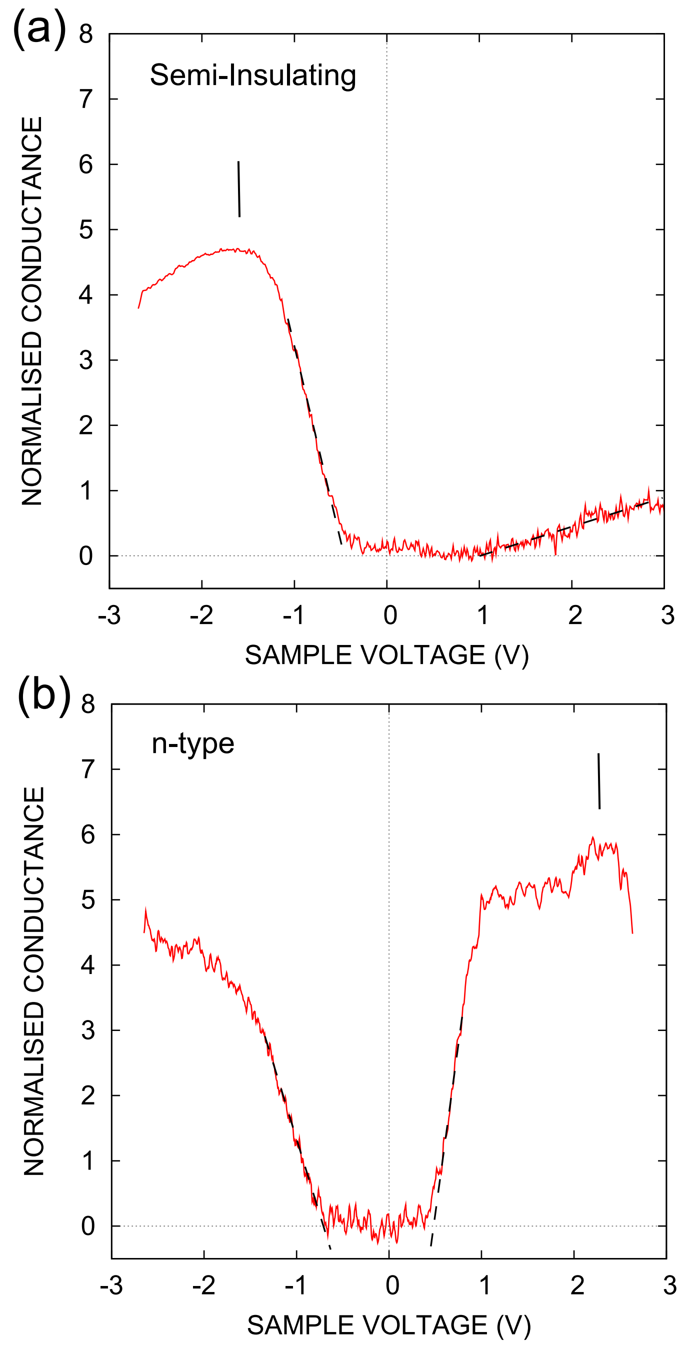

Figure 4.8: Normalised tunneling spectra obtained on semi-insulating (a) and n-type (b) surfaces.

15 pA/V. We can clearly see two components at negative and positive sample bias (VB and CB respectively). The CB and VB onsets are measured in the same way as before, yielding a surface band gap of about 1.15 eV, i.e. much less than bulk band gap of 1.47 eV for CdTe. This implies a mid-gap contribution to the tunnel current from accumulation layer or defect states. A peak is observed at +2.30 V which we tentatively assign to be a surface state from the unoccupied cadmium dangling bonds. Technically this is a surface resonance because it has significant overlap (degeneracy) with the CB. A surface resonance has been observed at 1.5 eV above the CB minimum by photoemission spectroscopy [90]. In this case, we measure the peak to be 1.85 eV above the CB minimum (not taking into account the effects of TIBB). Calculations of the TIBB at these bias voltages (discussed later) gives a value of 0.70 eV, therefore yielding a revised energy for the surface resonance of 1.55 eV above the CBM (calculated using Equation 1.11) i.e. closely matching that found from photoemission. Indeed, the energies of various surface resonances on III-V semiconductor surfaces have been measured in this way [71].

The normalised conductance spectra therefore give a convenient overview of the experimental data, however in order to get a true physical insight into the tunneling processes, we need to be able to calculate the tunneling current taking into account the effects of TIBB. This is the focus of discussion for the next section.

4.3.3 Computation of Tunneling Spectra

Before we can calculate the tunnel current we need to calculate the amount of TIBB. This is performed by solving Poisson's equation both in the vacuum and in the bulk of the semiconductor. To complicate matters, the 3D shape of the tip must be taken into account since a sharp probe tip will drop less of the applied bias into the semiconductor as compared to a blunt tip with a large radius of curvature. The calculation of the 3D electrostatics is approached using a finite element method using a prolate spheroid coordinate system [34].

Electrostatic calculations for the electric potential in a semiconductor near to a biased metallic tip is shown in Figure 4.9. In these calculations we have considered an n-type semiconductor (CdTe) with a dopant concentration of 1×10^{16} cm^{-3}, a contact potential of 0 eV and a tip sample separation of 1 nm. In Figure 4.9(a) the calculation was performed using a tip radius of 70 nm, whereas in Figure 4.9(b) the calculation was performed using a radius of 20 nm. We can clearly see that more of the potential is dropped into the semiconductor for a tip with a larger radius. For this case the semiconductor is in depletion (positive TIBB) and for a larger tip radius more of the semiconductor is depleted of charge.

Other parameters that should be considered when calculating the TIBB, are the tip-sample separation (s) and tip shank angle. For example, if the tip-sample separation is increased, *less* of the electrostatic potential is dropped into the semiconductor. However if tip shank angle is increased then *more* of the applied potential is dropped into the semiconductor. Because of the apparent overlap between these two parameters, and because we do not know the exact shape of the tip at the nanoscale, we chose *not* to vary the tip shank angle within our calculations. Instead, we relied upon using the tip radius and tip-sample separation to control the magnitude of the TIBB. The main advantage of this method is that the number of calculation parameters is reduced, allowing for easier computational fitting.

For most surfaces there usually exist a number of *extrinsic* surface states which can hold significant charge so as to alter the band bending at the surface. These extrinsic states result from structural defects at the surface (e.g. steps, absorbates, grain boundaries, etc...) or from surface disorder. Because these defects are highly disordered and/or originate from a large variety of sources, they are usually considered to be electrically distributed evenly over the band gap region [1]. This surface band is then filled with electrons up to some energy known as the "charge neutrality level". This is the energy below which states are neutral when filled and positively charged when empty, and above

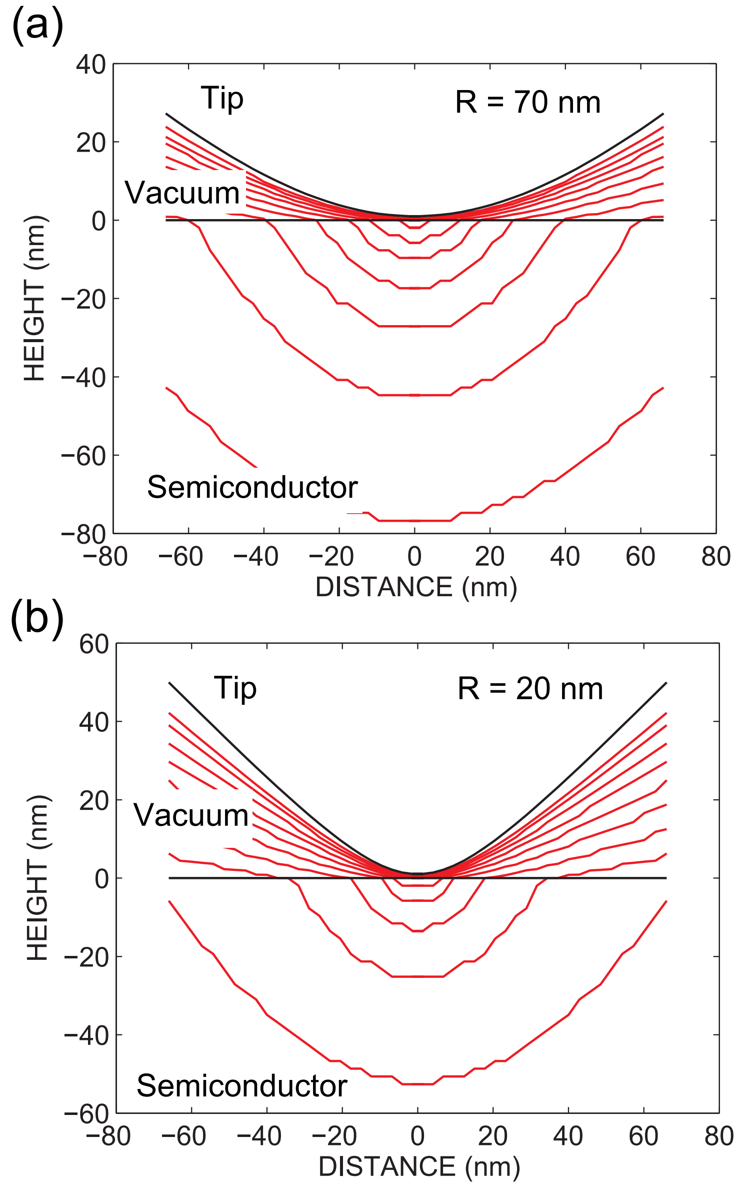

Figure 4.9: Examples of the calculated electrostatic potential distribution from a hyperbolic probe tip near to a n-type semiconductor surface. Computed electrostatic potentials are for a tip of radius of (a) 70 nm and (b) 20 nm, respectively. For both panels the sample is biased at +2 V and the contact potential is 0 eV, therefore the electrostatic potential energy of the tip relative to a point deep inside the semiconductor is +2 eV. Constant potential energy contours (red) are separated by 0.182 eV and the semiconductor doping was set at 1×10^{16} cm^{-3}.

which they are negatively charged when filled and neutral when empty. The former types of states are known, by definition, as donor-like and the latter as acceptor-like. The position of the charge neutrality level, as well as the position of the Fermi level in the bulk of the semiconductor generally controls the surface band bending. If the extrinsic surface states exist in sufficient number, then the Fermi-level is known to be “pinned” at a particular value [91]. For the STM, where an additional electrostatic potential of the probe tip is included, then the TIBB can be significantly altered by the presence of extrinsic surface states.

In addition to extrinsic surface states, we must also consider *intrinsic* surface states. Theses states are intrinsic to the surface, in that they are from the ideal surface reconstruction, and are not resultant from some external effect (e.g. absorbate). For example, intrinsic surface states on the GaAs(110) surface from gallium and arsenic dangling bonds have been shown to hold significant charge so as to pin the Fermi level and lead to a tunnel current within the band gap region (the so-called dopant induced component) [92, 71]. For CdTe(110), two intrinsic surface states (technically surface resonances since they are degenerate with the bulk bands) associated with dangling bonds have been identified: The first is acceptor-like with energy 1.5 eV above the CB minimum and is associated with the cation[90] and the second is donor-like with energy 0.3 eV below the VB maximum and is associated with the anion[93]. Such states will be considered within the theoretical calculations of the tunnel current, using a density of 3.4×10^{14} cm^{-2} i.e. one for every surface atom corresponding to each surface dangling bond.

Having calculated the TIBB at a particular bias voltage (taking into account the effects of various surface states), we can now calculate the tunnel current that flows between the sample and tip. This calculation is performed by analysing the equations presented in Section 1.3 based on the theory developed by Tersoff and Hamann. The amount of tunnel current is evaluated in the limit of large tip radii (i.e. a 1D planar treatment in the z-direction).

This approximation neglects the lateral (radial) part of the wavefunctions. In general the effect of curved potential contours as in Figure 4.9 will lead to a slight focusing of the wavefunction at the surface. However for larger tip radii whereby the equipotential contours are nearly parallel, this effect is expected to be small. For localised states at the surface (i.e. those associated with an accumulation layer), this approximation neglects the effects of any lateral potential confinement (i.e. electrical quantization of states), however they are considered in the z-direction. The advantages of using the planar approximation is that it simplifies the computation massively. Of course, for a particularly sharp tip, less current is likely to flow, as compared to a blunt tip. However, the actual tip shape is not known in an experiment, so a scaling factor (representing a fictitious tip area) is usually included to match to the *magnitude* of the current. This tip area is physically unimportant since it is highly dependent upon other factors such as the tip-sample separation. Typical values for this area are usually in between $0.1 - 1.0\,\text{nm}^2$. Furthermore, the effects of the image potential which (to first approximation) lowers the potential barrier in the vacuum and increases the current density by three orders of magnitude (and does not have any dependence upon tip-sample separation or bias) is taken into account by multiplying the current density by 1000 [34, 94, 95]. As one final point it should be noted that many of the parameters mentioned above correlate with each other such that the overall effect is cancelled. For example, an increase in tip radius increases the TIBB, however this can be compensated by increasing the tip-sample separation, such that the overall change in the tunnel current is negligible.

The whole calculation is performed using the SEMITIP program developed by Prof. R. M. Feenstra from the Physics Department at Carnegie Mellon University, USA [96]. This program implements all of the theoretical considerations described above and the majority of the theory was developed within his research group. Indeed, Prof. Feenstra has been the leading researcher in the field of STM on semiconductor surfaces for the past 25 years.

Band Gap	1.47 eV
Electron Affinity	4.30 eV
Donor Concentration	1×10^{16} cm^{-3}
Donor Binding Energy	0.01 eV
Conduction Band Effective Mass	0.10
Heavy Hole Effective Mass	0.81
Light Hole Effective Mass	0.12

Table 4.1: Main parameters used for the numerical calculations of tunneling spectra for n-type CdTe. Binding energies are relative to the conduction band minimum. Effective masses are relative to the free electron mass.

We are now in a position to compare theoretically calculated tunneling spectra to experimental data. To start, consider tunneling spectra from n-type CdTe(110) surfaces. The main calculation parameters used to calculate the tunneling spectra are listed in Table 4.1. On top of these, we also have to vary the tip radius (R), contact potential ($\Delta\phi$) and tip-sample separation (s). In order to "fit" to the experimental data, we use a simple method whereby we choose appropriate physical parameters for the system (e.g. contact potential, semiconductor properties, tip structure etc...) and observe how well the theory matches to the experimental data. Then a number of parameters are altered, and the change in the fit is observed. This was repeated until a good fit was achieved within sensible parameter limits. This type of "fitting" is of course secondary to perhaps a least squares fit to the experimental data. Indeed, least squares fitting has been performed in the past (e.g. by Dong *et al.* for extracting band offsets in semiconductor heterostructures using STS [74]), however the fitting process takes a considerable amount of time and/or computing power. For the purposes of this study, whereby we only want to gain insight into the tunneling process rather extract physical parameters, then this simple "fitting" (or perhaps better described as "matching") to experiment is completely adequate.

A typical tunneling spectrum obtained on an n-type CdTe(110) surface is shown in Figure 4.10(a). Also shown is the calculated tunneling spectrum using the principle parameters shown in Table 4.1 and using a tip radius of 50

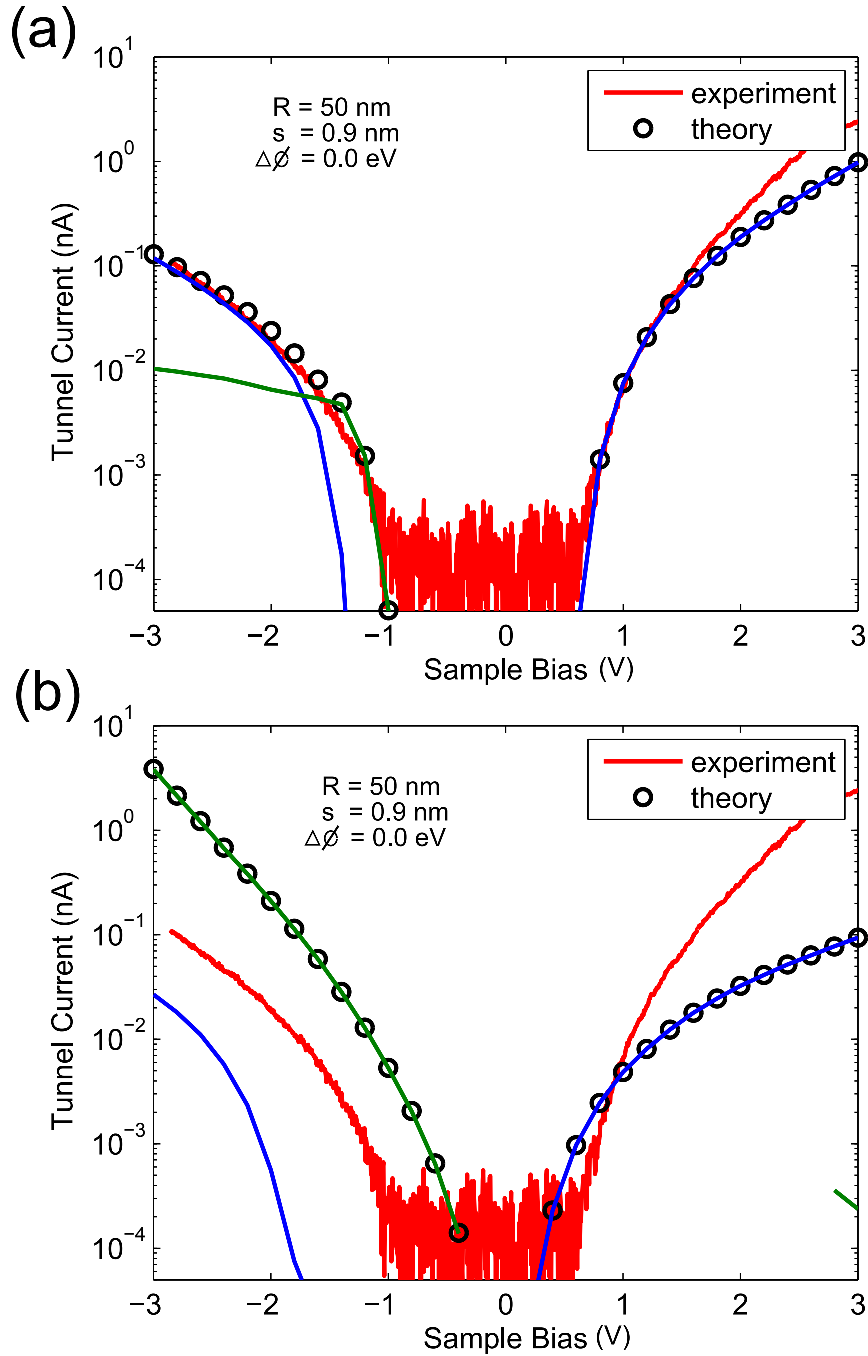

Figure 4.10: Tunneling spectra from n-type CdTe(110) surfaces, experiment and theory. (a) Theory with extrinsic surface states. (b) Theory without extrinsic surface states. Green and blue lines show the contribution from localised and extended states, respectively.

nm and a tip-sample separation of 0.9 nm. For the contact potential we use a value of 0 eV. This was calculated using a metal work function of 4.5 eV, a semiconductor electron affinity of 4.3 eV, and a semiconductor Fermi level of 0.2 eV below the CB minimum. This was calculated using Fermi statistics with a doping concentration of 1×10^{16} cm^{-3} and effective masses presented in Table 4.1. In the tunnel current calculations we have also included a number of extrinsic surface states to model the presence of defects (steps, vacancies, etc...) present in STM images (see Figure 4.4). We have chosen extrinsic surface states that are evenly distributed over the band gap region with a spatial density of 5×10^{13} cm^{-2} (i.e. $\sim$0.1 ML) and charge neutrality level of 0.85 eV (i.e. just slightly above mid-gap). We can see that the theoretical prediction (black open circles) matches the experimental data quite well. The coloured lines show the various contributions from localised (green lines) and extended (blue lines) states. The tunnel current from localised states originates from those states which are in an accumulation layer and are thus localised at the surface. The tunnel current from extended states originates from either the CB or VB and are thus extended throughout the bulk of the semiconductor. These two components are separately calculated within the SEMITIP program and summed together to form the total tunnel current (black open circles). We can see that at large negative bias, the tunnel current originates from electrons tunneling into empty VB (extended) states. At moderate negative bias, there exists a contribution from localised states from an accumulation layer that forms at the surface in the CB. At positive sample bias all the current originates from electrons tunneling from the tip into empty extended CB states. At large positive bias, the theory diverges away from the experimental data. The reason for this is not known at present: we tried to produce a better fit to the experimental data by varying parameters like the tip radius or contact potential, however we could not obtain a better match to the data than that shown. We tentatively suggest that this effect could be due to some voltage variation of the image potential (which is not considered in the calculation),

or perhaps due to an extra contribution from the surface resonance described above.

Calculation of the same spectra but without the presence of extrinsic surface states (Figure 4.10(b)) gives a very poor fit to the experimental data. We have used the same principal parameters as for Figure 4.10(a), but even if we vary some of the parameters we cannot obtain a good fit. This is due the large component from accumulation layer (localised) states in the CB that makes up the current at negative sample bias. There is also a very small component from extended VB states that exist at large negative bias. These extended states make a neglible contribution to the overall spectrum. The large amount of current at negative bias is simply not seen in the experimental data and suggests that the extrinsic states resulting from surface defects play a significant contribution. The effect of the extrinsic states is to become charged, thereby screening more of the electrostatic potential of the tip and reducing the TIBB. We can see this if we plot the calculated TIBB for situations with and without the inclusion of extrinsic surface states, as shown in Figure 4.11. Without the inclusion of surface states, the TIBB is calculated to be very large. We can see a kink in the curve at about -0.2 V. This corresponds the the voltage where an accumulation layer has begun to form in the conduction band. The effect of the accumulation layer is to screen some of the electric field of the tip, thus limiting the TIBB. For the situation when surface states are included, the TIBB is calculated to be quite small and shows only a small variation with bias voltage. Therefore the electronic bands are relatively well pinned by the surface states, and leads to the observed tunneling spectra as shown in Figure 4.10.

Before moving on we should analyse what effect the variation of certain calculation parameters has on the calculated tunneling spectra. For example, can we fit to the data by using wildly different parameters? A demonstration of this analysis is shown in Figure 4.12. In the top graph, a tunneling spectrum obtained from an n-type surface is shown repeated four times with each

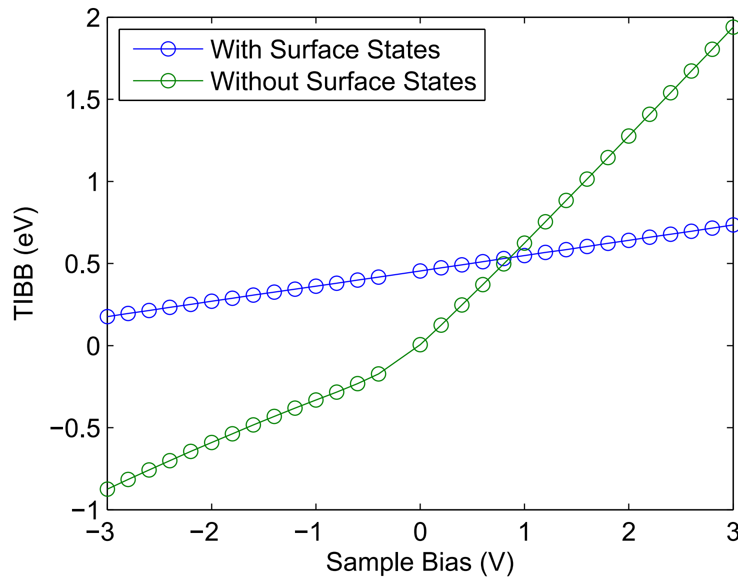

Figure 4.11: Calculated TIBB for tunneling spectra from n-type material with and without extrinsic surface states.

curve compared to a theoretical computation (circles). These data sets are displaced vertically by an order-of-magnitude, for ease of viewing. The theory is computed using various parameter values as indicated. As shown in Figure 4.12(a), a contact potential of 0.0 eV together with a tip radius of 50 nm, at a separation of 0.9 nm, provide a reasonable fit to the experiment. In fact this computation was performed using exactly the same parameters as for Figure 4.10(a). Increasing the contact potential to 0.2 eV produces a decidedly worse fit (Figure 4.12(b)), although by increasing the separation to 1.1 nm (Figure 4.12(c)) or decreasing the radius to 20 nm (Figure 4.12(d)) a reasonably good fit is recovered. It is thus seen that considerable correlation occurs among the parameters of the theory. What is also evident is that reasonable perturbation from the key parameters would not produce a decent fit to the data. For example, computation of a tunneling spectrum using a very large tip radius, e.g. 100 nm (not shown) does not produce a good fit to the present data.

Variation of the parameters used to model extrinsic surface states on the surface has an even stronger effect. As shown in Figure 4.12(e), a surface state density of $\sigma = 5 \times 10^{13}$ cm^{-2}eV^{-1} together with a charge neutrality

level of $E_N = 0.85$ eV provide a reasonable fit to the experiment. In fact this computation was performed using exactly the same parameters as for Figure 4.10(a). Reducing the surface state density to $\sigma = 1 \times 10^{12}$ cm^{-2}eV^{-1} (Figure 4.12(f)) produces a significantly worse fit. A good fit cannot be recovered by altering the charge neutrality level either (Figure 4.12(g) and (h)). Only small variations in the surface charge density (e.g. by fractions of an order-of-magnitude) or charge neutrality level (less than a tenth of an eV) produce reasonable fits to the data.

Consider now tunneling spectra from SI CdZnTe(110) surfaces. In order to calculate tunneling spectra we need to accurately simulate the doping levels for SI material. In our calculations we use a shallow acceptor concentration of 1×10^{15} cm^{-3} with ionization energy 0.01 eV and a compensating deep donor level of concentration 1×10^{16} cm^{-3} of ionization energy 0.74 eV. This shallow level - deep level compensation mechanism is widely accepted as the physically correct mechanism leading to the high resistivities found in SI-materials [97]. The shallow level represents residual impurities at the purification limit obtained during crystal growth or native point defects such as vacancies or antisites. The compensating deep level allows the material to become highly resistive, which would otherwise not occur because of residual impurities that cannot be removed. For example, in SI-GaAs the native deep level EL2 center compensates for residual impurities, most notably carbon [97]. In CdZnTe, due to the high cadmium partial pressure and thus growth in a tellurium rich environment, it has been proposed that the tellurium antisite compensates cadmium vacancies which would otherwise make the material low resistivity and p-type [98, 99, 100, 101]. In this analysis, we do not concern ourselves too much with the actual compensating defects since the tunneling spectra are more dependent on the position of the Fermi-level within the bulk, rather than the relative concentrations and energy levels of the dopants.

Using Fermi statistics we calculate the Fermi-level to be 0.78 eV above the VB maximum, yielding a contact potential of -0.55 eV. Based on charge con-

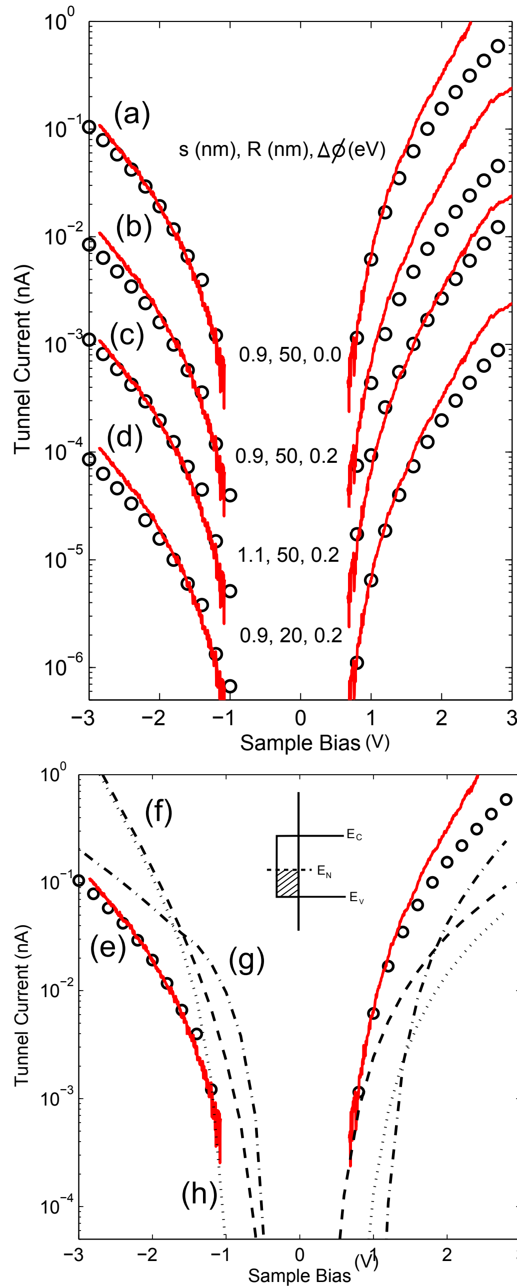

Figure 4.12: Variation of theoretical tunneling spectra using different calculation parameters. (TOP graph) Tunneling spectrum (red lines) obtained from an n-type surface, repeated four times with each curve compared to a theoretical computation. Consecutive pairs of experimental and theoretical curves are displaced by an order-of-magnitude, for ease of viewing. The theory is computed using various parameter values as indicated: tip-sample separation s, tip radius-of-curvature R, and contact potential $\Delta\phi$. (BOTTOM graph) Computations of tunneling spectra for various values of extrinsic surface state density σ, and charge neutrality level E_N. (e) $\sigma = 5{\times}10^{13}$ cm^{-2}eV^{-1}, $E_N = 0.85$ eV (f) $\sigma = 1{\times}10^{12}$ cm^{-2}eV^{-1}, $E_N = 0.85$ eV (g) $\sigma = 5{\times}10^{13}$ cm^{-2}eV^{-1}, $E_N = 0.30$ eV (h) $\sigma = 5 \times 10^{13}$ cm^{-2}eV^{-1}, $E_N = 0.30$ eV.

Band Gap	1.54 eV
Electron Affinity	4.30 eV
Donor Concentration	1×10^{16} cm^{-3}
Acceptor Concentration	1×10^{15} cm^{-3}
Donor Binding Energy	0.80 eV
Acceptor Binding Energy	0.01 eV

Table 4.2: Main parameters used for the numerical calculations of tunneling spectra from SI CdZnTe. Binding energies are relative to the valence band maximum.

centrations within the bulk and using an electron mobility of 1000 cm^{2}V^{-1}s^{-1} and hole mobility of 100 cm^{2}V^{-1}s^{-1} we calculate the bulk resistivity to be 4×10^9 Ωcm, consistent with experiment. The main calculation parameters (in addition to the effective mass parameters cited in Table 4.1) used to calculate tunneling spectra on SI CdZnTe are summarised in Table 4.2.

A typical tunneling spectrum taken from the CdZnTe(110) surface is shown in Figure 4.13. Also shown is the calculated tunnel current using the parameter values of 0.7 nm, 70 nm, and -0.55 eV for s, R and $\Delta\phi$, respectively. The theory provides a good fit to the data over the whole bias range. The calculations show that at positive bias the current originates from tunneling into empty extended states (blue line) of the CB. At negative bias the majority of the current arises from tunneling out of filled CB states due to the occupation of an accumulation layer at the surface (green line). There is also a small component from the occupied valence band states which turns on at -2.0 V (blue line), however this component is two orders of magnitude smaller than that of the localised accumulation layer and plays a neglible contribution to the overall tunnel current (open circles). As a result no voltage dependent imaging can be performed since the tunnel current originates from the CB (either extended or localised) at both bias polarities.

We have also tried to fit to the experimental data when considering the effects of extrinsic surface states, in a similar way as for n-type surfaces. We considered the same density and charging character as for the n-type case. The calculated tunneling spectra when considering extrinsic surface states is

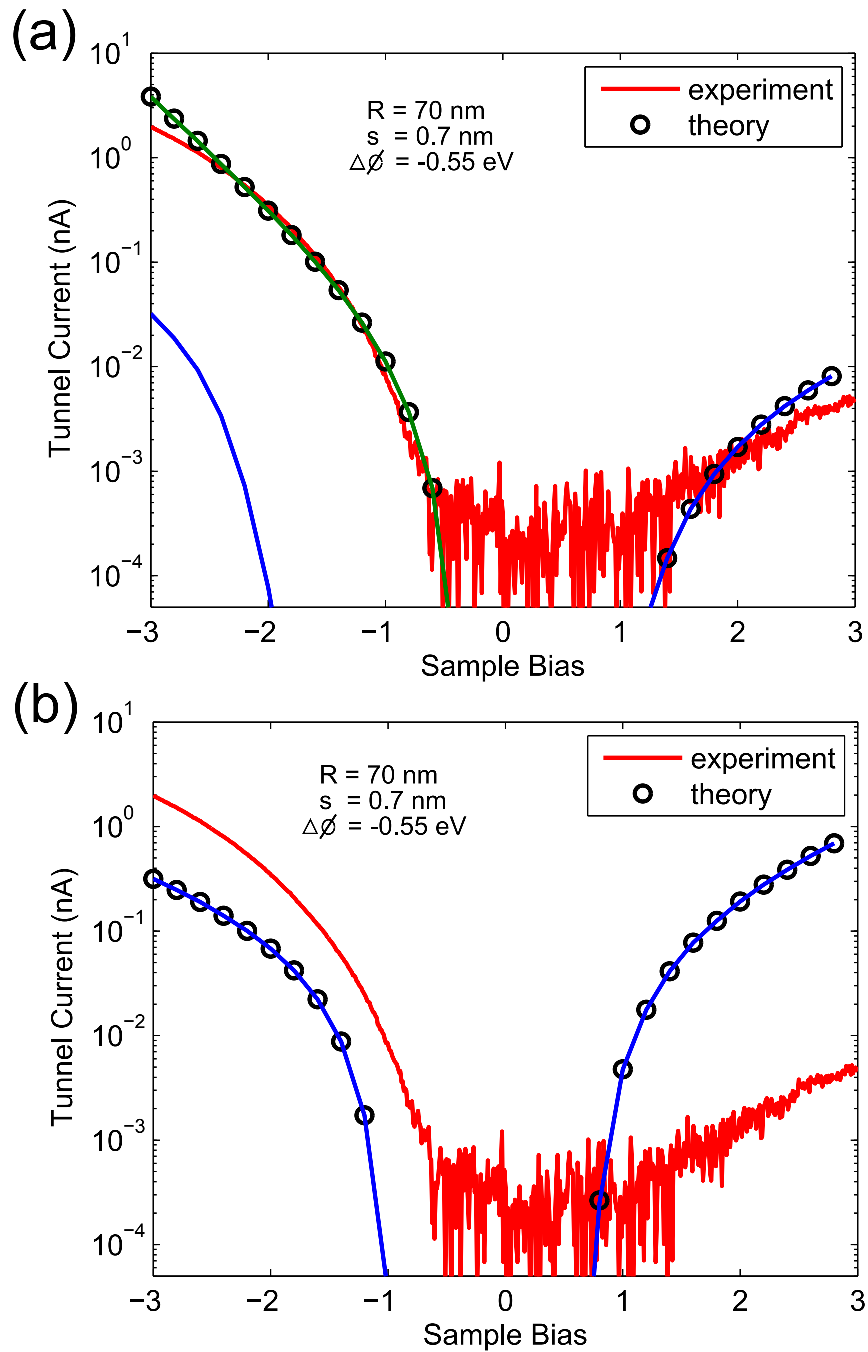

Figure 4.13: Tunneling spectra from the CdZnTe(110) surface, experiment and theory. (a) Theory without extrinsic surface states. (b) Theory with extrinsic surface states. Green and blue lines show the contribution from localised and extended states, respectively.

shown in Figure 4.13(b). We can see that the spectra do not match to the experimental data very well and that no rectification is predicted. The Fermi-level is pinned to approximately mid-gap, since the CB and VB components are roughly evenly distributed either side of 0 V. At both bias polarities the tunnel current originates from extended states, either filled VB or empty CB states. The poor fitting to the experimental data when including extrinsic states suggests that they play lesser role in controlling the tunneling spectra on SI surfaces.

Shown in Figure 4.14 is the voltage variation of the TIBB with and without extrinsic states. For the situation without extrinsic states where tunneling spectra nicely match the experimental data, we can see there is a large amount of TIBB and that it shows a strong voltage dependence. At positive bias the TIBB rises linearly with voltage with magnitude of 1.9 eV at +3 V. At negative bias there is a kink at about -0.7 V owing to the accumulation of charge at the surface screening the electric field of the tip and limiting the magnitude of the TIBB. The large magnitude of TIBB at positive sample bias, explains why the tunneling spectra are so rectified: Usually the tunnel current scales exponentially with voltage, however if there is a large amount of TIBB, then the tunnel current is severely restricted because the difference in energy between the metal Fermi-level and CB minimum is small. For the case when extrinsic states are included, the TIBB is relatively small and is limited to values between -0.45 eV and 0.2 eV over the whole voltage range. The band bending is weak because of the added screening effects from fixed charge carriers at the surface. For this case, the theory does not match the experiment very well.

As one final point, the calculations presented here for both n-type and SI material were performed such that holes were *not* allowed to occupy the VB at the surface. If this effect is incorporated (commonly known as “inversion”) the fitting is decidedly worse. Even with adjustment of the key fitting parameters, matching between experiment and theory was still very poor. Indeed, this

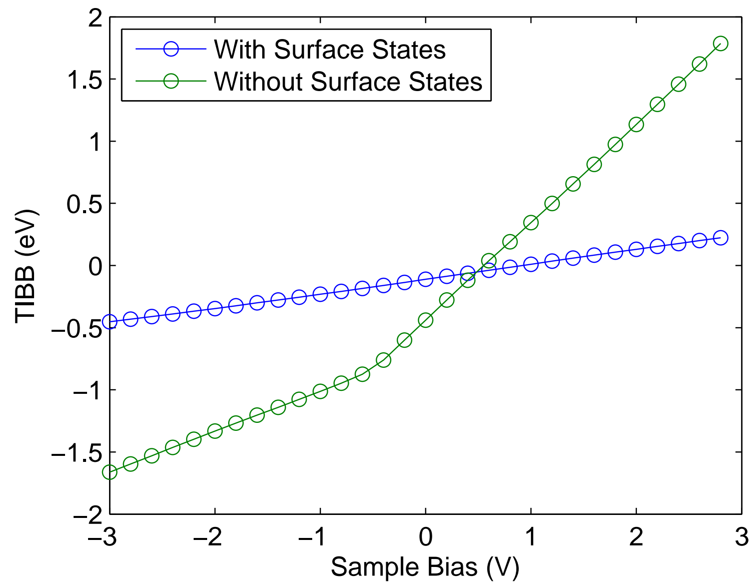

Figure 4.14: Calculated TIBB for tunneling spectra from SI material with and without extrinsic surface states.

phenomenon has been observed on many other semiconductor surfaces and has been attributed to non-equilibrium of charge carriers at the semiconductor surface [102, 103]. These results seem to support this hypothesis, hence the reason for not including the inversion effect in the calculations. The effects of including inversion within the calculations is described in more detail in Reference [104], but are not discussed any further here.

4.4 Discussion

The differences in the lineshape of the tunneling spectra from SI and n-tpye material is very apparent. Calculations of the tunnel current and fitting to the experimental data has revealed the origin of the tunnel current for both conductivity types. The most striking difference between the two is the apparent variation with the effect of extrinsic surface states: spectra from n-type material are strongly controlled by extrinsic surface states, whereas spectra from SI material seems to show little dependence. This is a strange effect, since it is unlikely that the bulk Fermi level position should control the charging character

of surface states. One possible explanation is that of transport limitations to and from those surface states [105]. If current is transported away from those states faster than it can be replenished, then charging of those states would be limited. Indeed, tunneling spectra of UHV-prepared SiC(0001)$-\sqrt{3}\times\sqrt{3}R30°$ surfaces by Ramachandran *et al.* revealed a strong dependence on the magnitude of the current, interpreted in terms of a "spreading resistance" in the transport of carriers to (or from) surface states [106, 102]. The spreading resistance is characterised by $R_s \sim \rho \frac{l}{s}$, where ρ is the semiconductor resistivity, and l and s are the effective length and section of field lines spreading away from the region directly below the tip apex (i.e. the curvature of the equipotential lines shown in Figure 4.9) [107]. In this case, a spreading resistance mechanism is therefore more likely for SI material (large ρ), and less likely for n-type material (small ρ), hence explaining the apparent differences between the two. In any case, a significant increase in the surface state density (i.e. for surfaces that *have not* been prepared in UHV conditions) quite effectively pins the Fermi-level for both n-type and SI material. Examples of such effects will be presented later in the thesis (Chapter 6).

Surfaces that have very few structural defects, e.g. ones prepared by cleavage in UHV, will of course have tunneling spectra that are less controlled by extrinsic surface states. In this case, the tunneling spectra will be more sensitive to bulk effects, e.g. positions of band edges for the study of band offsets in heterostructures. Indeed, this was one of the reason for investigating STS on (110) surfaces. It appears that in order to be able to study such structures, UHV cleavage will be necessary, particularly for low resistivity material. This is perhaps an area for future study, however the tunneling spectra presented in this chapter have provided a strong base and good physical understanding of the specific processes involved.

Now lets move on and discuss intrinsic surface states. These states were included within our calculations since it was important to closely represent the true physical situation. However, if these states are omitted from the

calculations, we observed no change in the lineshape of the calculated tunneling spectra. This suggests that intrinsic surface states play no role in pinning the Fermi-level for n-type or SI material. We can explain the reason for this if we consider where the Fermi-level is during a voltage ramp. For both n-type (Fermi-level close to VB) and SI (Fermi-level near mid-gap) materials, the Fermi-level never gets near to the intrinsic states thus preventing any fixed charge from entering those states. However we would expect there to be some Fermi-level pinning for p-type material because the anion resonance is relatively close to the VB maximum. This is another area for future study, since we have not considered p-type material in the present analysis.

Finally, lets discuss scanning tunneling microscopy on SI materials. Intuitively, imaging should prove difficult since there are very few charge carriers to provide a tunnel current. Indeed, previous experiments have often been performed either at high temperature or under illumination to increase carrier density [108, 109, 64]. In this chapter we have shown that such external effects are not required and topography and spectra can both be obtained in the dark at room temperature. We note that as long as the absolute resistance through the sample is much less than the vacuum gap resistance (typically 20 GΩ) then the majority of the voltage drop falls across the vacuum gap (excluding the electrostatic effects of the tip), thus allowing STM and STS to be performed. In addition to this, sufficient tunnel current should be allowed to flow, this is achieved by using thin samples or by reducing the distance between the probe tip and the electrical contact. However, we note that for some situations (e.g. when performing high resolution imaging or for surfaces that have a very high defect density), the use of an external light source or higher temperatures can greatly improve imaging performance [110]. The choice of using light or higher temperatures, will of course depend on the equipment available to the experimenter. However, it should be remembered that an external light source will alter the surface band bending and therefore significantly change the tunneling spectra [110].

4.5 Conclusions

In this Chapter we have studied the surface reconstructions and analysed tunneling spectra for the (110) surface of CdTe and CdZnTe surfaces. We have considered both n-type and semi-insulating material. The surface shows a (1×1) reconstruction, which appears as rows aligned along the $[1\bar{1}0]$ direction. In these images we observed a large number of surface steps, leading to a high level of extrinsic surface states. The tunneling spectra presented in this chapter have allowed us to investigate the electronic properties for the (110) surface. The (110) surface is ideal for this since there are no intrinsic electronic states that exist in the band gap region. For semi-insulating material, tunneling spectra were found to be highly rectified, with a large amount of current flowing at negative sample bias, but very little at positive bias. Theoretical calculations of the tunneling current based on the Bardeen formalism taking into account the 3D effects of TIBB have shown that an accumulation layer forms at the surface at negative bias, yielding a large tunnel current. At positive bias, the large amount of TIBB (due to the low doping level), means that the electronic bands are significantly bent upwards suppressing the tunnel current. This implies that the tunnel current originates from the CB (either filled or empty) at both bias polarities and suggests that the VB states cannot be probed. This analysis also explains why all of the (undoped) samples studied in this thesis could only be imaged at negative sample bias. For n-type material, we observed both VB and CB states, as well as a small contribution from accumulated charge in the CB. In this case, extrinsic (defect) surface states were found to significantly limit the tunnel current at negative bias. This effect was not observed in spectra from SI material, and a mechanism whereby a spreading resistance near the surface limits the charging of extrinsic states has been suggested to explain this.

Chapter 5

The (111) Surface

5.1 Introduction

In this chapter we look at the atomic structure of clean {111} oriented CdTe surfaces. The {111} crystal surfaces of zincblende structures exhibit crystallographic polarity, that is the (111) and $(\bar{1}\bar{1}\bar{1})$ planes are non-equivalent, as shown in Figure 5.1. Conventionally the close packed plane terminated by metal atoms (cadmium) is called the (111) or A face whereas that terminated by non-metal atoms (tellurium) is called the $(\bar{1}\bar{1}\bar{1})$ or B face. As a result many properties of polar {111} surfaces in CdTe differ considerably. For example, differences in the growth rate and quality of epitaxial films, as well as etch pit geometries are apparent [111, 112, 113]. On the atomic level, as was found using electron diffraction techniques, the surface reconstructions of the polar faces are also remarkably different. For the A face, a (2×2) reconstruction has previously been measured by LEED, although the exact surface structure was not identified in that case [114, 115]. For the B face, a number of reconstructions were identified on MBE grown material using RHEED [116, 117]. At temperatures lower than 300°C, a $c(8 \times 4)$ reconstruction was found. This was observed to have glide planes in the <211> directions and it was proposed that it consisted of an infinite chain structure consisting of tellurium adatoms sitting on a cadmium trimer base in a two layer structure. For temperatures

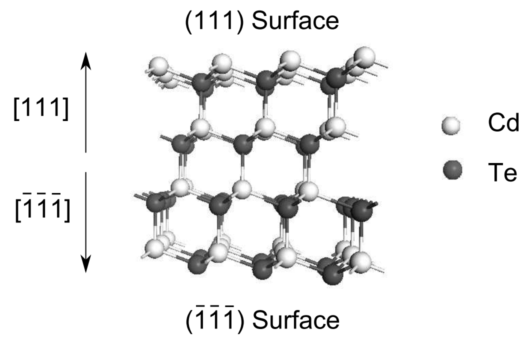

Figure 5.1: Crystal structure for the polar CdTe(111) and CdTe($\bar{1}\bar{1}\bar{1}$) surfaces.

above 300°C, a $(2\sqrt{3} \times 2\sqrt{3})$R30° was observed which was proposed to form from a breaking up of the aforementioned chains, whilst still maintaining the electron counting rule. Although two separate reconstructions were identified, a considerable amount of overlap in the temperature phase diagram was observed, perhaps alluding to the large surface disorder.

In this chapter, we have used scanning tunneling microscopy to study the surface morphology and surface reconstructions of clean CdTe(111)A and B faces that have been prepared in ultrahigh vacuum by argon ion sputtering and annealing. The aim was to build upon the work of those structures identified using electron diffraction techniques.

5.2 Sample Preparation

(111)A and (111)B surfaces were prepared by epitaxial growth of thick undoped CdTe films on GaAs(111)A and B substrates, respectively. Growth was performed from the vapour phase: 'A' films were grown by HWE [48] whilst 'B' films grown by epitaxial CSS [47]. Both types of film were of high crystalline quality with as grown thicknesses of about $\sim 80\mu m$ for 'A' films and $\sim 100\mu m$ for 'B' films. X-ray Laue back reflection diffraction patterns produced well defined spot patterns with a trigonal symmetry for both films (Figure 5.2). Even though the diffraction patterns clearly show the surfaces to be well orientated

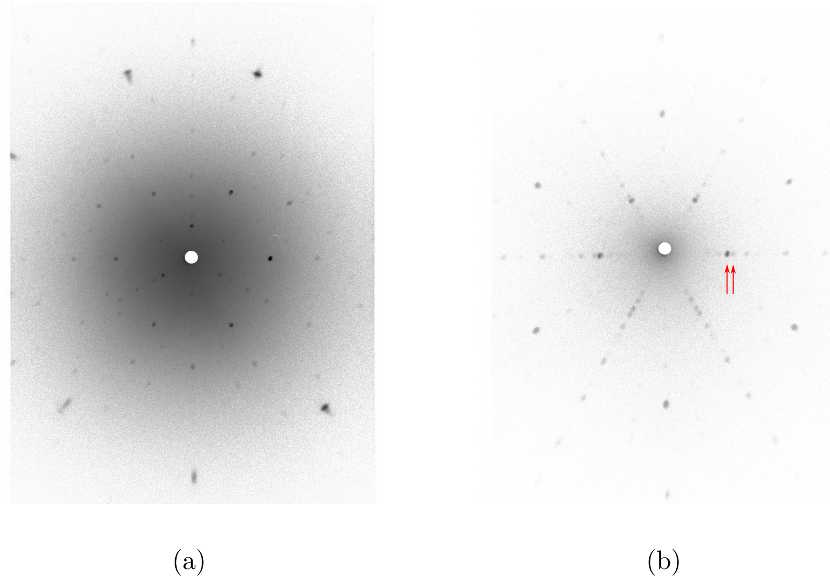

(a) (b)

Figure 5.2: Laue back reflection x-ray diffraction patterns for (111)A (a) and (111)B (b) films.

with a (111) surface plane, there are some striking differences between the two. Firstly, the background intensity for the 'A' film is larger than that for the 'B' film. This represents the better crystalline quality of 'B' film compared to 'A' films. Secondly, the 'B' film shows some double spots (e.g. as shown by the arrows in Figure 5.2(b)) which represent twinning within the crystal. This will become important later when analysing STM images of the surface.

The surface polarity of the films was confirmed using wet chemical etching in a 1:1:1 ratio of HF : HNO_3 : CH_3COOH. This produced a dark black film on the cadmium terminated surface and a shiny polished surface for the tellurium terminated face. Looking under an optical microscope, the A face was found to be considerably etched with a high number of etch pits on the surface (Figure 5.3(a)); whilst the B face was found to be much smoother with a lot fewer etch pits (Figure 5.3(b)). The etching mechanism is still not clear at present, however the polarity of the surfaces have been clearly identified, qualitatively agreeing with previous studies on polarity identification [118]. These results highlight the striking difference in the surface chemistry of the polar {111} surfaces.

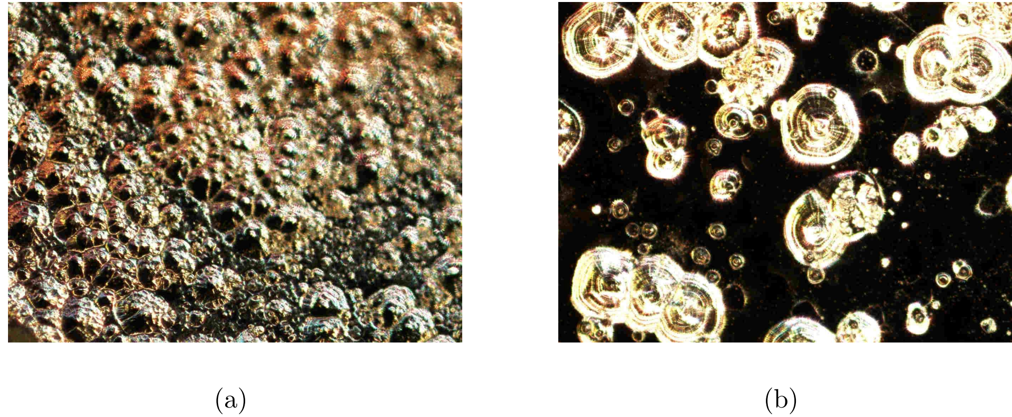

(a) (b)

Figure 5.3: Optical micrographs (200x) of CdTe surfaces after etching in a 1:1:1 ratio of HF:HNO_3:Acetic Acid for 20 seconds. (a) (111)A surface, (b) (111)B surface.

After growth, pieces were cut to size and polished using a diamond suspension with a particle size of 0.1 μm. These were then etched in a 2 % bromine methanol solution for 2 minutes, before being rinsed and dried with compressed nitrogen. Samples were then loaded into vacuum and baked at 65°C for 2 hours to remove any residual methanol. In vacuum, clean surfaces were prepared using argon ion sputtering and annealing. Sputtering was performed as described in Section 2.4. Annealing was performed at various temperatures in the range of 200°C to 375°C for varying times, typically 1-2 hours. Samples were allowed to cool to room temperature before being studied by STM.

5.3 Results

5.3.1 CdTe(111)A Surface

Figure 5.4(a) shows a large area STM image of the CdTe(111)A surface after argon ion sputtering and annealing at 250°C. The surface shows a terraced structure, with four individual terraces observed in this image. The terraces extend typically about 15 nm in the $[\bar{1}\bar{1}2]$ direction and extend much further in the orthogonal $[1\bar{1}0]$ direction. This is a result of the grazing incidence

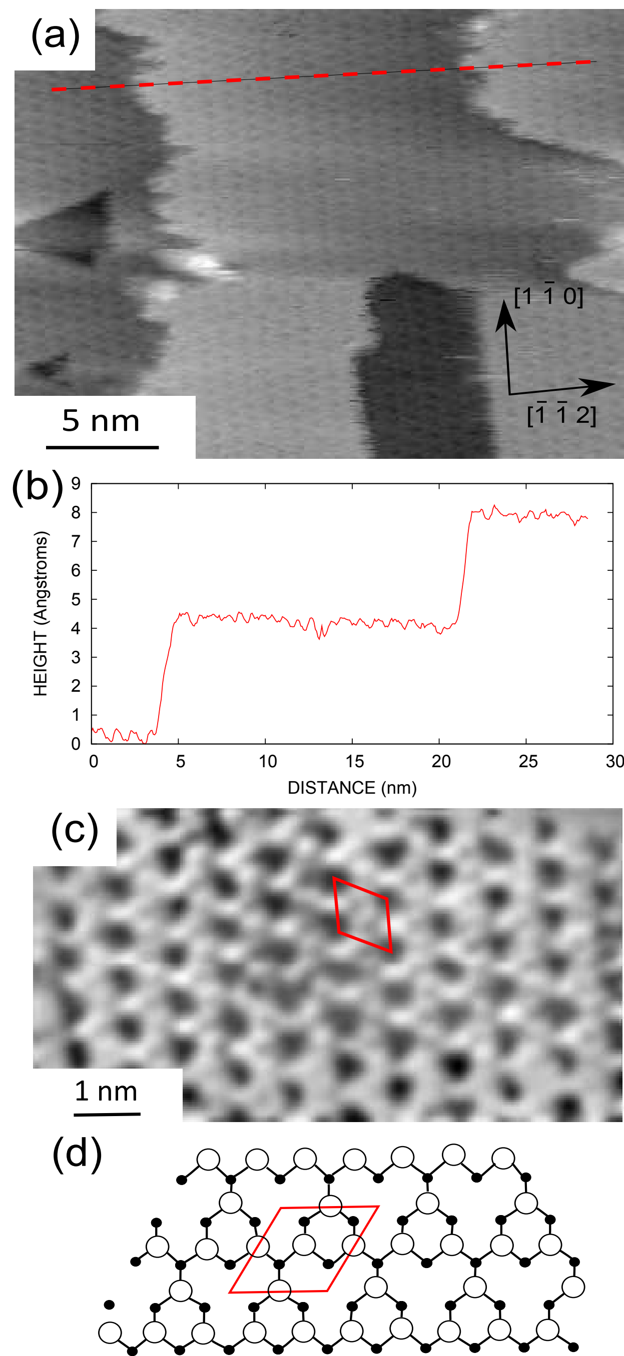

Figure 5.4: (a) Large area STM image of the CdTe(111)A surface after argon ion sputtering and annealing. The image is displayed on a grayscale range of 13.6 Å and was taken using a sample bias of -2 V and a tunnel current of 0.2 nA. (b) Line profile along the dashed line in (a). (c) High resolution STM image detailing the (2×2) reconstruction. Grayscale range 0.77 Å, sample bias -2 V, tunnel current 0.2 nA. (d) Proposed cadmium vacancy model for the (2×2) reconstruction. Large open circles and small filled circles denote top layer Cd and second layer Te atoms, respectively.

sputtering which forms a rippled surface structure perpendicular to the ion beam. It is a coincidence that the beam direction lies along the $[1\bar{1}0]$ direction and thus the extended terrace size in that direction is not a crystallographic effect. Generally, the surface becomes smoother with increasing annealing temperature and/or time. A line profile taken perpendicular to the step edges [Figure 5.4(b)] shows steps to be 3.7 Å in height. This corresponds to one CdTe bilayer in the [111] direction and therefore the steps are mono-atomic.

Figure 5.4(c) shows a high resolution STM image detailing the surface reconstruction. We observe a (2×2) reconstruction with the periodicity along the <110> directions being about 9 Å. This is characterized by the rhombus with a 9 Å side length joining adjacent surface depressions. These surface depression correspond to a cadmium vacancy on the bulk terminated surface. The surface reconstruction shows good long range order and extends over many hundreds of nanometers, albeit separated into terraces. These results agree well with those previously obtained on the CdTe(111)A surface using LEED.

The bulk terminated (111)A surface is terminated with cadmium atoms each having one dangling bond perpendicular to the surface. These dangling bonds are sp^3 hybridized (i.e. the same as in the bulk) and are only half filled with 1/2 electron in each. Therefore the surface does not fulfill the electron counting rule [66]. The removal of 1/4 of the surface cadmium atoms leaves three cadmium dangling bonds per (2×2) unit cell. The missing cadmium atom also leaves behind 3 tellurium dangling bonds per unit cell from the second layer tellurium atoms. Thus there are 3 dangling bonds on both cadmium and tellurium atoms, and the electrons can be equally shared between them such that the more electronegative tellurium atoms have dangling bonds that are completely filled whilst the less electronegative cadmium atoms has completely empty dangling bonds. This is the cadmium vacancy model, and the charge transfer between the atoms means that there is a surface relaxation or buckling: Cadmium atoms relax downwards into the plane of the second layer tellurium atoms; whilst tellurium atoms relax inwards in the plane of the surface. The

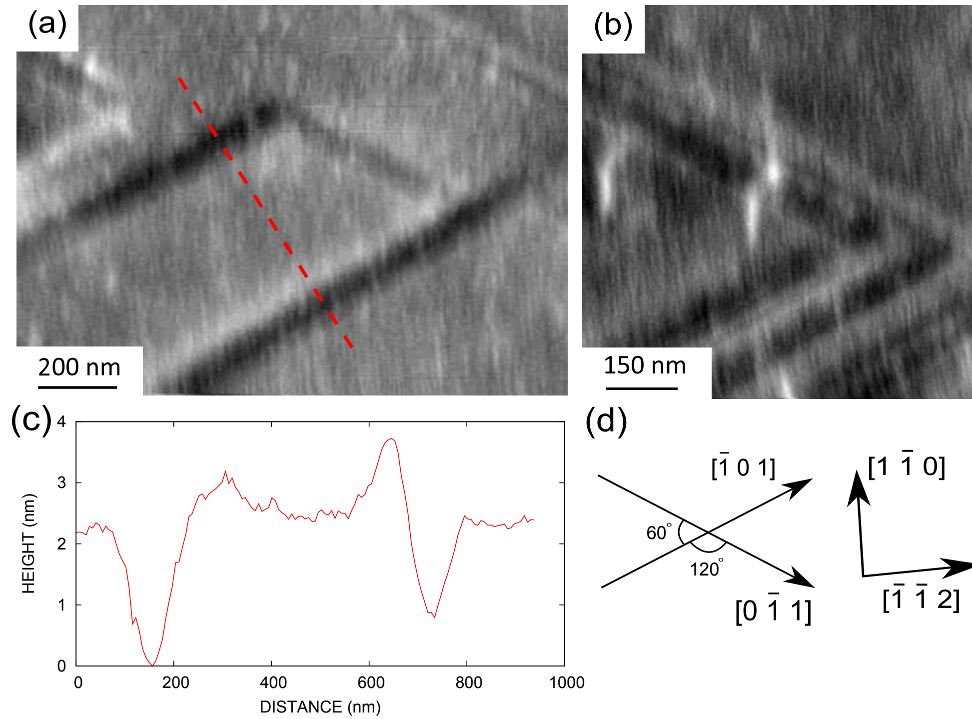

Figure 5.5: Faceting on the CdTe(111)A surface. (a) and (b) Large area STM images taken at two different positions using two different tips. Images were recorded at a sample bias of -3 V and a tunnel current of 0.2 nA. Grayscale ranges are 6.5 nm and 6.4 nm respectively. (c) Line profile taken across the dashed line in (a). (d) Principal crystallographic directions for the sample surface.

proposed cadmium vacancy model is shown in Figure 5.4(d). This buckling vacancy model is analogous to the GaAs(111)A-(2×2) surface reconstruction where the gallium vacancy structure was found to be energetically favorable [119, 120].

In addition to the $(2{\times}2)$ reconstruction we also observed a certain amount of faceting, as shown in Figure 5.5. Figure 5.5(a) and (b) show large area STM images of the CdTe(111)A surface taken at two separate positions using two different tips. We observe elongated features that extend over several hundreds of nanometers and are aligned along the <110> directions with both 60° and 120° angled corners. The facets are sometimes bunched together, as shown in Figure 5.5(b), whereby the distance between two adjacent facets is typically less than 50 nm. The lateral extent of the facets (i.e. the distance

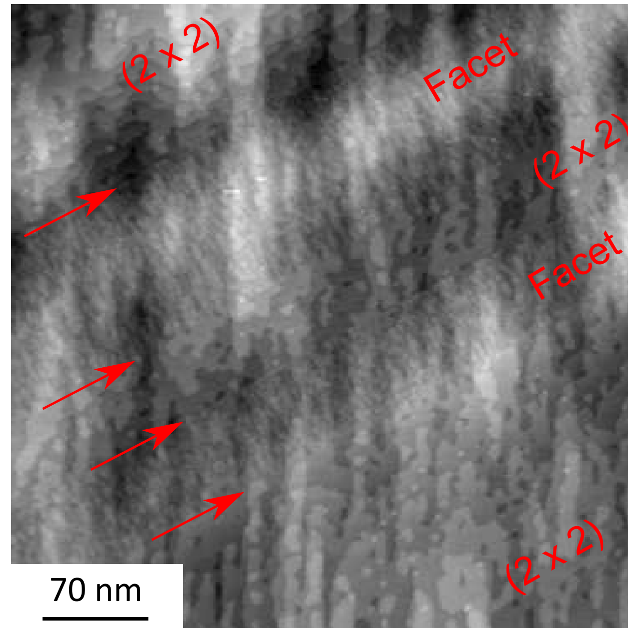

Figure 5.6: Detailed STM image of two facets intersecting (2×2) terraces. Arrows show the facet boundaries. Sample bias: -3 V. Tunnel current: 0.2 nA. Grayscale range: 3.8 nm.

along a <211> direction) is usually quite small, typically about 50 nm, as shown by the line profile in Figure 5.5(c). Figure 5.5(d) shows the orthogonal crystallographic directions for this sample on the left hand side, as well as two <110> directions, which highlights the well orientated facets. Figure 5.6 shows a detailed STM image of two faceted regions intersecting (2×2) terraces. It appears that the facets form by removal of material from beneath the surface [as seen from the line profile in Figure 5.5(c)], with one edge forming the face of the facet plane and the other formed by (2×2) terraces stepping downwards, i.e. a vicinal surface. This is best shown at the top of Figure 5.6 where terrace steps are seen to extend upwards.

5.3.2 CdTe(111)B Surface

The CdTe(111)B surface is much more disordered and to discern the individual structures we have performed a systematic annealing study. After sputtering, the surfaces were annealed at various temperatures for typically between 1-

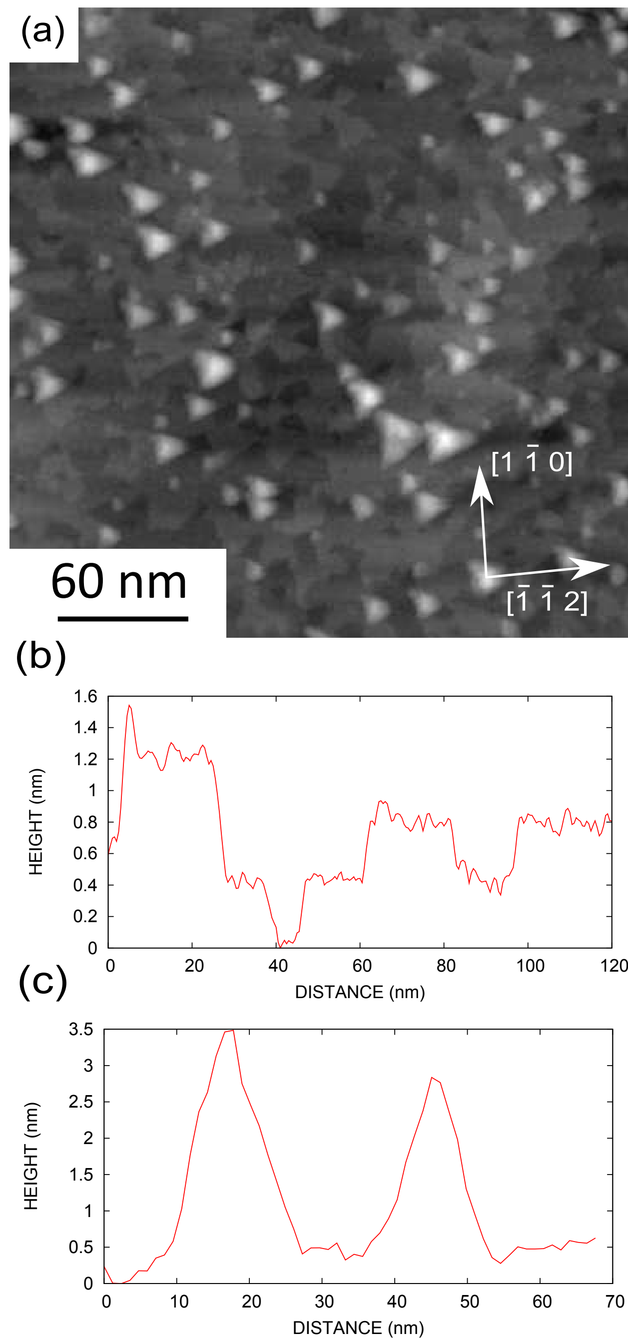

Figure 5.7: (a) Large area STM image of the CdTe(111)B surface after annealing at 275°C. The surface shows terraces and large triangular based pyramids which cover approximately 5 % of the surface. Shown on a grayscale range of 5.5 nm. (b) Line profile taken across a terraced region on the surface. Step heights are measured to be about 4 Å. (c) Line profile over two adjacent triangular based pyramids. They are found to be typically 4 nm in height.

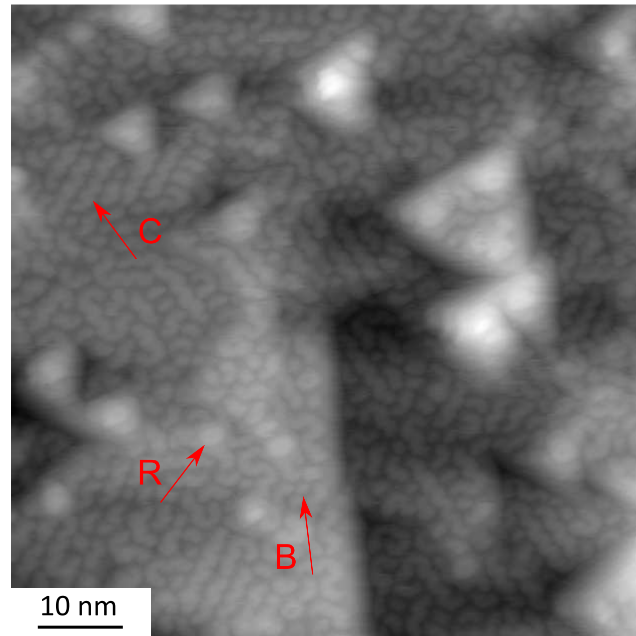

Figure 5.8: Surface reconstructions of the (111)B surface. Chain structures are highlighted by the arrow labeled C. Ring structures are highlighted at the arrows labeled R.

2 hours. For surfaces annealed at temperatures below 220°C we observe no ordered surface structures. On annealing at 250°C we start to observe some surface ordering although the ordering is still very poor. The structuring is more evident after annealing at this temperature for greater than 2 hours. For higher annealing temperatures the surface ordering is more apparent with terraces beginning to form. This is shown in Figure 5.7(a) which shows a large area STM image of the surface. We see a terraced structure with large pyramid features superimposed. Line profiles across the terraces show the steps to be about 4 Å in height [Figure 5.7(b)], i.e. slightly larger than one CdTe bilayer. This discrepancy may be due to the high surface disorder, which is demonstrated by the poorly resolved steps in the line profile. Figure 5.7(c) shows a line profile across two pyramids in close proximity. They are found to be about 4 nm in height and extend over about 20 nm, and have their edges aligned along <110> directions.

Before discussing these facets in more detail, we first examine the surface reconstructions observed on the terraces mentioned above.

Figure 5.8 shows a detailed STM image of the (111)B surface reconstructions. There is a large amount of disorder on the surface with poor long range ordering. We can however see ordered chain structures (as shown by the arrow labeled "C") which align along <211> type directions. These form either small ordered domains, or exist alone, or exist as incomplete structures (i.e. small chains, chains with poor inter-chain ordering or chains with hooked heads). The small domains typically only exist over about five or six chain widths, whilst the chain lengths are typically limited to about 10 nm. We also observe some ringed structures (labeled by "R") as well as individual "building units", labeled "B". A detailed image of the ringed and building unit structures is shown in Figure 5.9(a). The building units appear as individual circular beads, however on closer inspection we can see they are slightly extended along <211> type directions. Detailed images of the ringed structure [Figure 5.9(b)] show it to have a hexagonal symmetry. As was shown by Duszak *et al.*[117], a semiconducting (electrically neutral) surface can be constructed with two tellurium atoms bound to five cadmium atoms in a two layer structure, as shown in Figure 5.9(d). This building unit could be used to construct a hexagonal ring model [Figure 5.9(c)], similar to that found on GaAs(111)B -($\sqrt{19} \times \sqrt{19}$) surface, whilst still maintaining the electron counting criterion [121]. This ringed structure is what we observe here by STM. These hexagonal rings were not identified by Duszak et al., probably because they are few in number and show very little ordering between them and so cannot be seen in a RHEED pattern. Generally we seem to observe them at surface protrusions or near to steps. Due to the poor ordering between rings, we propose that they are energetically unfavorable to form on the surface. However, near to steps or on small surface protrusions, where there is surface confinement, they are able to form. In addition, we generally found the rings to be more numerous after annealing at lower temperatures (lower than 250°C) although the ordering between them was still very poor. There are two possible explanations for this: either the surface is slightly more tellurium rich at lower temperatures allowing

more rings to form, or the surface is less smooth due to sputtering damage, meaning there are more defect sites at which rings can form. We expect it is a combination of the two.

The chain structures form the principal surface reconstruction observed on this surface. The surface unit cell is $c(8 \times 4)$ and this was previously identified by Duszak et al. to have glide planes in <211> directions. Glide plane symmetry involves mirror and translational operators, so in this case, the principal structural motif has to be mirrored and translated in a (211) plane to reproduce itself. In this work (for example as shown in Figure 5.8) the chains are found to run parallel to any of the <211> directions and therefore are rotated by 120° with respect to each other. Figure 5.10(a) shows a detailed STM image of the $c(8 \times 4)$ reconstruction along with the proposed atomic model. Here we identify the infinitely long chain structure running parallel to the [211] direction. The chains consist of a double alternated row made up of principal building units, as shown in Figure 5.10(b). This structure also maintains the electron counting criterion since it has the same stoichiometry per unit area as that of the principal building unit. The fact that the chains can run parallel to any of the <211> directions may be a principle reason for the high surface disorder: there is no energetically favorable orientation for chains, so small rotated domains can easily form, with the domain boundaries typically producing disordered regions at which other structures can be made.

We failed to observe the $(2\sqrt{3}\times2\sqrt{3})$R30° reconstruction observed at higher temperatures as was identified by Duszak *et al.*. However, we generally observed a breaking up of the $c(8\times4)$ chains at higher temperatures into smaller components, for example as can be seen in Figure 5.11(a). The high surface disorder means that any long range reconstructions are inhibited and therefore difficult to observe on the local scale by STM. However, a large area averaged method like RHEED would probably be able to discern this structure. Furthermore, as will be discussed below, surface facets begin to grow in size at higher annealing temperatures and thus may conceal this reconstruction.

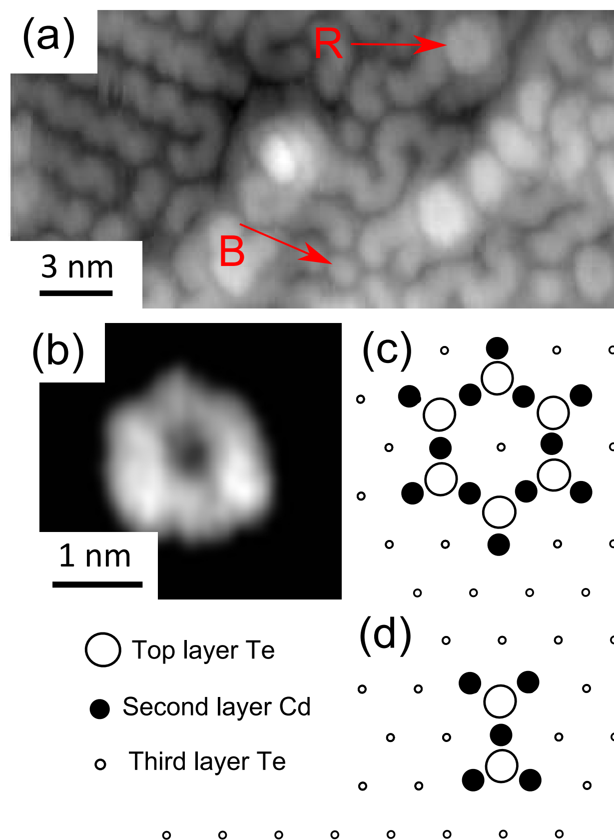

Figure 5.9: (a) STM image of the CdTe($\bar{1}\bar{1}\bar{1}$) surface detailing ring structures (labeled R) and individual building units (labeled B). Chain structures can be seen on the left hand side. Sample bias: -2.5 V, tunnel current: 0.1 nA, grayscale range: 1.1 nm. (b) Detailed image of the ring structure. A background subtraction has been applied to emphasize the structure. (c) Proposed model for the ring structure. (d) Proposed model for the building unit.

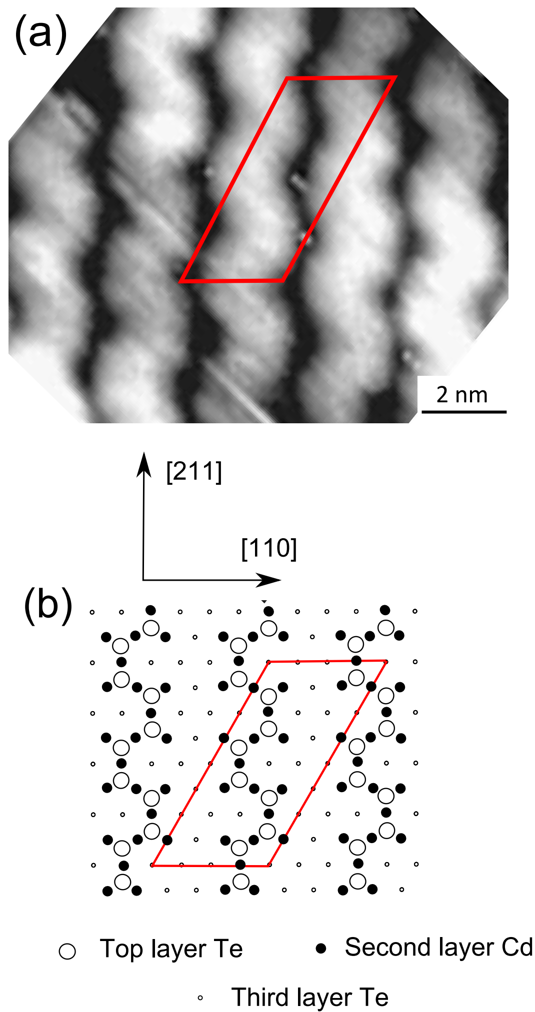

Figure 5.10: (a) Detailed image of the $c(8 \times 4)$ reconstruction. (b) Model of the $c(8 \times 4)$ reconstruction. Large and small open circles denote the first and third layer tellurium atoms, respectively. Filled circles denote second layer cadmium atoms. In both images one surface unit cell is shown.

Faceted structures are produced by forming triangular based islands on top of the surface. Material to produce these structures appears to come from the local surrounding regions as shown in Figure 5.11(a). Here we see depressions either side of the facets where material is missing, and is presumably used to build the faceted structure. In addition, we can observe the individual atomic planes that make up the pyramidal structure. These planes are better observed in the derivative image (dz/dx) as shown in Figure 5.11(b). The central pyramid in this image is 6 atomic planes in height. Often a small accumulation of material is found to form at the apex of the pyramids and is particularly evident for the taller pyramids, the reason for this is not clear at present.

The extent of faceting increases for higher anneal temperatures (greater than 325°C) with the facets increasing in both height and lateral extent. The surface has complete coverage at temperatures greater than 350°C [see Figure 5.12] and the surface has a very rough morphology with the pyramids becoming up to 60 nm in height. Again we see that the pyramids are topped by a small accumulation of material.

We can use this faceting to identify certain surface defects and image them on the atomic scale. Figure 5.13 shows an STM image of a line defect intersecting the (111)B surface. The image is shown as the derivative of the topographic height (dz/dx). We chose to present the image in this form because it highlights the faceted structures over that of the rest of the surface. The line defect runs diagonally across the image and is found to be parallel to the <100> directions. We can clearly see pyramid structures (facets) dotted all over the surface, in addition to the various surface reconstructions in between the faceted structures. Either side of the line defect the pyramid structures appear to be aligned anti-parallel to one-another, i.e. the line defect represents a mirror plane. Considering this, we can comprehensively conclude that the line defect is a twin boundary.

CdTe is quite prone to twinning, especially for growth in the [111] direction.

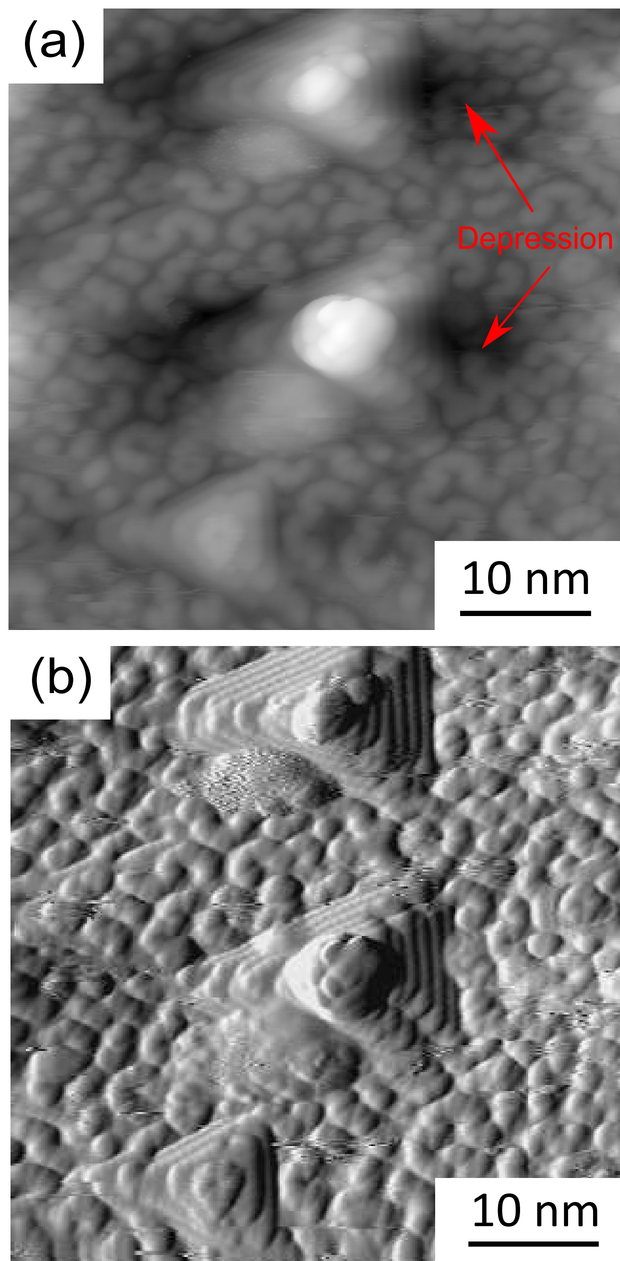

Figure 5.11: Detailed images of three triangular based pyramids. (a) Topographic height image shown on a grayscale range of 7.6 nm. Depressions near the faceted structures are highlighted. (b) Derivative of (a) highlighting the steps on the pyramid structures.

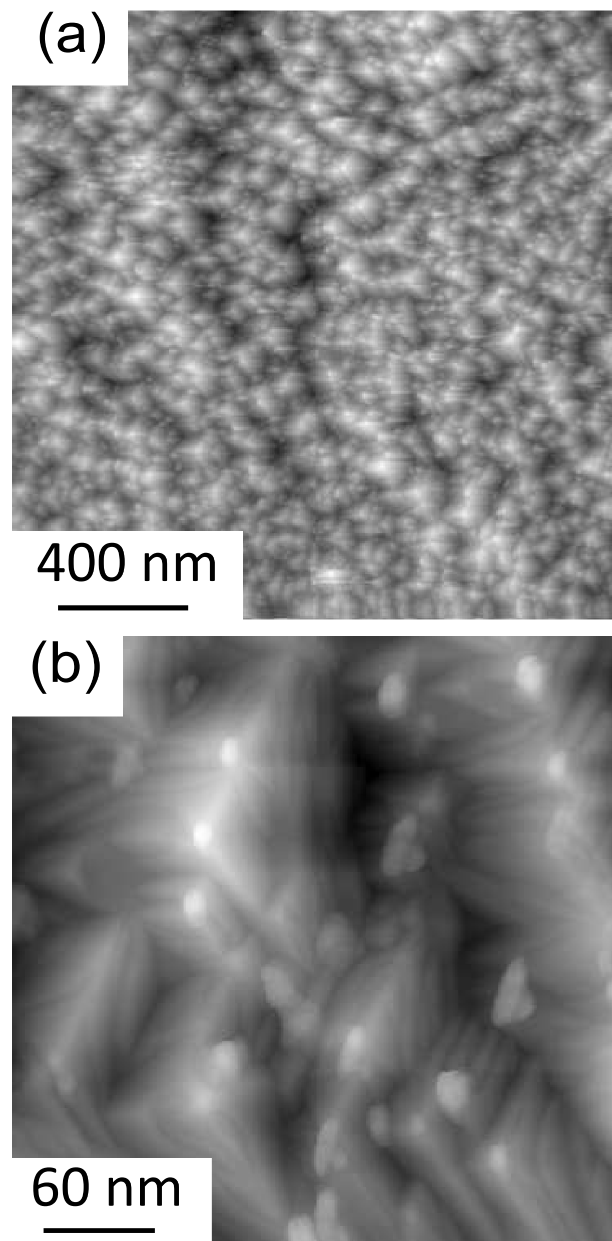

Figure 5.12: Two STM images of the CdTe(111)B surface after annealing at 375°C for 1 hour. The surface is completely covered in triangular pyramid facets. Images are shown on grayscale ranges of (a) 60 nm (b) 35 nm.

This is due to the low stacking fault energy which results in the formation of so-called lamella twins whereby the stacking sequence in the [111] direction is disrupted [122, 123, 124]. Indeed, X-ray diffraction analysis of the CdTe films grown on GaAs(111)B substrates for this study, revealed them to be highly twinned [see Section 5.2]. Instead of the usual ABCABCABC stacking sequence, lamella twins have the stacking sequence ACBACBACB, where the fault in the sequence defines the lamella or coherent twin boundary. Running perpendicular to the {111} plane, so-called double-positioning or incoherent twin boundaries occur. These have a higher surface energy due to disorder in the bonding sequence. It is these twin boundaries that intersect the (111) surface and can be imaged by STM. Schematic diagrams of twin boundaries common to CdTe, along with the resultant crystal structures, are shown in Figure 5.14. By considering the atomic arrangement shown in Figure 5.14, we can conclusively say that the STM image of the line defect in Figure 5.13 is that of a *double-positioning* (lateral) twin boundary. The faceting on the surface has therefore been a useful tool to analyse these crystal defects. We would not have been able to distinguish the defect using the surface reconstruction alone (e.g. the chain structures). This is due to the 120° rotational degeneracy, whereby the chain structures could be aligned in any one of three different angles. So either side of the twin boundary, the surface structure would appear the same. However, the facets precisely follow the bulk crystal structure, and thus can be used to identify the defect.

5.4 Discussion

The observation of faceting for both the (111)A and (111)B surfaces is quite unique for a low index surface plane. Faceting is usually observed on higher index planes where the surface energy of that plane is high and it is energetically more favorable to split into multiple lower index surfaces. For example, the clean GaAs(211) surface is known to facet into assymetric pyramids with faces

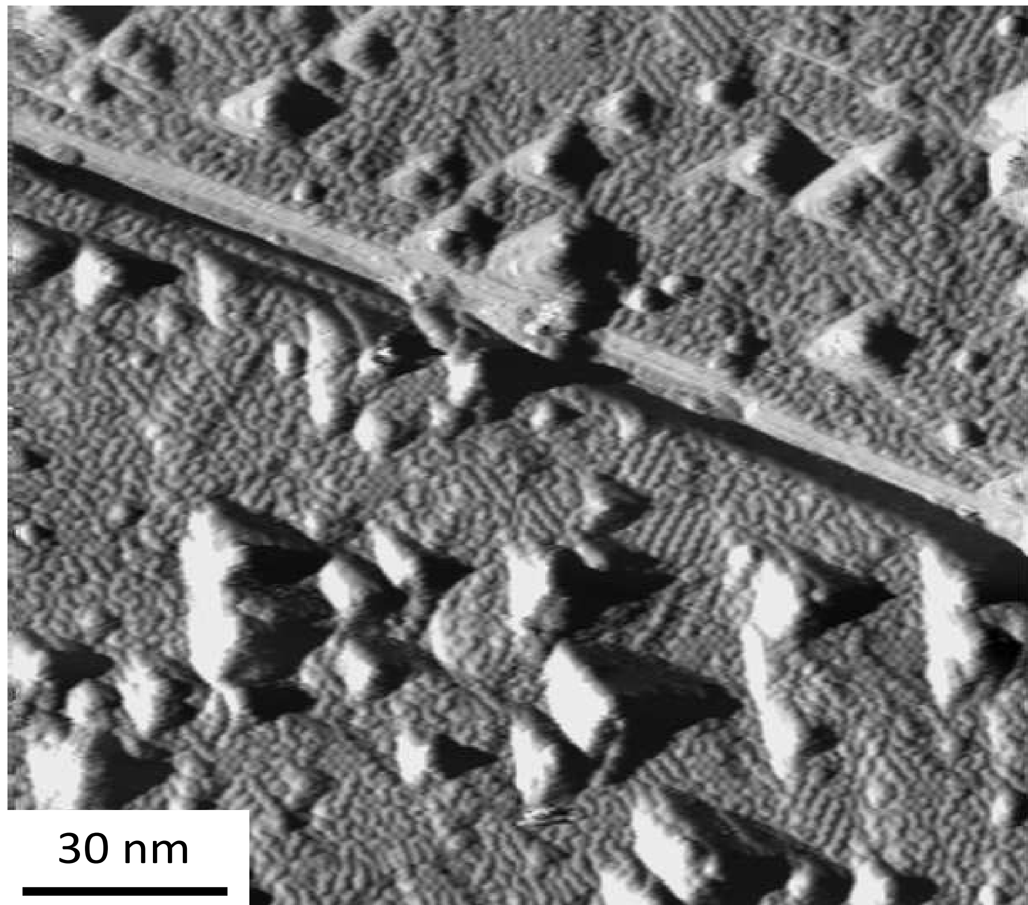

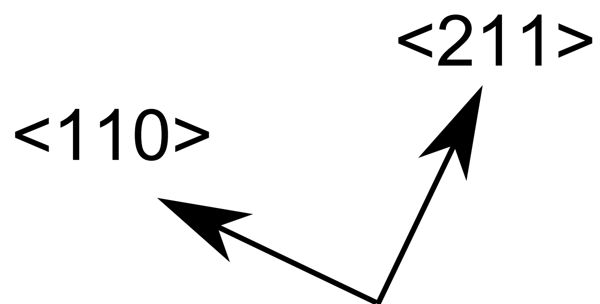

Figure 5.13: STM image (derivative) of a twin boundary intersecting the (111)B surface. Pyramid structures (facets) are seen to be mirrored in the plane of the line defect.

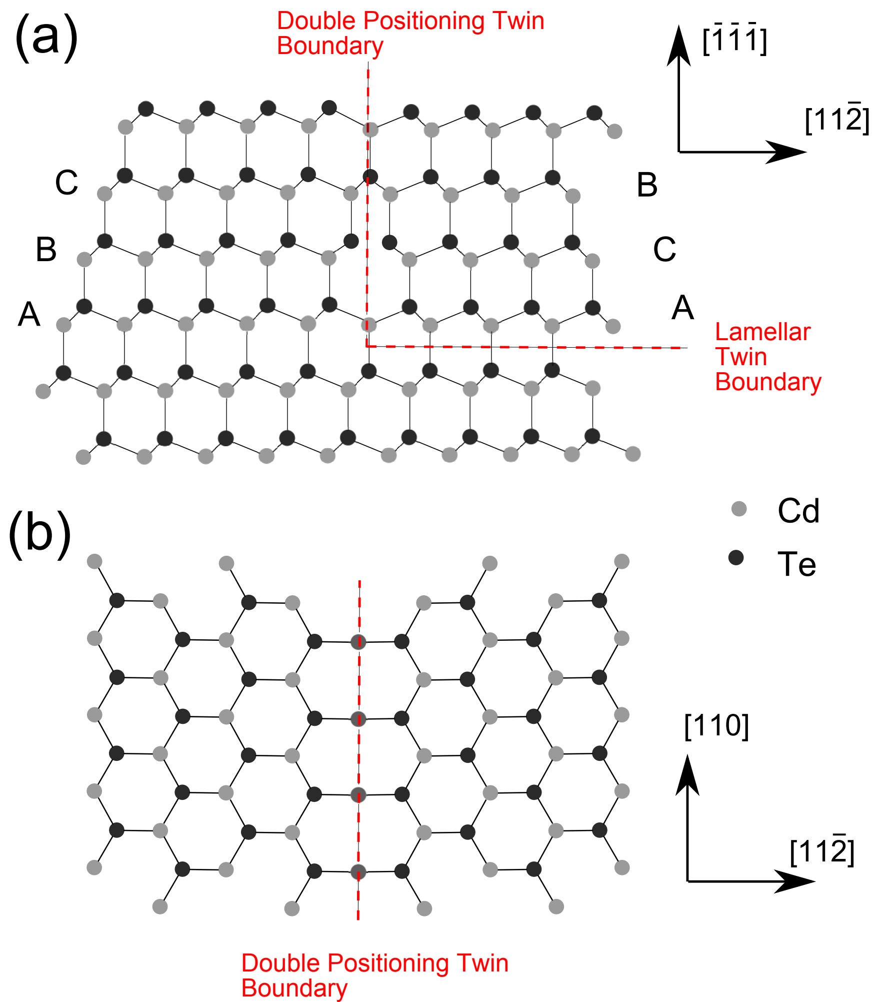

Figure 5.14: Schematic diagrams for twin boundaries common in CdTe. (a) Side view, looking along the [110] direction. (b) Top view looking along the [111] direction.

formed by (111), (101), (110) and (100) planes [125]. Although the symmetry of the facets for both the A and B faces has been well described, we have not yet specified what crystal planes form the faces of the pyramids. This in itself is quite a difficult measurement: the scanner has to be well calibrated so as to precisely measure the angle the facets form with the flat surface; and the STM image has to be carefully planed and flattened so as to remove any false height data. For our STM, we have calibrated the scanner to the interatomic distances on the HOPG(0001) surface (so we can precisely measure surface atomic structures), however we did *not* calibrate for large scale structures (e.g. greater than 100 nm, as for those features observed in Figure 5.12). Therefore we will have to assume a linear relationship to the piezoelectric response, but this is not a bad assumption for most applications. The majority of the facets observed here have sizes between 10 nm and 30 nm, with heights of around 5 nm [Figure 5.7(c)], and are thus only one order of magnitude larger than the length scales used for calibration. By taking line profiles across the faceted structures we can measure the inclined angle the faces have with respect to the {111} surface. To get a good representation of all the facets, we have measured over 100 different pyramid structures using a number of different tips at various positions on the surface. These measurements yielded a mean angle of 29° with a standard deviation of 3°. Thus 95% of the measured angles are within 6° of the mean. So realistically we should consider planes with angles between 23° and 35°. A number of potential candidates for the facets are listed in Table 5.1 along with their associated angle with respect to the (111) plane. Remember that all the families of planes to be considered must have a three-fold rotational symmetry around the [111] axis so as to form the triangular based pyramid structures observed.

Before doing this analysis, our initial thought was that the {100} planes were most likely because these are the lowest index surfaces with a three-fold rotational symmetry about the [111] axis. However, having analyzed the angles the faces form with the surface, the {100} planes can be clearly discounted.

Plane	Angle
{100}	54.7°
{110}	35.3°
{211}	19.5°
{311}	**29.5°**
{221}	15.8°
{331}	22.0°
{522}	25.2°

Table 5.1: Plane intersection angles to the {111} family of planes.

The angles are different by about 25°, so even a 200% error in scanner calibration could not account for this. Of all the other planes to be considered the {311} planes are the most closely matched to the measured angle, being only 0.5° different. The {522} and {110} family of planes are the next closest being 5° either side. Of these two, the {110} planes are more likely because they are of lower index. Considering the data spread we should therefore consider three families of planes: {311}, {522} and {110}. Of these three, the {311} planes are very closely matched to our measured angle, and so we conclude that the facets are most likely to be formed from {311} planes. Electron diffraction techniques should easily be able confirm this.

5.5 Conclusions

In conclusion, we have studied the surface morphology and surface reconstructions of clean CdTe(111)A and CdTe(111)B surfaces using scanning tunneling microscopy. The (111)A surface shows a (2×2) reconstruction which is stable over a wide temperature range. A cadmium vacancy model is proposed for this structure whereby one cadmium atom is removed from every (2×2) unit cell. This structure fulfills the electron counting rule and is analogous to that found on the GaAs(111)A surface.

The CdTe(111)B surface shows a large amount of disorder. We observe three separate surface structures. These are: a chain structure, which was found to extend in any of the <211> directions; a ring structure, with a

hexagonal symmetry; and individual building blocks, appearing as small individual beads which are slightly extended in the <211> directions. The chain structures are the $c(8 \times 4)$ reconstruction previously observed using RHEED. The ring structures and individual building blocks do *not* appear to be energetically favorable on an ideally flat surface. However they still fulfill the electron counting rule and thus can exist near surface defect sites (step edges or small terraces) where the surface confinement allows them to form preferentially over other structures. We failed to observe the $(2\sqrt{3} \times 2\sqrt{3})$R30° reconstruction that was found at high temperatures by Duszak *et al.*, but we observed that the c(8×4) chains generally broke apart at higher temperatures and this could be the beginning of the formation of that reconstruction.

For both surfaces we observed a certain amount of faceting. The facets on the (111)A surface are made from planes that embed within the surface and extend of distances greater than 400 nm, although their lateral extent remains small, typically about 50 nm. These facets form a large triangular structure with the extent of faceting increasing for higher annealing temperatures. For the (111)B surface the facets form by making small pyramid islands on top of the surface which grow in size with increasing annealing temperature. The surface is completely covered by facets at temperatures higher than 350°C, with the resultant surface having a very rough morphology. By measuring the angle at which the facets intersect the surface, we conclude that the {311} family of planes make up the facets. The facets have been used to identify double-positioning (lateral) twin boundaries intersecting the (111)B surface.

The faceting observed for both the A and B surfaces implies that the surface energy for {111} surfaces is quite large and may have profound implications upon crystal growth, especially from the vapour phase, whereby the growth interface at high temperatures actually consists of {311} planes rather than the expected {111} surface orientation.

Chapter 6

Chemically Treated Surfaces

6.1 Introduction

This chapter is concerned with the nanoscale surface morphology and electronic structure of wet chemically treated CdZnTe surfaces. Wet chemical polishing and etching for any semiconductor is an important step in the preparation of a smooth, flat, clean and defect free surface as required for metal contact deposition or in the preparation of substrates for epitaxial growth. Indeed, all of the samples studied in this thesis have at some point been prepared in this manner.

For radiation detector applications, polishing and etching in various concentrations of bromine methanol solution is usually performed before contact deposition to remove the damaged layer produced after wafer cutting and lapping. This process results in a smooth, clean surface however the surface composition is usually tellurium rich due to the preferential etching of cadmium by the bromine solution. The interaction of the metal film with the etched surface will control the electrical characteristics of that contact, so a good understanding of morphology and electrical properties of surfaces prepared in this way is essential. Passivation in oxidising chemicals such as hydrogen peroxide is sometimes performed after metal deposition to inhibit further chemical reactions and also acts to reduce the surface leakage current which can impede

detector performance [126, 127].

Traditionally, a chemical polish is distinct from a chemical etchant in that it dissolves a crystal surface uniformly without preferentially removing material from any crystal defects. In this chapter however, we use these terms interchangeably. The reason for this is to keep in accordance with the literature: The majority of the publications concerned with the wet chemical treatment of CdZnTe surfaces use the term "etch" when dealing with solutions of bromine in methanol, leaving the term "polish" for use of mechanical abrasives to produce a flat and smooth surface as a precursor to chemical treatment. We stick to this convention.

Chemically treated CdZnTe surfaces have been extensively studied over the years using surface sensitive techniques. In particular, the chemical composition has been investigated by numerous authors using techniques like X-ray photoelectron spectroscopy (XPS) and Auger electron spectroscopy (AES). It is now widely accepted that bromine etching results in a tellurium-rich surface and subsequent passivation in oxidising solutions results in a thin oxide of tellurium, most likely TeO_2 [128, 129, 130, 131, 132]. One of the questions that has yet to be solved is the origin of the high surface leakage current for chemically treated surfaces. Although studied by many authors, little physical insight has been made to that actual electronic structure of the surface. The aim of this chapter is to use scanning probe techniques to shed light on some of these unknown aspects.

6.2 Sample Preparation and Experimental Technique

In this chapter we used semi-insulating (SI) CdZnTe crystals with a 5 % zinc concentration grown by the MTPVT method. Samples were cleaved in air to produce a (110) face where the surface alignment was checked using Laue X-ray diffraction. These surfaces were then polished in several stages using a

dimaond suspension with the final polishing step made using an average particle size of 0.1 μm. Samples were then etched in bromine methanol (BM) solution of various concentrations (between 1 % and 5 % by volume) for differing amounts of time. After etching they were rinsed in methanol and dried in nitrogen and immediately loaded into the UHV chamber with a base pressure of 2×10^{-10} mbar. The time between etching and loading into vacuum was typically less than 3 minutes. In vacuum, samples were baked at 65 °C for 1 hour to remove any residual methanol that may have remained on the surface. We do not expect this baking step to alter the surface morphology or electronic properties. For passivation studies, the surface was polished using the same method as described above and then etched in a 2 % BM solution for 2 minutes. This was then rinsed in methanol and dried in nitrogen before being passivated in 30 % by weight hydrogen peroxide solution for various times (up to 2 minutes). This was then rinsed in methanol once more and then dried, loaded into vacuum and baked as described above. The time between etching and passivation was typically less than 1 minute. For all measurements, surfaces were *re-polished* before further chemical treatment and we observed no difference between freshly prepared and re-worked samples.

AFM measurements were performed using the methods described in Chapter 2. Image and roughness analysis was performed by averaging over at least 4 separate images that were recorded at different positions on the surface. Roughness statistics were calculated using Equation 2.1 and analysed using the WSxM software [133]. Due to the low sample conductivity (and high number of extrinsic surface states pinning the Fermi-level) STM/STS measurements were performed with the sample heated to 95 °C. We observed no change in the surface topography between samples studied at room temperature or at 95°C.

6.3 Results

6.3.1 Surface Morphology

Figure 6.1(a) shows a typical AFM image of the CdZnTe surface after polishing. There are a large number of scratches which remain on the surface and this is consistent with previous results [134]. It is expected that this surface damage should introduce a large number of defects (traps) and thus inhibit any device properties. Indeed, this is the whole reason why etching in BM solution is performed, to remove this damaged layer. Etching a mild BM solution (1 % by volume) for a short period of time (30 seconds) is sufficient to remove the surface scratches, although there still remain a number of surface defects as observed in Figure 6.1(b). The surface forms a hillock structure, the diameter of which is typically 40 nm. Roughness analysis (Figure 6.2) shows that the roughness has reduced significantly, although there still remains tails in the histogram which we attribute to defects that have not been completely removed. Figures 6.1(c) and 6.1(d) show the surface morpholgy after larger amounts of etching. All defects have been removed and the surface roughness has been reduced, however increased etching concentration and/or time increases the roughness somewhat. This we attribute aggressive etching and the formation of larger hillocks due to the inhomogeneous etching of cadmium.

Shown in Figure 6.3 is a comparison of an AFM image and an STM image taken from the same surface that has been etched in a 2 % BM solution for 5 minutes. Here we see that the STM image correlates well with the AFM image. The STM image was taken at negative sample bias and thus represents filled states (valence band states). We therefore conclude that no filled states are localized at any specific topographic features on the surface.

Figure 6.4 shows AFM results for surfaces that have been etched and passivated in hydrogen peroxide for varying amounts of time. The surface again forms a hillock like structure although this time the surface features are smaller typically 20 nm in diameter. The roughness has increased to 2.62 nm RMS and

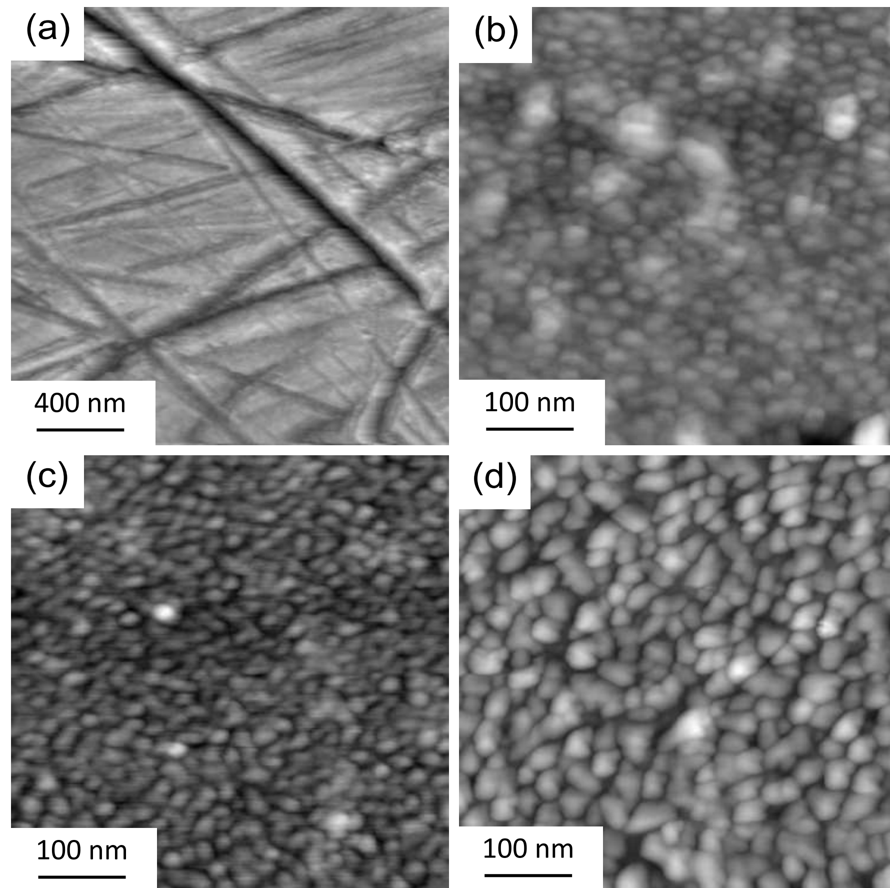

Figure 6.1: AFM images of polished and etched CdZnTe surfaces: (a) Mechanically polished, finished using a diamond suspension of average grit size 0.1 microns. (b) Polished as in (a), then etched in 1 % bromine methanol solution for 30 seconds. (c) Polished as in (a), then etched in a 2 % bromine methanol solution for 2 minutes.(d) Polished as in (a), then etched in a 5 % bromine methanol solution for 2 minutes. Images are shown on grayscale ranges of 34 nm, 13 nm, 5 nm and 11 nm respectively.

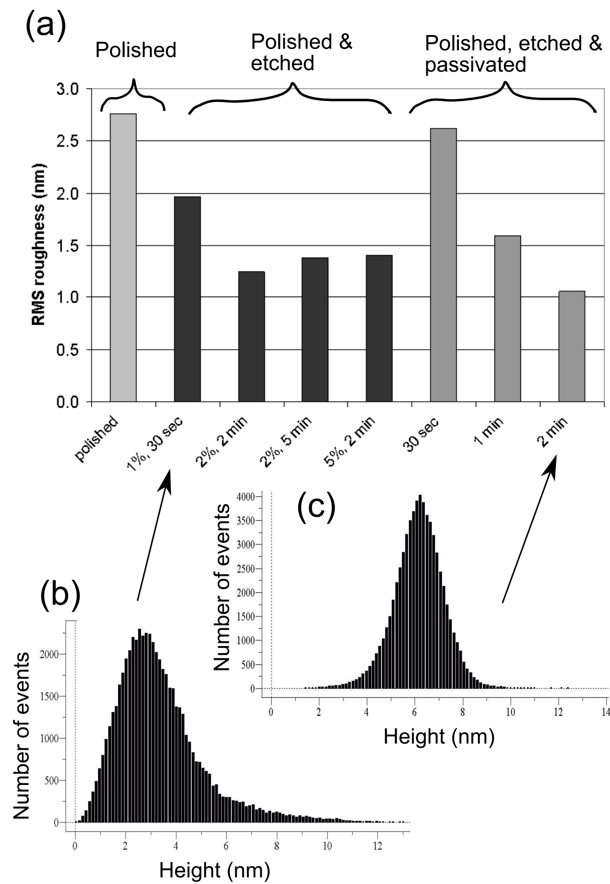

Figure 6.2: Roughness analysis of chemically prepared surfaces. (a) Overview of the root mean square roughness in nm for each preparation method. For etched surfaces, the bromine concentration is given in volume percentage, along with the time in the etchant. For etched and passivated surfaces, the time in the passivant is given. (b) and (c) Representative histogram plots of the z-coordinate for two different surface preparations.

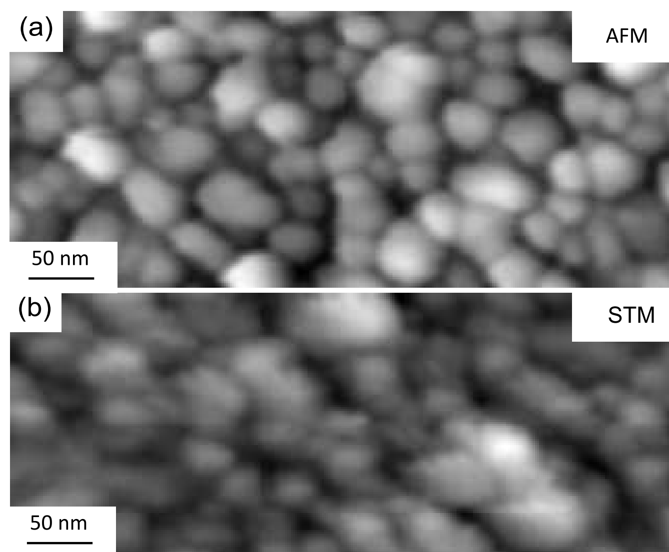

Figure 6.3: Comparison of AFM and STM images taken on the same surface which has been polished and etched in a 2 % bromine methanol solution for 5 minutes. (a) AFM image, (b) STM image acquired using a sample bias of -2.5 V and tunnel current of 0.1 nA. Both images are displayed on a grayscale range of 6 nm.

the histogram plot is symmetrical implying a uniform surface. For increased time in the passivant the surface roughness decreases, reaching 1.06 nm RMS after 2 minutes passivation. The histogram plot is again symmetrical but the peak width is reduced meaning the surface is flatter. In addition we notice that there exist a number of hole-like features most evident in Figure 6.4(b) and are detailed in Figure 6.5. These holes are typically 20 nm in diameter and about 7 nm in depth.

6.3.2 Tunneling Spectroscopy

Figure 6.6 shows a typical tunneling spectrum obtained from a surface that has been polished and etched in a 2 % bromine methanol solution for two minutes. In this figure, the spectrum is plotted on both a linear and logarithmic scale. The magnitude of the tunnel current is significantly reduced when compared to those spectra obtained from surfaces prepared in UHV (Chapter 4). This spectrum was obtained by averaging over about 20 individual spetcra over an

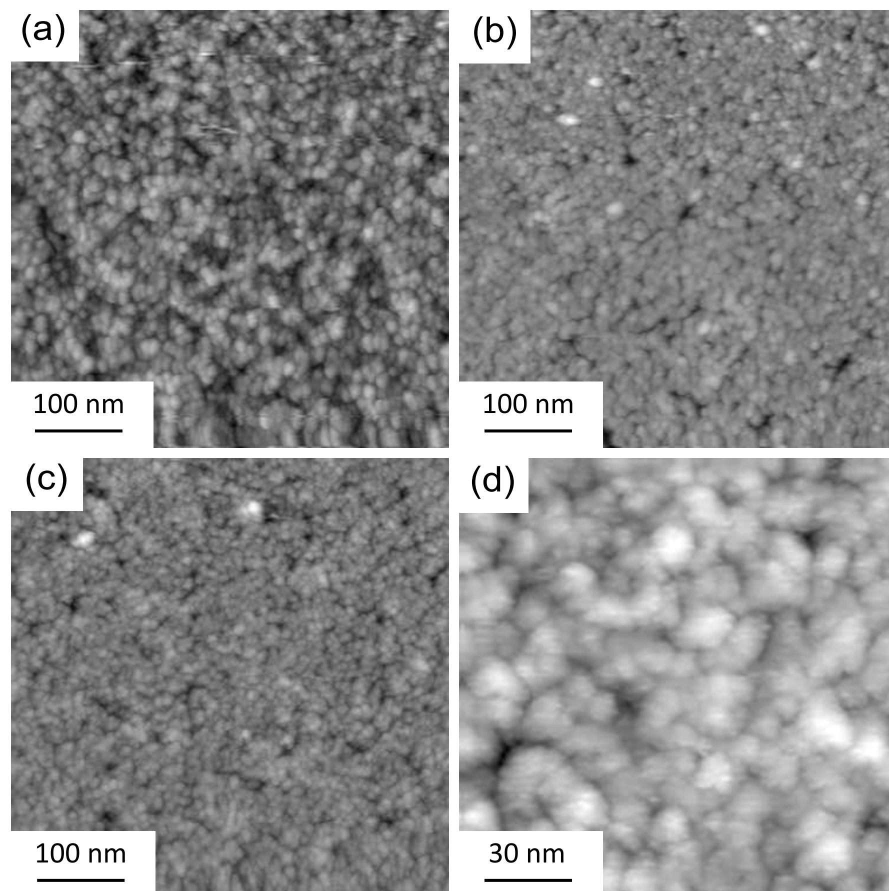

Figure 6.4: AFM images of CdZnTe surfaces etched in a 2 % bromine methanol solution and then passivated in 30 % hydrogen peroxide for: (a) 30 seconds, (b) 1 minute, (c) and (d) 2 minutes. Images are shown on grayscale ranges of 19 nm, 17 nm, 12 nm and 6 nm respectively.

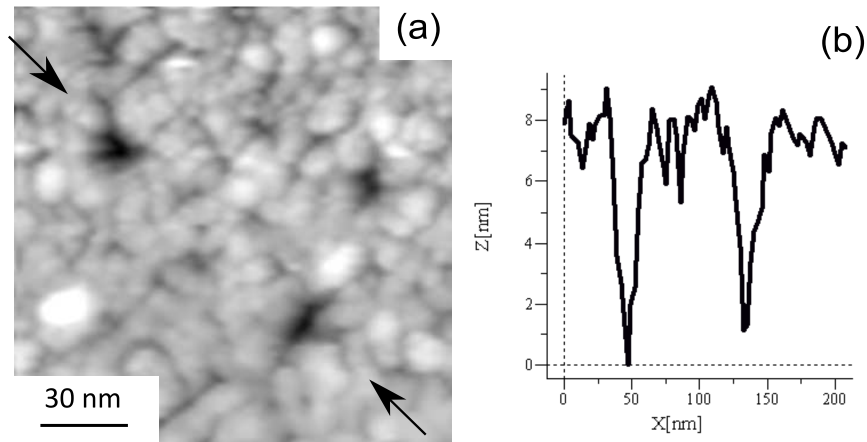

Figure 6.5: (a) Detail of hole-like features observed on passivated surfaces. (b) line profile measured between the arrows in (a).

area of about 20 nm^2. The reason for doing this was to increase the signal-to-noise ratio so we can better discern the lineshape closer to zero volts. We can see that there is still a small tunnel current at low bias voltages (below $|\pm 1|$V), i.e. there is some contribution from electronic states that exist within the band gap region. A better way to view the data is to plot the normalised conductance (as described in Chapter 4) which is shown in Figure 6.7. Here we can see a large component at negative bias peaking at about -1.5 V; a shoulder at small negative bias; and a component at moderate positive bias, peaking at about +1.2 V. There is no well defined band gap region and the conductance has a value of about 0.5 at zero volts. This is compared to spectra obtained from UHV prepared surfaces presented in Chapter 4, which show a clear band gap region where the conductance has a value of 0 at zero volts. This highlights that there is a significant contribution from electronic states that exist in the band gap region. Having plotted the normalised conductance, we can now compare spectra from different experiments.

Shown in Figure 6.8 are the normalized tunneling spectra for surfaces etched in BM solution for various concentrations and times. For all the spectra we again identify three distinct features: A peak at large negative bias, a shoulder at small negative bias, and a third peak at moderate positive bias. The

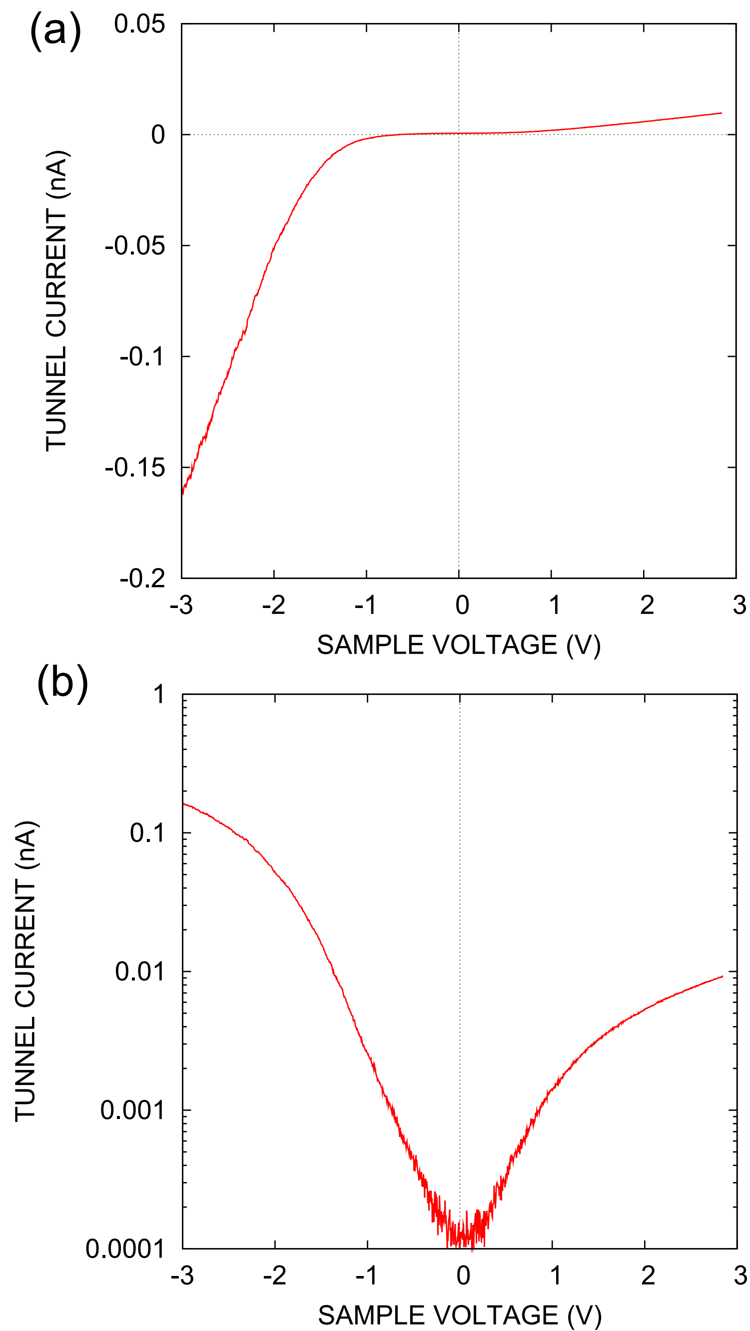

Figure 6.6: Tunneling spectrum obtained from a surface that has been polished and etched in a 2 % bromine methanol solution for 2 minutes. (a) Linear scale. (b) Logarithmic scale.

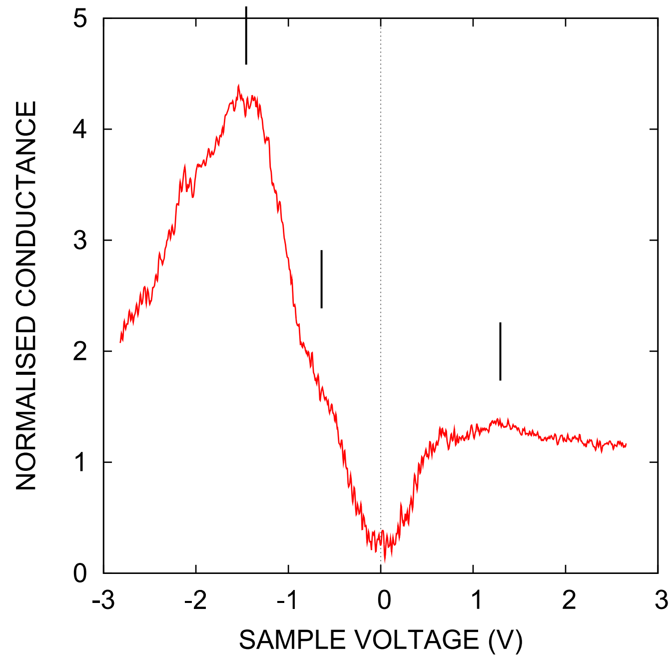

Figure 6.7: Normalised conductance tunneling spectrum obtained from a surface that has been polished and etched in 2 % bromine methanol solution for 2 minutes. Normalisation constant: 10 pA/V.

peak position for the shoulder is determined by subtracting an approximate background (given by a quadratic function), as shown in Figure 6.8(a). We apply this method to determine the peak positions for all the other shoulder-like features. As a general rule, all peak positions move out to higher bias for increased etching. However, the tip-to-tip and tip-to-sample reproducibility may shift the peak positions somewhat, as shown in Figure 6.8(b). However, even taking this into account, we still observe consistent peak shifting for increased etching. Also the general shape of the spectra remains the same, and indeed the position of the shoulder feature observed at about -0.5 V remains relatively constant. The magnitude of this peak shows some increase for each different preparation method, but the increase is smaller than that observed for the first peak. For a surface with a high number of extrinsic surface states (as is likely to be the case here) we would expect the Fermi-level to be pinned to somewhere near mid-gap and since the band gap of CdZnTe is around 1.6 eV, we can roughly place the valence band maximum at about -0.8 V and

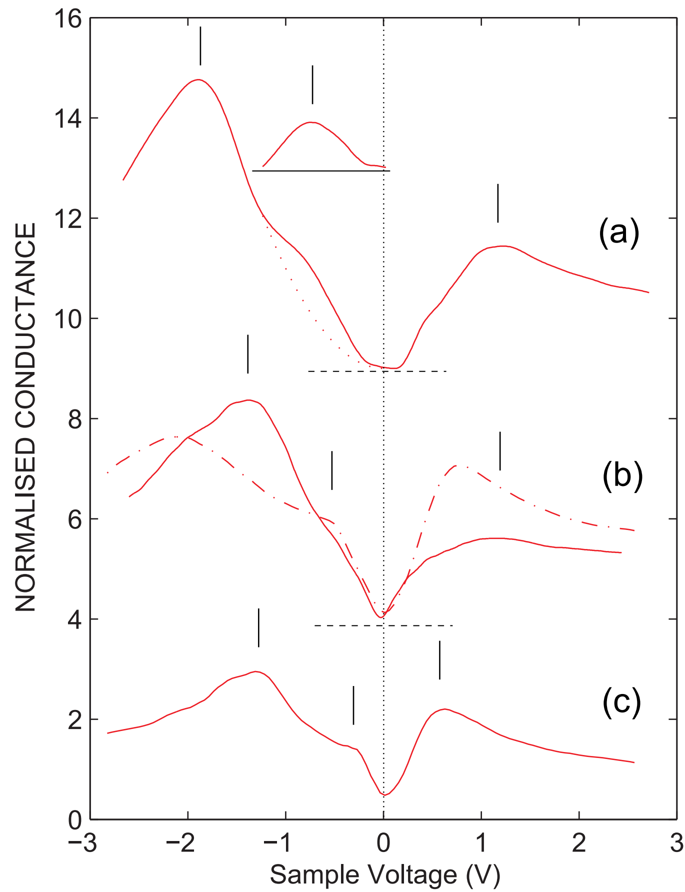

Figure 6.8: Normalised tunneling spectra for etched CdZnTe surface. Peak positions are indicated by vertical lines. (a) Etched in a 5 % bromine methanol solution for 2 minutes. The dotted line is an approximate background used for determining the peak position of the feature near -0.7 V, with the difference spectrum shown above the raw spectrum. (b) Etched in a 2 % solution for 2 minutes. The dot-dashed line, shows a spectrum taken on a different sample using a different probe tip. (c) Etched in a 1 % solution for 30 seconds. Upper spectra are offset vertically for clarity with the horizontal dashed lines indicating the zero level.

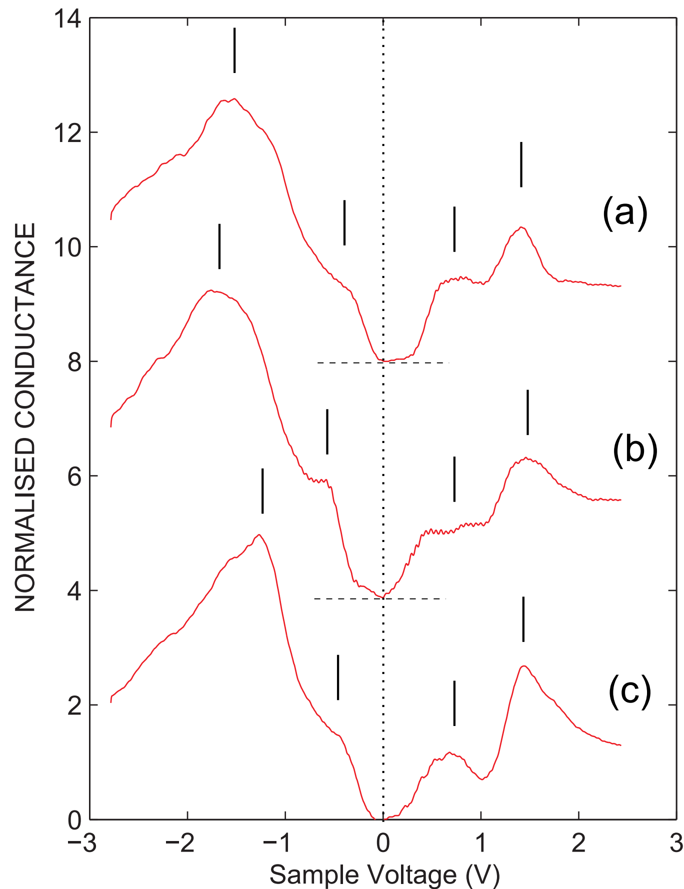

Figure 6.9: Normalised tunneling spectra for etched and passivated surfaces. Vertical lines indicate peak positions. All surfaces were etched in a 2 % bromine methanol solution for 2 minutes and then passivated in 30 % hydrogen peroxide for (a) 2 minutes, (b) 1 minute and (c) 30 seconds. The upper spectra are offset vertically for clarity with the horizontal dashed line indicating the zero level.

the conduction band minimum at about 0.8 V. Therefore the shoulder feature exists *within* the band gap region and since it is observed at negative bias, it therefore has a donor-like charging character. By the same argument the third peak also exists within the band gap, but is observed at positive bias, thus it has an acceptor-like charging character. For increased etching the peak moves out of the band-gap region however it still has tails that extend into the band-gap due to inhomogeneous broadening effects from the amorphous nature of the surface.

Shown in Figure 6.9 are normalised tunneling spectra surfaces that have

been polished, etched and then passivated in hydrogen peroxide. These spectra show broadly the same features as that observed on the etched surface. We observe the same large peak at large negative bias and the shoulder feature at small negative bias. We also observe an apparent increase in the observed band gap. The most obvious difference in the spectra is that we now observe two peaks at positive bias. The first of peak lies at about 0.6 V, the second lies at about 1.4 V. These peaks are much narrower than those observed on simply etched surfaces and show little change in position for different passivation times.

6.4 Discussion

6.4.1 Etched surfaces

The classic description of tunneling spectroscopy involves that of electrons either tunneling from filled states of the tip into empty states of the sample (conduction band), or tunneling from filled states of the sample (valence band) into empty states of the tip. Thus a measurement of the position of a particular peak in the tunneling spectra would yield its exact energetic position relative to the sample Fermi level. However for semiconductors, the reduced bulk charge density allows some of the applied potential between the probe tip and the sample to be dropped in the sample itself. This effect is known as tip induced band bending (TIBB) and causes electronic states to be pushed to higher biases [35, 34]. As shown in Figure 6.8, the peak positions tend to move out to higher bias for increased etching, this we attribute to TIBB. For higher amounts of etching more surface defects are removed (as shown by AFM images and roughness analysis). This lowers the surface pinning, thus allowing more TIBB and pushing all spectral features to higher bias. Of course there is still a certain amount of pinning from the surface states themselves, however this pinning is localized at those particular states in the voltage spectrum, not throughout the band gap region as would be expected for structural defects

[91].

We now discuss the physical origin of the observed surface states. Surface states are usually characterised by their charging character whereby the surface band is filled with electrons up to some energy known as the charge neutrality level. Below this energy, states are neutral when filled and positively charged when empty; above this energy, states are negatively charged when filled and neutral when empty. The former types of surface states are known, by definition, as donor-like and the latter as acceptor-like [1]. The position of the charge neutrality level is of course unknown; however a safe estimate is to place it mid-gap such that it coincides with the Fermi-level in the bulk. As a result, donor-like surface states reside close to the valence band and acceptor-like states reside close to the conduction band. In any case, the observation of a particular surface state at a particular sample bias in a tunneling spectrum usually identifies its charging character. For example, the observation of a surface state at negative bias (i.e. filled states) implies that electrons have filled this state and it therefore lies below the charge neutrality level and thus means it is donor-like.

Based on this theoretical framework, consider now the individual peaks in the spectra. The large peak observed at large negative bias is attributed to the valence band, i.e. electrons tunneling from filled valence band states into empty states of the tip. The onset of this band is obscured by the shoulder observed at small negative bias. This shoulder is a donor-type surface state (since it exists at negative bias), which is broadened due to the amorphous nature of the surface, such that it has tails that penetrate into the band gap region. Since this peak shows some increase in magnitude with increased etching we tentatively suggest that this state is cadmium related. Bromine is well known to preferentially attack cadmium, so this state is most likely to be due a cadmium vacancy. Since a missing cadmium ion would leave behind negatively charged tellurium ions, this defect would be donor-like, consistent with our observation. The third peak observed in the spectra is an acceptor-like

surface state. We attribute this state to tellurium, most likely tellurium dangling bonds because the surface is well known to be tellurium rich after etching. This state is very broad, most likely due to the amorphous nature of the surface, and obscures the conduction band onset, which is the origin of the tunnel current at large positive bias. The energetic position of these states broadly agrees with those found by Yang *et al.* [135] using surface photovoltage, who identified both donor-like and acceptor-like states near to the band edges for chemically etched surfaces. As we have shown, these states are very broad and the exact energetic positions are difficult to measure.

As a general observation, even for well etched surfaces the conductance at zero bias is above zero and there is no clear band gap. There are tails of the electronic states that penetrate into the band gap region. From this we conclude that etched surfaces have their own surface band structure derived from a number of donor-like and acceptor-like surface states arising from defects which are inhomogeneously broadened due to the amorphous nature of the surface (as observed by AFM), such that they extend into the band gap. This results in a band gap that is now quite narrow (perhaps not even zero since some states may still exist below the sensitivity of the instrument) allowing charge hopping between states at room temperature and hence the increased surface conductivity. The proposed surface density of states (DOS) is schematically shown in Figure 6.10(a). The actual *magnitude* of the DOS is difficult to measure using STM however we can make an estimate based on the number of surface atoms. For the (110) surface (as studied in this work) the atomic density is 3.3×10^{14} cm^{-2} for either cadmium or tellurium. We expect the density of surface states to be somewhere in this range, probably between 10 % to 100% of this value. It is difficult to imagine a number higher than this. This analysis may also help to explain the larger surface conductivity found on (111) surfaces [136]. The atomic density for (111) surfaces is 5.5×10^{14}cm^{-2} implying there are probably 66% more electronic states allowing for an increased frequency in charge hopping.

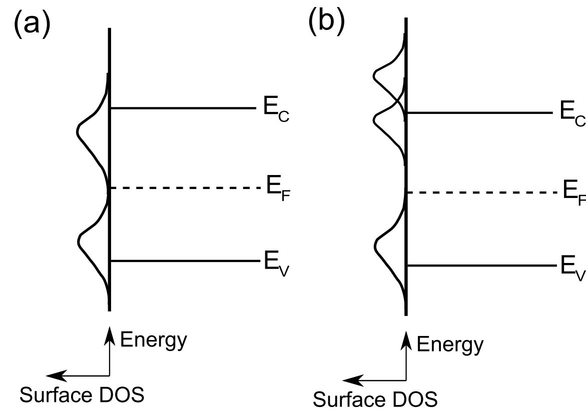

Figure 6.10: Schematic energy diagram for the surface density of states (DOS) found from STS experiments. (a) Bromine methanol etched surface showing broadened donor-like and acceptor-like surfaces states across the band gap region. (b) Etched and passivated surfaces showing additional higher lying acceptor surface state and increased surface band gap.

6.4.2 Passivated surfaces

We interpret the AFM results for passivated surfaces as the evolution of the formation of the oxide layer. After the surface is immersed in the passivant the oxide layer begins to form in a cluster-like manner. From previous reports, this oxide layer is strongly believed to be TeO_2 [128, 129, 130, 131]. As the reaction continues, the clusters begin to coalesce, resulting in a flatter, more uniform surface, however resulting in the observed hole-like features where surrounding clusters have not yet combined. Eventually all holes (exposed surface underneath) are filled in and the passivation is complete. Previous reports estimate the TeO_2 layer to be around 5 nm thick [137, 132]. Based on the observed distribution of hole depths we estimate the oxide thickness to be about 7 nm. However we must take into account the surface roughness before the formation of the oxide, i.e. at what height was that surface feature before passivation. Considering this, the revised surface oxide thickness is estimated to be about 4 nm, in-line with previous findings.

The tunneling spectra for passivated surfaces show the introduction of a

fourth peak and subsequent movement of the third peak down to lower biases. This confirms that these two peaks (or peak for simply etched surfaces) are Te related, since the surface oxide is strongly believed to be TeO_2. We interpret the peak splitting to be due to the creation of tellurium - oxygen bonds. As is often observed by XPS, the Te^{4+} cation is created after oxidation, and since this is an acceptor, we associate this to the highest lying peak observed in the spectra. The chemical origin of the lower lying peak is unclear, it is perhaps remnant dangling bonds that have yet to bond with oxygen. XPS studies often show a remnant of the Te^0 peak after passivation in H_2O_2, however for stronger oxidizers, such as NH_4F/H_2O_2, the Te^0 peak is completely removed. Thus for the chemicals studied here we may expect some dangling bonds to remain on the surface. One obvious feature of the spectra is that the peaks have become narrower, with fewer states penetrating into the band gap. This narrowing seems to suggest a more uniform interface, since any broadening is usually caused by defects. We liken this to that seen for oxidized silicon surfaces, where a good uniform interface is created, even though the surface is still amorphous [138]. Finally, because of this, a wider, better defined surface band gap exists. This reduces the surface conduction because there is less charge hopping between states. The proposed surface density of states is schematically shown in Figure 6.10(b).

6.5 Conclusions

In conclusion, the morphology and electronic structure of chemical treated CdZnTe surfaces has been studied using scanning probe techniques. We find that for surfaces etched in solutions of bromine, the structural defects arising from polishing are removed, however a number of donor-like and acceptor-like electronic states are introduced, and are thought to be from Cd vacancies and Te dangling bonds, respectively. The amorphous nature of the etched surface broadens these states such that they have tails that penetrate into the band

gap region, effectively creating a narrow surface band structure. At room temperature, there is significant charge hopping these states which increases the surface conductivity. For passivated surfaces, based on AFM results, we estimate that a 4 nm thick oxide layer is produced. This layer is quite uniform and additional acceptor-like surface states are introduced at higher energies. The increased uniformity seems to narrow the width of the electronic states resulting in an increased surface band gap. This reduces the rate of charge hopping and therefore lowers the surface conductivity.

Chapter 7

Summary

This thesis has focused on the study of the structure, morphology and electronic properties of CdTe and CdZnTe surfaces using scanning tunneling microscopy. The scanning tunneling microscope is a very powerful tool for studying structures on the nanometer and atomic scale. Coupled with tunneling spectroscopy, precise spatial probing of local electronic states can be achieved. In this thesis we have used these techniques to systematically study the three low index surface planes of cubic CdTe crystals.

The first experimental chapter discussed the (100) surface plane. To start with, we laid out the mechanisms required to produce clean surfaces in ultra-high vacuum (UHV). Clean surfaces are made by performing argon ion sputtering followed by annealing; with the former removing any surface contaminants and the latter restoring the surface crystal structure. We systematically studied the surface morphology for a range of different argon ion energies, fluxes and incident angles. We found that a rippled surface structure was formed for argon ions impinging on the surface at grazing incidence. This rippled structure formed because of the competition between erosion and surface diffusion, whereby regions with positive morphological curvature are eroded faster than regions with negative curvature. We also found that surfaces sputtered with very high fluxes, were inhomogeneously etched, forming very deep etch pits on the surface, possibly preferentially etching regions of high defect density.

Based on these studies we found that using a beam energy of 1 keV and flux of 8 μAcm^{-2} for 30 minutes produced flat, clean and reproducible surfaces. The next step was to anneal the surface in vacuum, which restores the surface crystal structure, allowing the lowest energy surface structure to form. The resultant surface *reconstruction* reflects the competition between the energy associated with dangling bonds at the surface and the strain induced between the atoms due to electronic rearrangement. For the (100) surface, a mixed phase of $(2 \times 1) + c(2 \times 2)$ reconstructions consisting of two-fold coordinated cadmium atoms sitting upon the bulk terminated structure was found to form after annealing at temperatures in the range of 200°C to 300°C. The so-called *electron counting rule* was used to explain the formation of this mixed surface phase. Having identified the surface reconstruction, we moved on to discuss vicinal surfaces, that is surfaces offcut by a small angle towards a particular direction or plane. We found that for surfaces offcut towards the (111) plane, surface steps were found to run parallel to <100> directions, forming a zig-zag pattern. This was in contrast to surfaces offcut towards the (110) plane, whereby steps were found to run very parallel to each other. These results suggested that the <100> type direction steps are energetically favourable, and could be explained by considering the bulk crystal structure.

Having demonstrated that clean, well defined surfaces could be prepared in vacuum and studied on the atomic scale, we moved on to study the (110) surface plane. The (110) plane forms the cleavage plane, which allows for simple surface preparation. Unfortunately, cleavage could not be performed in vacuum so argon ion sputtering and annealing was still required. This therefore lead to a relatively large number of surface steps to form on the surface. However, the surface crystal structure could still be clearly identified. Due to the equal numbers of anions and cations on the bulk terminated (110) surface, no surface reconstruction is formed (or to put it another way a (1×1) reconstruction is formed). This reconstruction appeared as rows aligned along the $[1\bar{1}0]$ direction due to the reduced distance between surface atoms in that

direction. For this surface, we extensively employed tunneling spectroscopy to study the surface electronic structure. The (110) surface is ideal for this since the dangling bond surface states lie outside the band gap region, preventing any surface pinning. It is also perfect for studying heterostructures in cross section by probing structures grown along the [100] direction after cleavage; or for studying electronic states within the band gap e.g. from metal overlayers; these are two possible areas for future study. The aim of the current work was to investigate and understand the spectral lineshape, with a view for future study. Indeed, the spectroscopy presented in this chapter represents the first tunneling spectroscopy investigation on CdTe and CdZnTe surfaces. For this study we investigated both n-type and semi-insulating (SI) material. Through calculations of the tunneling spectra based on the Bardeen formalism using the tunneling equations developed by Tersoff and Hamann which takes into account the effects of tip induced band bending (TIBB), we were able to fit to the experimental data and gain significant insight into the tunneling mechanisms involved. We found that for SI material, tunneling spectra were highly rectified giving large amounts of current at negative bias but very little at positive bias. As a result, topographic STM measurements could only be obtained at negative sample bias. This effect was explained by the very high TIBB due to the low material doping leading to an accumulation layer forming at the surface at negative bias, but only a small contribution from empty extended states at positive bias. For n-type material, we found that extrinsic surface states (electronic states from surface defects or disorder) played a strong role in screening the electric field from the metal tip and limiting the TIBB and yielding spectra that were a lot less rectified, but displayed a surface band gap smaller than that of the bulk. The difference in the apparent charging character of extrinsic states on SI and n-type material was explained by considering the spreading resistance at the near surface region.

The third experimental chapter discussed the third low index surface plane, the (111) plane. The (111) surface plane is in fact polar such that there is

no centre of symmetry between the (111) and $(\bar{1}\bar{1}\bar{1})$ planes. This results in drastically different surface chemistry for the two faces. On the atomic scale, the 'A' face was found to have a (2×2) reconstruction where cadmium atoms form the top atomic layer. For every other surface unit cell one cadmium atom was found to be missing yielding the (2×2) lattice. This structure was predicted by considering the electron counting rule. The 'B' face was found to be highly disordered showing a variety of different surface structures. The principle structure was a double layer chain structure terminated in tellurium atoms. This structure has a $c(8\times4)$ surface lattice and was previously identified by electron diffraction techniques. In addition to this we observed: a ring structure with a hexagonal symmetry; as well as individual building units which are made from five cadmium atoms and two tellurium atoms in a two layer structure. For both surfaces we observed a certain amount of faceting, with the faces formed by {311} planes. For the 'A' face, the facets had a very large lateral extent; whereas for the 'B' face the facets were formed by producing small pyramid structures approximately 10 nm in lateral extent. The results presented in this chapter have very high scientific impact for two reasons. Firstly, the STM images presented in this thesis are the first *real space* identification of the surface reconstructions. This is compared to reciprocal space identification (e.g. using electron diffraction) which can only identify the surface periodicity. Secondly, the observation of faceting suggests that the surface energy of the {111} planes is quite large. This is the first experimental evidence of this effect and is quite interesting since low index surface planes of zincblende semiconductor generally *do not* form faceted structures. Going further, using these faceted structures we able able to explicitly identify twin boundaries that intersected the 'B' face. Indeed, the results presented in this chapter may go some way to explaining why CdTe is very prone to twinning for growth in the [111] directions.

In the final experimental chapter we studied the surface morphology and electronic properties of chemically treated surfaces. For CdTe and CdZnTe,

polishing and etching in various concentrations of bromine methanol solution is often performed so as to produce a relatively clean flat surface as required to deposit metal electrical contacts for producing semiconductor devices. This is sometimes followed by passivation in hydrogen peroxide which acts as a passivant, thus preventing further surface oxidation and also reduces surface leakage (which is important for radiation detectors). We systematically studied the surface morphology (using AFM and STM) and surface electronic properties (using STS) for surfaces that were polished, etched and passivated in various concentrations of bromine methanol and hydrogen peroxide. We found that for surfaces etched in solutions of bromine that the structural defects arising from polishing are removed, however a number of donor-like and acceptor-like electronic states are introduced, and are thought to be from cadmium vacancies and tellurium dangling bonds, respectively. The amorphous nature of the etched surface broadens these states such that they have tails that penetrate into the band gap region, effectively creating a narrow surface band structure. At room temperature, there is significant charge hopping these states which increases the surface conductivity. For passivated surfaces, based on AFM results, we estimate that a 4 nm thick oxide layer is produced. This layer was found to be quite uniform and additional acceptor-like surface states are introduced at higher energies. The increased uniformity seems to narrow the width of the electronic states resulting in an increased surface band gap. This reduces the rate of charge hopping and therefore lowers the surface conductivity.

Previous studies using scanning tunneling microscopy on CdTe and CdZnTe surfaces and other II-VI semiconductors in general is relatively limited. The results presented in this thesis go a long way to fill this gap and they provide a very strong foundation for future study. Many of the results shown here have strong implications for crystal growth, especially from the vapour phase, since the STM effectively probes the growth interface. This could be even more effectively utilised if, for example, we study films grown by molecular beam epitaxy (MBE). In MBE systems, the growth rate and stoichiometry of

the growth interface can be very precisely controlled and by using STM at times that interrupt the growth process we could gain significant information about the growth mechanisms. As an example, consider a (111) orientated CdTe film epitaxially grown on a substrate by MBE. As shown in Chapter 5, (111) surfaces have been found to form faceted structures. So by performing interrupted experiments during the growth process we could watch how these faceted structures form and develop during growth and find out what effect they have on the crystal quality. Going further, MBE is a very good way of growing semiconductor heterostructures which could be studied in cross-section probing the cleavage plane using STM. A particularly useful tool for this would be tunneling spectroscopy (STS) since it probes the surface as well as the bulk electronic structures allowing, for example, to extract physical quantities such as band offsets or quantised electronic states. The STS results presented in Chapter 4 provide a very strong basis for future study in that case. In Chapter 6 we used STM and STS to investigate the morphology and electronic properties of chemically treated surfaces. In a similar vane, one could study surfaces that have been intentional oxidised in a controlled manner (e.g. in a vacuum system). This would yield results of how CdTe surfaces form oxide layers and what electronic states are introduced for those surfaces. Moving on, this thesis has focused on studying the *low index* surface planes, however there are numerous *high index* surface planes that in theory could be study by STM. As an example consider the (211) surface of a zincblende crystal. This surface orientation is often used as a substrate for epitaxial growth because it yields high growth rates. Indeed, the GaAs(211) surface is known to preferentially form facets.[125] For CdTe however, STM studies on the morphology and structure of the (211) surface are non existent. Finally, many of the studies presented here could be extended to other II-VI semiconductors (e.g. ZnTe, CdSe ,HgTe etc...) using CdTe as a template. STM studies on these materials are even more rare than on CdTe, however significant knowledge gain could be achieved, particularly for crystal growth, by studying them using STM.

This would be particularly relevant since many of these materials are alloyed together to produce useful semiconductor devices (e.g. CdZnTe and HgCdte).

In conclusion, we have used scanning tunneling microscopy to study the morphology, structure and electronic properties of CdTe surfaces. Understanding these properties of surfaces has strong impact upon various physical applications as well as furthering our knowledge of solid materials.

References

[1] H. Luth. *Surfaces and Interfaces of Solid Materials*. Springer, Berlin, third edition, 1995.

[2] S. M. Sze. *Physics of Semiconductor Devices*. Wiley, New York, second edition, 1981.

[3] K. Oura, V. G. Lifshits, A. A. Saranin, A. V. Zotov, and M. Katayama. *Surface Science: An Introduction*. Springer, Berlin, 2003.

[4] D. M. Kolb. *Angew. Chem.*, 40:1163, 2001.

[5] J. R. Arthur. *Surf. Sci.*, 500:189, 2002.

[6] F. Heinrichsdorff, M. H. Mao, N. Kirstaedter, A. Krost, D. Bimberg, A. O. Kosogov, and P. Werner. *Appl. Phys. Lett.*, 71:22, 1997.

[7] H. S. Nalwa. *Handbook of Nanostructured Materials and Nanotechnology*. Academic Press, c2000.

[8] P. K. Larsen and P. J. Dobson. *Reflection High-Energy Electron Diffraction and Reflection Electron Imaging of Surfaces*. Plenum, New York, 1988.

[9] I. K. Robinson and D. J. Tweet. *Rep. Prog. Phys.*, 55:599, 1992.

[10] M. A. Van Hove, W. H. Weinberg, and C.-M. Chan. *Low Energy Electron Diffraction: Experiment, Theory and Surface Structure Determination*. Springer, Berlin, 1986.

[11] A. Benninghoven, F. G. Rudenauer, and H. W. Werner. *Secondary Ion Mass Specrometry: Basic Concepts, Instrumental Aspects, Applications, and Trends*. Wiley, New York, 1987.

[12] J. I. Goldstein. *Scanning Electron Microscopy and X-ray Microanalysis : a text for Biologists, Materials Scientists, and Geologists*. Plenum, New York, second edition, 1992.

[13] R. D. Heidenreich. *Fundamentals of Transmission Electron Microscopy*. Interscience, New York, 1964.

[14] K. Yagi. *Surf. Sci. Rep.*, 17:305, 1993.

[15] E. Bauer. *Rep. Prog. Phys.*, 57:895, 1994.

[16] R. Gomer. *Field Emission and Field Ionization*. American Inst. of Physics, 1992.

[17] R. Wiesendanger. *Scanning Probe Microscopy and Spectroscopy: Methods and Applications*. Cambridge University Press, 1994.

[18] F. J. Giessibl. *Science*, 267:68, 1995.

[19] K. L. Chopra, P. D. Paulson, and V. Dutta. *Prog. Photovoltaics*, 12:69, 2004.

[20] G. F. Knoll. *Radiation Detection and Measurement*. Wiley, third edition, 2000.

[21] T. E. Schlesinger, J. E. Toney, H. Yoon, E. Y. Lee, B. A. Brunett, L. Franks, and R. B. James. *Mat. Sci. Eng. R*, 32:103, 2001.

[22] A. Rogalski. *Rep. Prog. Phys.*, 68:2267, 2005.

[23] M. Carmody, J. G. Pasko, D. Edwall, R. Bailey, J. Arias, S. Cabelli, J. Bajaj, L. A. Almeida, J. H. Dinan, M. Groenert, A. J. Stoltz, Y. Chen, G. Brill, and N. K. Dhar. *J. Electron Mater.*, 34:832, 2005.

[24] D. J. Williams. Mechanical properties of cdte and cdznte. In P. Capper, editor, *Properties of Narraw Gap Cadmium Based Compounds*, Emis datareview series no. 10. 1995.

[25] D. J. Williams. Band structure and carrier properties. In P. Capper, editor, *Properties of Narraw Gap Cadmium Based Compounds*, Emis datareview series no. 10. 1995.

[26] G. Binnig and H. Rohrer. *Rev. Mod. Phys.*, 59:615, 1987.

[27] G. Binnig, H. Rohrer, C. Gerber, and E. Weibel. *Appl. Phys. Lett.*, 40:178, 1982.

[28] G. Binnig, H. Rohrer, C. Gerber, and E. Weibel. *Phys. Rev. Lett.*, 50:120, 1983.

[29] G. Binnig, H. Rohrer, C. Gerber, and E. Weibel. *Phys. Rev. Lett.*, 49:57, 1982.

[30] S. Gasiorowicz. *Quantum Physics*. Wiley, third edition, 2003.

[31] J. Tersoff and D. R. Hamann. *Phys. Rev. B*, 31:805, 1985.

[32] J. Bardeen. *Phys. Rev. Lett.*, 6:57, 1961.

[33] R. M. Feenstra. *J. Vac. Sci. Technol. B*, 5:923, 1987.

[34] R. M. Feenstra, Y. Dong, M. P. Semtsiv, and W. T. Masselink. *Nanotechnology*, 18:044015, 2007.

[35] R. M. Feenstra. *J. Vac. Sci. Technol. B*, 21:2080, 2003.

[36] G. Binnig, C. F. Quate, and C. Gerber. *Phys. Rev. Lett.*, 56:930, 1986.

[37] T. Hashizume, Q. K. Xue, J. Zhou, and A. Ichimiya adn T. Sakurai. *Phys. Rev. Lett.*, 73:2208, 1994.

[38] J. E. Northrup and S. Froyen. *Phys. Rev. B*, 50:2015, 1994.

[39] I. P. Batra, N. Garcia, H. Rohrer, H. Salemink, E. Stoll, and S. Ciraci. *Surf. Sci.*, 181:126, 1987.

[40] Chapter 4. In J. A. Stroscio and W. J. Kaiser, editors, *Scanning Tunneling Microscopy*, Methods of Experimental Physics Vol. 27. 1993.

[41] A. J. Melmed. *J. Vac. Sci. Technol. B*, 9:601, 1991.

[42] I. Ekvall, E. Wahlstrom, D. Claesson, H. Olin, and E. Olsson. *Meas. Sci. Technol.*, 10:11, 1999.

[43] N. Ishida, A. Subagyo, A. Ikeuchi, and K. Sueoka. *Rev. Sci. Instrum.*, 80:093703, 2009.

[44] R. M. Feenstra, G. Meyer, F. Moresco, and K. H. Rieder. *Phys. Rev. B*, 64:081306, 2001.

[45] R. Nishi, I. Houda, T. Aramata, Y. Sugawara, and S. Morita. *Appl. Surf. Sci.*, 157:332, 2000.

[46] J. Wang, A. Howard, R. G. Egdell, J. B. Pethica, and J. S. Foord. *Surf. Sci.*, 515:337, 2002.

[47] Q. Z. Jiang, A. W. Brinkman, P. Veeramani, and P. J. Sellin. *Jpn. J. Appl. Phys.*, 49:025504, 2010.

[48] Q. Z. Jiang, J. T. Mullins, J. Toman, T. P. Hase, B. J Cantwell, G. Lloyd, A. Basu, and A. W. Brinkman. *J. Cryst. Growth*, 310:1652, 2008.

[49] J. T. Mullins, B. J. Cantwell, A. Basu, Q. Z. Jiang, A. Choubey, A. W. Brinkman, and B. K. Tanner. *J. Electron. Mater.*, 37:1460, 2008.

[50] H. K. Sanghera, B. J. Cantwell, and A. W. Brinkman. *J. Cryst. Growth*, 237:1741, 2002.

[51] L. He, C. R. Becker, R. N. Bicknelltassius, S. Scholl, and G. Landwehr. *Semicond. Sci. Technol.*, 8, 1993.

[52] S. M. Johnson, T. J. de Lyon, C. A. Cockrum, W. J. Hamilton, T. Tung, F. I. Gesswin, B. A. Baumgratz, L. M. Ruzicka, O. K. Wu, and J. A. Roth. *J. Electron. Mater.*, 24:467, 1995.

[53] H. Neureiter, S. Spranger, M. Schneider, U. Winkler, M. Sokolowski, and E. Umbach. *Surf. Sci.*, 388:186, 1997.

[54] B. Daudin, D. Brun-Le Cunff, and S. Tatarenko. *Surf. Sci.*, 352:99, 1996.

[55] S. Gundel, A. Fleszar, W. Faschinger, and W. Hanke. *Phys. Rev. B*, 59:15261, 1999.

[56] L. Seehofer, G. Falkenberg, R. L. Johnson, V. H. Etgens, S. Tatarenko, D. Brun, and B. Daudin. *Appl. Phys. Lett.*, 67:1680, 1995.

[57] K. Yong, A. J. Gellman, and P. J. Sides. *Surf. Sci.*, 374:65, 1997.

[58] S. Facsko T. Dekorsy, C. Koerdt, H. Kurz, A. Vogt, and H. L. Hartnagel. *Science*, 285:1551, 1999.

[59] W. L. Chan and E. Chason. *J. Appl. Phys.*, 101:121301, 2007.

[60] R. M. Bradley and J. M. E. Harper. *J. Vac. Sci. Technol. A*, 6:2390, 1988.

[61] U. Valbusa, C. Boragno, and F. Buatier de Mongeot. *J. Phys.: Condens. Matter*, 14:8153, 2002.

[62] G. Ehrlich and F. G. Hudda. *J. Chem. Phys.*, 44:1039, 1966.

[63] R. L. Schwoebel. *J. Appl. Phys.*, 40:614, 1969.

[64] G. Cohen-Taguri, M. Levinshtein, A. Ruzin, and I. Goldfarb. *Surf. Sci.*, 602:712, 2008.

[65] Q. Z. Jiang, B. J. Cantwell, J. T. Mullins, A. Basu, and A. W. Brinkman. *J. Cryst. Growth*, 310:1664, 2008.

[66] M. D. Pashley. *Phys. Rev. B*, 40:10481, 1989.

[67] D. Martrou and N. Magnea. *Thin Solid Films*, 367:48, 2000.

[68] C. B. Duke, A. Paton, W. K. Ford, A. Kahn, and G. Scott. *Phys. Rev. B*, 24:3310, 1981.

[69] R. M. Feenstra and P. Martensson. *Phys. Rev. Lett.*, 61:447, 1988.

[70] R. M. Feenstra. *Phys. Rev. Lett.*, 63:1412, 1989.

[71] R. M. Feenstra. *Phys. Rev. B*, 50:4561, 1994.

[72] M. Pfister, M. B. Johnson, S. F. Alvarado, H. W. M. Salemink, U. Marti, D. Martin, F. Moriergenoud, and F. K. Reinhart. *Appl. Phys. Lett.*, 65:1168, 1994.

[73] R. S. Goldman. *J. Phys. D: Appl. Phys.*, 37:163, 2004.

[74] Y. Dong, R. M. Feenstra, M. P. Semtsiv, and W. T. Masselink. *J. Appl. Phys.*, 103:073704, 2008.

[75] S. Gaan, G. He, R. M. Feenstra, J. Walker, and E. Towe. *Appl. Phys. Lett.*, 97:123110, 2010.

[76] R. M. Feenstra. *Surf. Sci.*, 603:2841, 2009.

[77] D. Hommel, A. Waag, S. Scholl, and G. Landwehr. *Appl. Phys. Lett.*, 61:1546, 1992.

[78] D. Hommel, S. Scholl, T. A. Kuhn, W. Ossau, A. Waag, and G. Landwehrr. *Mater. Sci. Eng. B*, 16:178, 1993.

[79] S. Nozaki and A. G. Milnes. *J. Electron Mater.*, 14:137, 1984.

[80] P. Blood and J. W. Orton. *The electrical characterization of semiconductors : majority carriers and electron states*. Academic Press, London, 1992.

[81] B. Engels, P. Richard, K. Schroeder, S. Blugel, Ph. Ebert, and K. Urban. *Phys. Rev. B*, 58:7799, 1998.

[82] Ph. Ebert, B. Engels, P. Richard, K. Schroeder, S. Blugel, C. Domke, M. Heinrich, and K. Urban. *Phys. Rev. Lett.*, 77:2997, 1996.

[83] N. D. Jäger, Ph. Ebert, K. Urban, R. Krause-Rehberg, and E. R. Weber. *Phys. Rev. B*, 65:195318, 2002.

[84] R. Maboudian, K. Pond, V. Bressler-Hill, M. Wassermeier, P. M. Petroff, G. A. D. Briggs, and W. H. Weinberg. *Surf. Sci. Lett.*, 275:662, 1992.

[85] J. A. Stroscio, R. M. Feenstra, and A. P. Fein. *Phys. Rev. Lett.*, 57:2579, 1986.

[86] J. Mysliveeek, A. Stroecka, J. Steffl, P. Sobotk, I. Ostadal, and B. Voigtlander. *Phys. Rev. B*, 73:161302, 2006.

[87] P. Martensson and R. M. Feenstra. *Phys. Rev. B*, 39:7744, 1989.

[88] M. Prietsch, A. Samsavar, and R. Ludeke. *Phys. Rev. B*, 43:11850, 1991.

[89] R. M. Feenstra, J. Y. Lee, M. H. Kang, G. Meyer, and K. H. Rieder. *Phys. Rev. B*, 73:035310, 2006.

[90] K. O. Magnusson, U. O. Carlsson, D. Straub, S. A. Flodström, and F. J. Himpsel. *Phys. Rev. B*, 36:6566, 1987.

[91] H. Hasegawa and H. Ohno. *J. Vac. Sci. Technol. B*, 4:1130, 1986.

[92] N. Ishida, K. Sueoka, and R. M. Feenstra. *Phys. Rev. B*, 80:075320, 2009.

[93] K. O. Magnusson, S. A. Flodström, and P. E. S. Persson. *Phys. Rev. B*, 38:5384, 1988.

[94] J. G. Simmons. *J. Appl. Phys.*, 34:1793, 1963.

[95] G. Binnig, N. Garcia, H. Rohrer, J. M. Soler, and F. Flores. *Phys. Rev. B*, 30:4816, 1984.

[96] SEMITIP computer program, for 3D band bending and tunnel current computations, available at http://www.andrew.cmu.edu/user/feenstra/.

[97] R. K. Willardson and A. C. Beer. *Semi-insulating GaAs*, volume 20 of *Semiconductors and semimetals*. New York: Academic Press, 1984.

[98] V. Babentsov, J. Franc, P. Hoschl M., Fiederle, K. W. Benz, N. V. Sochinskii, E. Dieguez, and R. B. James. *Cryst. Res. Technol.*, 44:1054, 2009.

[99] M. Fiederle, C. Eiche, M. Salk, R. Schwarz, K. W. Benz, W. Stadler, D. M. Hofmann, and B. K. Meyer. *J. Appl. Phys.*, 84:6689, 1998.

[100] M. Fiederle, A. Fauler, J. Konrath, V. Babentsov, J. Franc, and R. B. James. *IEEE T. Nucl. Sci.*, 51:1864, 2004.

[101] M. Chu, S. Terterian, D. Ting, C. C. Wang, H. K. Gurgenian, and S. Mesropian. *Appl. Phys. Lett.*, 79:2728, 2001.

[102] R. M. Feenstra, S. Gaan, G. Meyer, and K. H. Rieder. *Phys. Rev. B*, 71:125316, 2005.

[103] N. D. Jäger, E. R. Weber, K. Urban, and Ph. Ebert. *Phys. Rev. B*, 67:165327, 2003.

[104] C. K. Egan, A. Choubey, and A. W. Brinkman. *Surf. Sci.*, 604:1825, 2010.

[105] S. Nie, R. M. Feenstra, Y. Ke, R. P. Devaty, and W. J. Choyke. *J. Appl. Phys.*, 103:013709, 2008.

[106] V. Ramachandran and R. M. Feenstra. *Phys. Rev. Lett.*, 82:1000, 1999.

[107] F. Flores and N. Garcia. *Phys. Rev. B*, 30:2289, 1984.

[108] G. F. A. van de Walle, H. van Kempen, P. Wyder, and P. Davidsson. *Appl. Phys. Lett.*, 50:22, 1987.

[109] T. Takahashi, M. Yoshita, and H. Sakaki. *Appl. Phys. Lett.*, 68:502, 1996.

[110] S. Grafstrom. *J. Appl. Phys.*, 91:1717, 2002.

[111] M. Inoue, I. Teramoto, and S. Takayanagi. *J. Appl. Phys.*, 33:2578, 1962.

[112] I. Teramoto and M. Inoue. *Phil. Mag.*, 8:1593, 1963.

[113] T. H. Myers, J. F. Schetzina, T. J. Magee, and R. B. Ormond. *J. Vac. Sci. Technol. A*, 1:1598, 1983.

[114] A. Ebina and T. Takahashi. *J. Cryst. Growth*, 59:51, 1982.

[115] C. Janowitz, R. Manzke, M. Skibowski, and B. A. Orlowski. *Surf. Sci.*, 247:100, 1991.

[116] R. Duszak, S. Tatarenko, J. Cibert, N. Magnea, H. Mariette, and K. Saminadayar. *Surf. Sci.*, 251:511, 1990.

[117] R. Duszak, S. Tatarenko, J. Cibert, K. Saminadayar, and C. Deshayes. *J. Vac. Sci. Technol. A*, 9:3025, 1991.

[118] P. D. Brown, K. Durose, G. J. Russell, and J. Woods. *J. Cryst. Growth*, 101:211, 1990.

[119] S. Y. Tong, G. Xu, and W. N. Mei. *Phys. Rev. Lett.*, 52:1693, 1984.

[120] N. Moll, A. Kley, E. Pehike, and M. Scheffler. *Phys. Rev. B*, 54:8844, 1996.

[121] D. K. Biegelsen, R. D. Bringans, J. E. Northrup, and L. E. Swartz. *Phys. Rev. Lett.*, 65:452, 1990.

[122] A. W. Vere, S. Cole, and D. J. Williams. *J. Electron. Mater.*, 12:551, 1983.

[123] Y. P. Chen, J. P. Faurie, S. Sivananthan, G. C. Hua, and N. Otsuka. *J. Electron. Mater.*, 24:475, 1995.

[124] Y. Xin, N. D. Browning, S. Rujirawat, S. Sivananthan, Y. P. Chen, P. D. Nellist, and S. J. Pennycook. *J. Appl. Phys.*, 84:4292, 1998.

[125] R. Notzel, L. Daweritz, and K. Ploog. *Phys. Rev. B*, 46:4736, 1992.

[126] L. Marchini, A. Zappettini, E. Gombia, R. Mosca, M. Lanata, and M. Pavesi. *IEEE T. Nucl. Sci.*, 56:1823, 2009.

[127] A. Burger, H. Chen, K. Chattopadhyay, D. Shi, S. H. Morgan, W. E. Collins, and R. B. James. *Nucl. Instrum. Meth. A*, 428:8, 1999.

[128] I. M. Kotinay, L. M. Tukhkoneny, G. V. Patsekinay, A. V. Shchukarevz, and G. M. Gusinskii. *Semicond. Sci. Technol.*, 13:890, 1998.

[129] T. B. Wu, J. S. Chen, C. D. Chiang, Y. M. Pang, and S. J. Yang. *J. Appl. Phys.*, 71:5212, 1992.

[130] T. Yang and T. Wu. *Jpn. J. Appl. Phys.*, 34:6184, 1995.

[131] S. Wenbin, W. Kunshu, M. Jiahua, T. Jianyong, Z. Qi, and Q. Yongbiao. *Semicond. Sci. Technol.*, 20:343, 2005.

[132] M. E. Ozsan, P. J. Sellin, P. Veeramani, S. J. Hinder, M. L. T. Monnier, G. Prekas, A. Lohstroh, and M. A. Baker. *Surf. Interface Anal.*, 42:795, 2010.

[133] I. Horcas, R. Fernandez, J. M. Gomez-Rodriguez, J. Colchero, J. Gomez-Herrero, and A. M. Baro. *Rev. Sci. Instrum.*, 78:012705, 2007.

[134] J. Liu, K. C. Mandal, and G. Koley. *Semicond. Sci. Tehcnol.*, 24:045012, 2009.

[135] J. Yang, Y. Zidon, and Y. Shapira. *J. Appl. Phys.*, 91:703, 2002.

[136] G. Zha, W. Jie, T. Tan, and P. Li. *Appl. Surf. Sci.*, 253:3476, 2007.

[137] W. Xiaoqin, J. Wanqi, L. Qiang, and G. Zhi. *Mat. Sci. Semicon. Proc.*, 8:615, 2005.

[138] S. M. Goodnick, D. K. Ferry, C. W. Wilmsen, Z. Liliental, D. Fathy, and O. L. Krivanek. *Phys. Rev. B*, 32:8171, 1985.